



# Non-mesonic weak decay of hypernuclei in effective field theory

Axel Pérez-Obiol Castañeda



Aquesta tesi doctoral està subjecta a la llicència [Reconeixement 3.0. Espanya de Creative Commons](#).

Esta tesis doctoral está sujeta a la licencia [Reconocimiento 3.0. España de Creative Commons](#).

This doctoral thesis is licensed under the [Creative Commons Attribution 3.0. Spain License](#).

Tesi doctoral - PhD Thesis



---

# Non-mesonic weak decay of hypernuclei in effective field theory

---

AXEL PÉREZ-OBIOL CASTAÑEDA

*Directors:*

Dra. Assumpta Parreño García  
Dr. Bruno Juliá Díaz

*Tutora:*

Dra. Assumpta Parreño García

Tesi doctoral presentada a la Universitat de Barcelona, dins del programa de doctorat de Física. Curs 2013/14.

Doctoral thesis presented at the University of Barcelona, within the PhD program of Physics. Academic year 2013/14



# Contents

<b>Resum</b>	<b>v</b>
<b>1 Introduction</b>	<b>1</b>
<b>2 Hypernuclear decay formalism</b>	<b>9</b>
2.1 Light hypernuclei . . . . .	10
2.1.1 Initial hypernuclear wave function . . . . .	10
2.1.2 Total and partial decay rates . . . . .	11
2.1.3 $\Delta I = \frac{1}{2}$ rule . . . . .	12
2.1.4 Initial $\Lambda N$ wave function . . . . .	13
2.1.5 Final $NN$ wave function . . . . .	14
2.1.6 Asymmetry . . . . .	15
2.2 Hypertriton . . . . .	16
2.2.1 Decay rate formula . . . . .	16
2.2.2 Final state wave function . . . . .	19
2.2.3 Final state interaction: the rescattering part . . . . .	21
2.2.4 Basis of three-body states: $ \alpha, p_{12}, p_3\rangle$ . . . . .	22
2.2.5 Matrix elements . . . . .	23
<b>3 Effective field theory description for the <math>\Lambda N \rightarrow NN</math> interaction</b>	<b>25</b>
3.1 Interaction Lagrangians . . . . .	27
3.2 Power counting scheme and non-relativistic expansion . . . . .	30
3.3 Leading order Contributions . . . . .	32
3.3.1 LO order contributions to the $\Sigma N \rightarrow NN$ potential . . . . .	33
3.4 Next-to-leading order contributions . . . . .	34
3.4.1 NLO contact potential . . . . .	34
3.4.2 Two-pion-exchange diagrams . . . . .	37
3.4.3 Master integrals and their relations . . . . .	40
<b>4 Results</b>	<b>43</b>
4.1 Experimental data on the hypernuclear decay observables . . . . .	45
4.2 LO EFT for ${}^5_\Lambda\text{He}$ , ${}^{11}_\Lambda\text{B}$ , and ${}^{12}_\Lambda\text{C}$ . . . . .	46
4.3 Relations between the one-meson exchange potentials and the EFT . . . . .	49
4.3.1 Scalar exchange interaction . . . . .	52
4.4 The Hypertriton decay rate at leading order . . . . .	54
4.5 Comparison of LO and NLO contributions . . . . .	59

---

<b>5 Summary and future perspectives</b>	<b>63</b>
5.1 Future Perspectives . . . . .	66
<b>A Spin matrix elements in position space</b>	<b>69</b>
A.1 Central spin-independent transition ( $\hat{1}$ ) . . . . .	69
A.2 Spin-spin transition ( $\vec{\sigma}_1 \cdot \vec{\sigma}_2$ ) . . . . .	69
A.3 Parity-violating transition ( $\vec{\sigma}_1 \cdot \hat{r}$ ) . . . . .	69
A.4 Tensor transition $3(\vec{\sigma}_1 \cdot \hat{r})(\vec{\sigma}_2 \cdot \hat{r}) - (\vec{\sigma}_1 \cdot \vec{\sigma}_2)$ . . . . .	70
<b>B Spin matrix elements in momentum space</b>	<b>71</b>
B.1 Central spin-independent transition ( $\hat{1}$ ) . . . . .	71
B.2 Central spin dependent transition ( $\vec{\sigma}_1 \cdot \vec{\sigma}_2$ ) . . . . .	71
B.3 Parity violating transition ( $\vec{\sigma}_2 \cdot \vec{q}$ ) . . . . .	72
B.4 Tensor transition operator ( $\vec{\sigma}_1 \cdot \vec{q})(\vec{\sigma}_2 \cdot \vec{q})$ . . . . .	72
<b>C Isospin matrix elements</b>	<b>73</b>
C.1 Unity operator ( $\hat{1}$ ) . . . . .	73
C.2 Operator ( $\vec{\tau}_1 \cdot \vec{\tau}_2$ ) . . . . .	73
C.3 Operator ( $\vec{T}_1 \cdot \vec{\tau}_2$ ) . . . . .	74
C.4 Relation between isospin basis and isopurious basis . . . . .	74
<b>D Diagrams</b>	<b>77</b>
D.1 Caramel diagrams . . . . .	77
D.2 Ball diagrams . . . . .	78
D.3 Triangle diagrams . . . . .	79
D.4 Box diagrams . . . . .	81
<b>E Master integrals</b>	<b>87</b>
E.1 Definitions . . . . .	87
E.2 Results for the master integrals . . . . .	88
E.2.1 $A(m), A(q_0, q'_0)$ and $B(q_0, \vec{q})$ . . . . .	89
E.2.2 $C(q_0, q'_0)$ and $D(q_0, q'_0)$ . . . . .	89
E.2.3 $I(q_0,  \vec{q} , q'_0)$ . . . . .	90
E.2.4 $J(q_0,  \vec{q} , q'_0)$ and $K(q_0,  \vec{q} , q'_0)$ . . . . .	90
E.3 Results for the master integrals with $q_0 = q'_0 = 0$ . . . . .	90
E.4 Relations between master integrals . . . . .	91
E.4.1 $A_\mu(q_0, q'_0)$ . . . . .	91
E.5 $A_{\mu\nu}(q, q')$ . . . . .	91
E.5.1 $B_\mu(q)$ . . . . .	91
E.5.2 $B_{\mu\nu}(q)$ . . . . .	92
E.5.3 $C_\mu(q_0, q'_0)$ . . . . .	92
E.5.4 $C_{\mu\nu}(q_0, q'_0)$ . . . . .	92
E.5.5 $C_{\mu\nu\rho}(q_0, q'_0)$ . . . . .	92
E.5.6 $D_\mu(q_0, q'_0)$ . . . . .	92
E.5.7 $D_{\mu\nu}(q_0, q'_0)$ . . . . .	93
E.5.8 $D_{\mu\nu\rho}(q_0, q'_0)$ . . . . .	93

E.5.9	$I_\mu$	93
E.5.10	$I_{\mu\nu}$	93
E.5.11	$I_{\mu\nu\rho}$	94
E.5.12	$J_\mu$	94
E.5.13	$J_{\mu\nu}$	94
E.5.14	$J_{\mu\nu\rho}$	95
E.5.15	$J_{\mu\nu\rho\sigma}$	95
E.5.16	$K_\mu$	96
E.5.17	$K_{\mu\nu}$	96
E.5.18	$K_{\mu\nu\rho}$	96
E.5.19	$K_{\mu\nu\rho\sigma}$	97
F	Lagrangians for the one-meson-exchange potentials	99
G	One-meson-exchange parameters	101
H	Low energy coefficients in terms of meson-exchange parameters	103
	Bibliography	105



# Resum

En aquesta tesi hem derivat una teoria efectiva de camps per tal de descriure la desintegració feble no mesònica d'hipernuclis. Aquest és un procés extremadament ric. Involucra diversos ingredients que abarquen des d'una precisa comprensió de les interaccions fortes entre els hadrons lleugers, fins a una descripció adequada dels mecanismes febles que desencadenen la desintegració de l'hipernucli. Avui dia els hipernuclis són produïts rutinàriament en diverses instal·lacions arreu del món i les seves desintegracions es poden mesurar amb bona precisió. Això fa que aquests sistemes siguin un bon laboratori on estudiar la física de la interacció feble.

En aquest treball ens hem concentrat en la derivació dels mecanismes de desintegració febles, els quals constitueixen la part menys coneguda en el procés de desintegració hipernuclear. En particular, hem estudiat la transició  $\Lambda N \rightarrow NN$ , principal responsable de la desintegració d'hipernuclis amb un nombre atòmic igual o superior a cinc. Això és degut a què la desintegració mesònica de la partícula  $\Lambda$  (únic canal de desintegració possible per aquest hiperó a l'espai lliure) està fortament suprimida en el medi nuclear. Aquest canal produeix un nucleó i un pió a l'estat final, però aquest nucleó no té prou energia com per, o bé escapar del nucli, o bé accedir a estats lliures per sobre del nivell de Fermi. Aquesta interacció s'ha descrit anteriorment usant models d'intercanvi d'un mesó, integrant-se en el càlcul de l'amplitud de desintegració hipernuclear un cop s'han tractat de forma realista els aspectes d'estructura nuclear lligats a la descripció de l'hipernucli inicial. El resultat és un acord força raonable entre els ritmes de desintegració total i parcial teòrics i les dades experimentals. Aquest èxit en els models fenomenològics d'intercanvi d'un mesó ens ha motivat a fer un pas més enllà i desenvolupar una descripció fonamental del procés  $\Lambda N \rightarrow NN$ , basada en una teoria efectiva de camps (EFT).

La derivació d'aquesta teoria efectiva és el principal resultat (formal) d'aquesta tesi. El seu desenvolupament és essencial per tal de tenir una sòlida comprensió del problema des del punt de vista teòric. Proporciona una descripció del procés de desintegració menys dependent de model i permet millorar les prediccions de la teoria d'una forma sistemàtica. Les teories efectives es construeixen basant-se en una clara separació d'escales físiques en el problema considerat i en l'existència d'un paràmetre prou petit com per poder definir una expansió. En el cas de la interacció forta nucleó-nucleó a energies baixes, on les EFT's s'han desenvolupat durant l'última dècada d'una manera molt exitosa, es pot prendre com a valor d'aquest paràmetre el moment dels nucleons. En el nostre cas, i donat que el moment intercanviat entre els barions és de l'ordre de 400 MeV/c, el paràmetre *petit* el construïm a partir del quotient de dues escales físiques, una associada al valor del moment intercanviat,  $q$ , i l'altra a la massa promig dels barions que participen en el procés.

Havent formulat la teoria fins a ordre  $\mathcal{O}(q^2)$ , ens hem centrat en examinar les dades

experimentals existents. Degut a la poca quantitat de dades experimentals disponibles per a nuclis lleugers hem decidit concentrar-nos en la implementació de l'ordre més baix de la teoria, i d'aquesta manera hem obtingut els valors teòrics per als observables corresponents a tres hipernuclis lleugers,  ${}^5_{\Lambda}\text{He}$ ,  ${}^{11}_{\Lambda}\text{B}$  i  ${}^{12}_{\Lambda}\text{C}$ . La mateixa teoria a ordre més baix s'ha utilitzat per tal de predir el valor de la tasa de desintegració no mesònica per a l'hipernucli més lleuger que podem construir, l'hipertrító. Per tal d'entrar en detall en com tot el procediment s'ha dut a terme, resumim a continuació els resultats principals de la tesi, presentats en els capítols 2, 3 i 4.

## Descripció de la interacció $\Lambda N \rightarrow NN$ amb teoria efectiva de camps

En el capítol 3 descrivim la teoria efectiva de camps desenvolupada per a l'obtenció de l'amplitud de desintegració feble. Primer notem que degut a la diferència en massa entre la  $\Lambda$  i el nucleó, els nucleons emergents s'emporten sempre un moment mínim diferent de zero. Aquest fet ens força a incloure en la nostra teoria efectiva graus de llibertat mesònics (el pió i el kaó) acompañant els termes de contacte. Aquests termes de contacte representen la física d'alta energia (o les curtes distàncies de la interacció) i juguen un paper equivalent a l'intercanvi de mesons pesats en models d'intercanvi mesònic.

Així, descrivim l'amplitud feble a primer ordre per mitjà d'un intercanvi explícit d'un pió i un kaó més interaccions de contacte a ordre zero en l'expansió de moment. Les constants d'acoblament que apareixen en els vèrtexs barió-barió-mesó, o bé es poden obtenir directament dels experiments (com en el cas del pió), o bé s'han de derivar utilitzant simetria SU(3) de sabor. La teoria efectiva a ordre zero és fàcilment derivable tenint en compte totes les possibles estructures de moment, spin i isospín que són compatibles amb les simetries del nostre problema, i té, a aquest ordre, només dues estructures operacionals i per tant dues constants de baixa energia.

La virtut de la descripció efectiva és que, dins del límitat rang de valors que pot prendre el paràmetre usat per definir la teoria, un pot investigar les contribucions dels següents ordres de l'expansió. En aquest capítol hem derivat la teoria efectiva fins a ordre  $\mathcal{O}(q^2)$ . Primer s'han escrit totes les interaccions de contacte fins a aquest ordre, i després, hem calculat tots els diagrames que participen en l'intercanvi de dos pions. Tots els detalls del càlcul d'aquests diagrames, agrupats per la seva topologia segons formen boles, triangles o quadrats, es donen a l'apèndix. Cal dir que aquests diagrames contribueixen a totes les possibles estructures de spin, isospín i moment i per tant el seu efecte s'hauria de tenir en compte en futurs estudis dins del camp. Notem, tanmateix, que la descripció a ordre  $\mathcal{O}(q^2)$  inclou 15 constants de baixa energia (dues de les quals ja estan presents a ordre zero), i que per tant, donat el nombre de dades experimentals (independents) disponibles, fixar la interacció a aquest ordre és quelcom no assumible en el futur immediat.

## Resultats

En el capítol 4, utilitzant el formalisme descrit per al càlcul dels observables de desintegració hipernuclear descrit en el capítol 2, comparem les prediccions de la EFT derivada al capítol 3 amb les dades experimentals existents. Com ja hem esmentat, la base de dades

per a la desintegració hipernuclear no mesònica és notablement curta, havent-hi només uns pocs observables de desintegració d'hipernuclis lleugers mesurats amb bona precisió. Aquesta escassetat de dades ens ha portat a considerar només la contribució a primer ordre en l'amplitud de la desintegració  $\Lambda N \rightarrow NN$ , que com hem dit conté només dos paràmetres independents, els quals són capaços de determinar mitjançant un procés de minimització. Hem dut a terme un ajust als ritmes de desintegració totals, als parcials,  $\Lambda p \rightarrow np$  o  $\Lambda n \rightarrow nn$ , i a l'asimetria dels protons emergents, la qual es pot relacionar amb la interferència entre les parts de violació i conservació de paritat de l'amplitud feble. Això ens ha permès extreure els valors de les dues constants de baixa energia que apareixen al primer ordre de la teoria. Malauradament, les constants de baixa energia trobades no són completament independents del model usat en la descripció de la interacció forta. Per tal d'obtenir un coneixement més complet del problema hem comparat les interaccions de contacte que van acompanyades de les constants de baixa energia amb els potencials corresponents a l'intercanvi d'un mesó pesat. Això s'ha fet de la següent manera, primer expandim els potencials d'intercanvi d'un mesó en potències de  $q$ , i després igualem la teoria efectiva amb el model d'intercanvi d'un mesó, ordre a ordre. D'aquesta manera som capaços d'estudiar la possible contribució d'un mesó escalar-isoescalar en models d'intercanvi mesònic, tal i com s'havia suggerit en treballs previs.

Un cop finalitzat aquest càlcul ens hem centrat en la desintegració feble de l'hipertrító. Aquest és un càlcul consistent, on tots els ingredients, siguin forts o febles, deriven d'una teoria efectiva. En aquest cas, hem presentat el resultat de la desintegració de l'hipertrító cap a estats finals de tres nucleons o d'un deuteró i un neutró.

Finalment, mostrem, com a exemple, una comparació teòrica entre les contribucions dels diagrames d'intercanvi de dos pions, que entren a segon ordre en la teoria, i les corresponents a diagrames d'intercanvi d'un mesó que entren a ordre zero. S'ha trobat que la contribució de l'intercanvi de dos pions és comparable en tamany a les contribucions d'intercanvi d'un pió i d'un kaó, i com a conseqüència s'observen importants interferències tant constructives com destructives entre totes dues contribucions.

Al final de la tesi presentem les possibles extensions i aplicacions del formalisme desenvolupat dins del camp de la física hipernuclear.



# Chapter 1

## Introduction

Being the lightest among the strange baryons, the  $\Lambda$  particle plays an essential role in the study of nuclear physics phenomena involving strangeness. With a mass of  $1115.684 \pm 0.006$  MeV, it is composed by u, d and s valence quarks and it has zero isospin and charge. The decay of the  $\Lambda$  baryon in free space can only proceed via the weak interaction, and therefore, through processes that do not conserve parity, strangeness nor isospin. The decay products are nucleons and pions, which follow the approximate experimental ratio  $\Gamma(\Lambda \rightarrow p\pi^-)/\Gamma(\Lambda \rightarrow n\pi^0)$  close to 2. This value can be theoretically reproduced using isospin coupling algebra and assuming dominance of the  $\Delta I = 1/2$  transitions over the  $\Delta I = 3/2$  ones, assumption that is known as the  $\Delta I = 1/2$  rule for the weak decay of hadrons. The dynamical origin of such rule is not yet understood at a fundamental level, neither its universal validity for the decay involving other hadrons.

The  $\Lambda$  baryon is one of the many strange baryons currently known. Baryons that contain one or more strange valence quarks are called hyperons, and nuclei that contain one or more hyperons are called hypernuclei. The first hypernucleus was discovered in 1952 in Warsaw by Danysz and Pniewski, when they were working with emulsion chamber experiments. At a height of 26 Km above ground, a high energy proton from a cosmic ray hit a nucleus from the emulsion, disintegrating it into small fragments. One of them left a much longer track — it lived much longer than expected by the typical strong interaction time scales —, and ended up disintegrating mesonically. It was the first recorded hypernuclear event [1].

After these early emulsion experiments, much effort was placed in obtaining better statistics on the production and decay of strange systems. The advent of modern particle accelerators represented a very important step forward this goal, giving rise to a more accurate set of data which included a wider range of nuclear masses. A beam of hadrons or electrons, produced in accelerator facilities, collided with a target nucleus, producing a hyperon in the final state which could be captured by a residual nucleus, forming a hypernucleus. Two types of reactions were used for the production mechanism: strangeness exchange reactions, where a non-strange quark and a strange quark were exchanged between the hadrons in the initial and in the final states, e.g.  $n(K^-, \pi^-)\Lambda$ , and associated strangeness production reactions, where a pair of strange and antistrange quarks were created in the final state, e.g. hadronic reactions as  $n(\pi^+, K^+)\Lambda$  or electromagnetic reactions as  $n(e, e'K^+)\Lambda$ . These processes usually leave the system in some excited state.

The hypernuclear ground state can then be reached via either particle (nucleon) emission, strong decay modes and/or the electromagnetic processes, with time scales of the order of  $10^{-16} - 10^{-24}$  seconds. Once the ground state is reached, about  $10^{-10}$  seconds later, the system decays weakly.

The binding energies and the potential depths of the  $\Lambda$  hyperon in light hypernuclei could already be extracted from the analysis of the above mentioned emulsion experiments. Later, in the 70's, different counter experiments at CERN (Switzerland), BNL (USA) and KEK (Japan) could produce, through the  $n(K^-, \pi^-)\Lambda$ ,  $n(K_{stop}^-, \pi^-)\Lambda$  reactions, the first excited hypernuclei. They gave information about hypernuclear structure and the hyperon-nucleon interaction, such as the particularly small  $\Lambda N$  spin-orbit force. However, these experiments still suffered from low statistics and had a limited energy resolution in the spectra. This situation changed in the 80's, when new experiments, first at BNL and later at KEK, studied hypernuclei through the  $n(\pi^+, K^+)\Lambda$  reaction. The higher beam intensities that were available allowed one to obtain a spectra of much higher quality, facilitating the detection of the final particles in the decay mechanism and consequently, opening the door for a more precise determination of the different decay observables. In the 90's, new experimental techniques were developed based in gamma-ray spectroscopy, and using the  $n(e, e'K^+)\Lambda$  reaction it was possible to obtain further information on the hypernuclear energy levels and their weak decay. All this experimental work has led to characterize quite a variety of hypernuclei (from  $^3_\Lambda H$  to  $^{208}_\Lambda Pb$ ), extending thus the nuclear landscape (see Fig.1.1) and providing a better understanding of the hypernuclear structure and of the interactions among hyperons and nucleons. Most of the international facilities responsible for this work (BNL, TJNAF, KEK) are still active and producing new data on hypernuclear spectroscopy and/or hypernuclear decay. The inclusion of an important strange physics program in the newly constructed experimental facilities (FINUDA at DAPHNE [3] or the future experiments at JPARC [4] and FAIR [5]) is a clear proof of the intense experimental activity in the field.

The data collected by hypernuclear experiments has been used to study the elementary weak  $\Lambda N \rightarrow NN$  interaction. However, the presence of the nuclear medium does not allow us to extract clean amplitudes for the two-body transition, and experiments less affected by the medium would be much more desirable. An attempt in this direction was taken some years ago by proposing to measure the weak production reaction  $np \rightarrow \Lambda p$  at RCNP (Osaka, Japan). A big effort was invested in extracting different polarization observables for this process. However, the experiment suffered from very low statistics due to the very small values of the cross sections for the production mechanism, of the order of  $10^{-12}$  mb [6, 7, 8], and these observables could not be extracted [9, 10]. Until the experimental community overcomes this difficulty and/or physicists come up with new alternative measurements, the decay of hypernuclei will be the only quantitative way to obtain information on the weak  $|\Delta S| = 1$  four-fermion interaction.

Along with these experiments, many theoretical groups have invested a lot of effort to understand the underlying theory governing the decay process, deriving models that were intended to reproduce the various hypernuclear decay data. In hypernuclei, the  $\Lambda$  is not free anymore but bound inside a medium of nucleons. When the  $\Lambda$  decays mesonically, the final nucleon has a momentum of  $\sim 100$  MeV, which is not large enough to access to unoccupied energy levels in the nucleus, except for very light systems (with  $A \leq 5$ ).

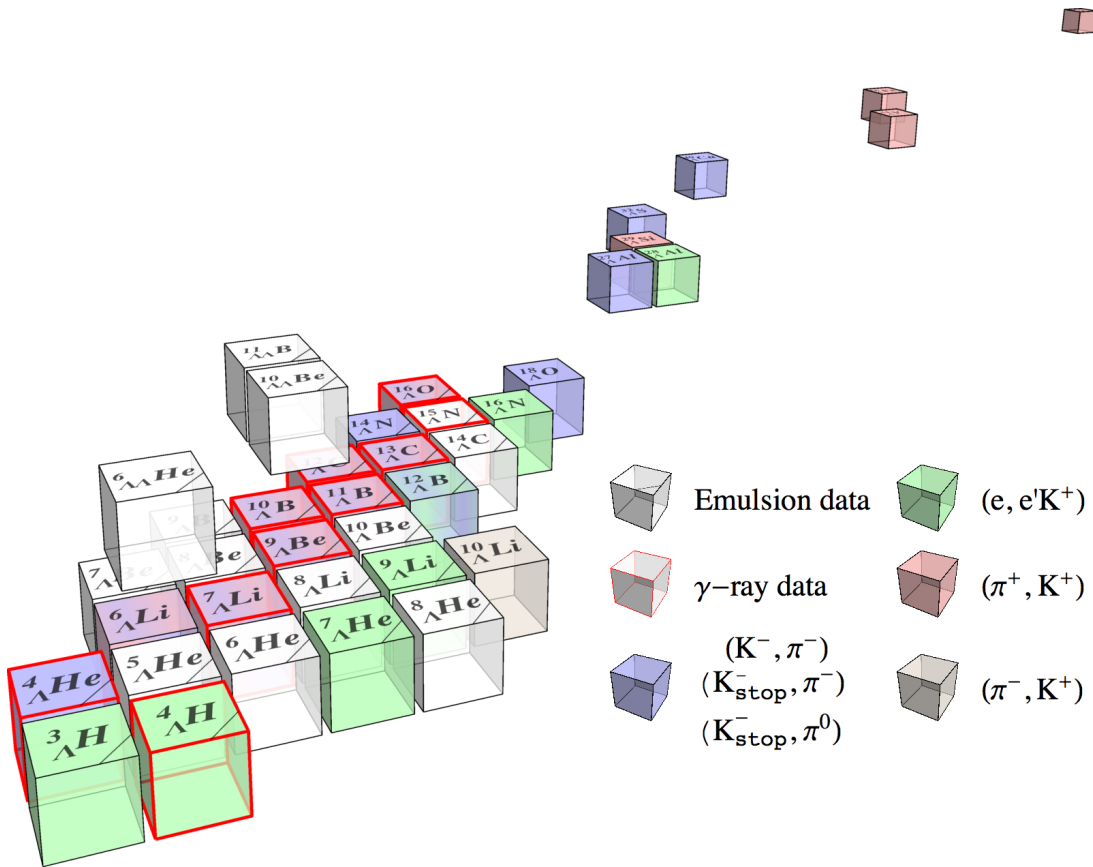


Figure 1.1: Layers  $s = -1$  and  $s = -2$  of the nuclear landscape. In the coming years, new experiments will contribute with more hypernuclei in both layers. Original data for the  $\Lambda$ -hypernuclei is taken from [2].

The same medium which is responsible for the Pauli-blocking on the final nucleon, is also responsible for the appearance of new decay mechanisms, the single and multi-nucleon induced channels,  $\Lambda N \rightarrow NN$  and  $\Lambda NN \rightarrow NNN$ , where no mesons are detected in the final state. Fig. 1.2, taken from Ref. [11], shows how the mesonic decay rate decreases with the mass number  $A$ , while the nucleon-induced decay increases, reaching a saturation value of the order of the decay rate of the  $\Lambda$  in free space, reflecting the short range nature of the  $\Lambda N \rightarrow NN$  interaction. The first counter experiments were able to extract values for the total non-mesonic decay rate ( $\Gamma_{nm}$ ) and the partial decay rate induced by protons,  $\Gamma_p$  ( $\Lambda p \rightarrow pn$ ), while extracting the neutron-induced rate,  $\Gamma_n$  ( $\Lambda n \rightarrow nn$ ), from direct subtraction of the former quantities. The newest experimental setups are able to detect in coincidence two nucleons in the final state, either a  $nn$  pair or a  $np$  pair, and from this measure give a realistic estimation of the so called neutron-to-proton ratio,  $\Gamma_n/\Gamma_p$ . Therefore, experimentalists usually give two independent quantities to constrain the different theoretical models,  $\Gamma_{nm}$  and  $\Gamma_n/\Gamma_p$ . Moreover, polarized hypernuclei were produced at KEK by using the  $(\pi^+, K^+)$  reaction under some particular kinematic conditions. This polarization produces an asymmetry ( $\mathcal{A}$ ) between the intensity of protons emitted parallel and antiparallel to the hypernuclear polarization axis, which, in turn, can be related to

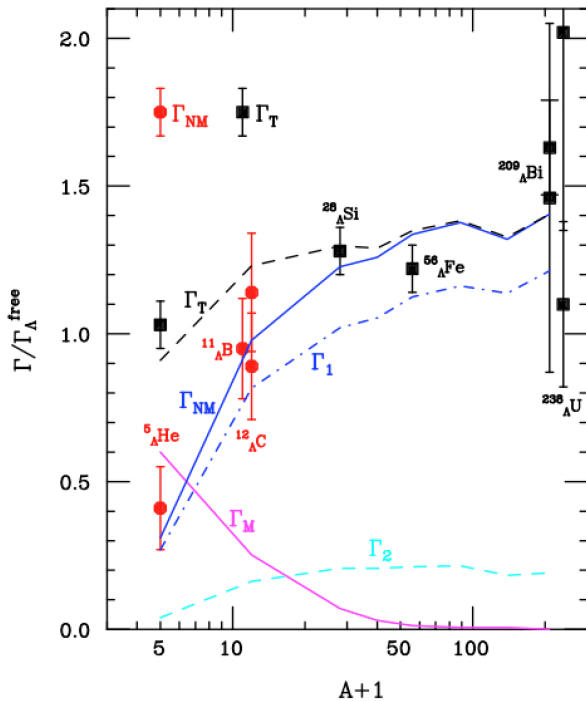


Figure 1.2: Weak decay rates as a function of the mass number  $A$ . The lines are theoretical calculations that use a polarization propagator method and a local density approximation [11]. The upper dashed and black line represents the total decay rate; the dark blue solid one represents the non-mesonic decay rate, which is the sum of the one-nucleon induced (dashed and dark blue line) and two-nucleon induced (dashed and light blue line) decays; the solid pink lower line represents the mesonic decay rate. The experimental points are labeled with black squares (for the total decay rates) and with round red circles (for the non-mesonic decay rates). Figure taken from Ref. [11].

the interference between the parity violating (PV) and parity conserving (PC) amplitudes corresponding to the  $\Lambda N \rightarrow NN$  transition. Therefore, at most, one can have three independent quantities characterizing the non-mesonic decay of a given hypernucleus:  $\Gamma_{nm}$ ,  $\Gamma_n/\Gamma_p$  and  $\mathcal{A}$ . For instance, the  ${}^5_\Lambda\text{He}$  observables or the total and partial decay rates for the p-shell  ${}^{12}_\Lambda\text{C}$  and  ${}^{11}_\Lambda\text{B}$  hypernuclei measured by KEK-PS E462 and KEK-PS E307 experiments [12, 13]. The decay of lighter nuclei is also desirable due to a cleaner extraction of the elementary weak four-fermion interaction, less contaminated by the presence of the medium. As an example, the E22 experiment at J-PARC [14], which will study the decay of the s-shell  ${}^4_\Lambda\text{H}$  and  ${}^4_\Lambda\text{He}$  systems.

The non-mesonic decay observables have been studied theoretically using different approaches. Guided by the previous work done in the description of the strong nucleon-nucleon (NN) interaction, hypernuclear physicists have tackled the weak  $\Lambda N \rightarrow NN$  transition in analogous ways. As a first step, the interaction was interpreted as the emission of a pion by the  $\Lambda$  hyperon that was absorbed by one of the nucleons in the medium. The result was that the non-mesonic decay rate could be fairly reproduced by this pion-exchange (OPE) mechanism, while the values obtained for the neutron-to-proton ratio

---

were too low compared with the central experimental numbers [15]. The reason resides in the dominance of the OPE tensor term which, for transitions induced by s-shell nucleons, translates in very low values for the production of a  $nn$  pair, and consequently, for  $\Gamma_n/\Gamma_p$ . A number of improvements were proposed: (a) the inclusion in the exchange mechanism of heavier mesons and uncorrelated two-pion exchanges, which would account for shorter ranges in the interaction[16, 17, 18, 19, 20], and produce interferences in the different spin-isospin transition channels that could increase the neutron-to-proton ratio, while keeping the total non-mesonic decay rate in agreement with the experimental data; (b) the inclusion of explicit  $\Delta I = 1/2$  breaking terms [21, 22]; (c) the consideration of the two-nucleon induced channel,  $\Lambda NN \rightarrow NNN$  [23, 24, 25, 26]; and (d) the combination of the long-ranged OPE mechanism with quark models suited for the description of shorter distances [27, 28]. Although these improvements succeeded in predicting a larger value for the theoretical neutron-to-proton ratio with a moderate increase in the total non-mesonic decay rate, a clear better agreement with experimental data was not achieved until an accurate description of the medium effects was included [29]. For instance, the partial decay rates, extracted with good precision from two-nucleon coincidence experiments performed at KEK [12, 30, 31, 32], could not be reproduced until the final state interactions between the outgoing nucleons and the residual nuclear medium were accounted for [33, 34, 35].

One of the remarkable good points regarding the theoretical models used is that, with a simple set of parameters, they successfully reproduce hypernuclear decay rates. However, these approaches have a very narrow scope and one can argue if they are really connected to the underlying physics —the results are model dependent—. For instance, in the one-boson exchange (OBE) model, the non-pionic couplings and form-factors are unknown and must be derived using  $SU_F(3)$  and  $SU(6) = SU_F(3) \otimes SU_{spin}(2)$  symmetries, which we know are broken at the 30% level (at least). Moreover, the vector mesons ( $\rho, \omega, K^*$ ) are too heavy to probe the short ranges ( $r \sim 0.25$  fm) they account for. At these small distances, the wave functions from the interacting baryons and mesons overlap, and one may wonder if the quark degrees of freedom would already play an important role in the interaction. A more general approach, more deeply connected to the underlying theory, is required to gain more fundamental insight.

Since the development of quantum chromodynamics (QCD), physicists have tried to understand nuclear physics from a broad perspective. The main drawback with this approach is the non-perturbative nature of QCD, which prevents the use of perturbative methods to solve the nuclear force in terms of the basic ingredients of QCD, quarks and gluons. Two theoretical efforts, very interconnected, are trying to overcome this problem, lattice QCD (LQCD) and effective field theories (EFTs), both giving very encouraging results (e.g. [36, 37]).

On the one hand, LQCD uses the path-integral formalism to perform finite-volume calculations in a discretized space-time, by using a lattice of size  $L$  and distance between nodes (lattice spacing)  $a$ . Within this approach, quarks are placed in the nodes of the lattice while gluons, the carriers of the strong force, act as links connecting those nodes. This discretization provides a natural cut-off for the theory of the order of  $1/a$ . Moreover, the space-time is Wick-rotated so an Euclidean time is obtained. Then the theory, regularized by this cut-off and defined in the Euclidean space, can be solved by using numerical Monte-Carlo methods. The cost of performing numerical calculations of QCD increases

with decreasing quark mass ( $m_q$ ) values. As a result, most of the present day computations involving baryons can only be done with unphysical large values for the light quark masses. After performing a few calculations using unrealistic  $m_q$  values, extrapolations (based on effective theories) to the physical *up* and *down* masses are required to connect the numerical results to nature. The computational cost also increases with increasing volumes and decreasing lattice spacings, and therefore, additional infinite volume and continuum extrapolations have to be undertaken to give realistic predictions for physical observables. Although computationally expensive, LQCD has the great advantage to provide direct information on the baryon-baryon interaction without contamination of the medium [38, 39, 40, 41]. A few attempts have been made to use this technique also in the weak sector involving baryons. The calculation is technically much more involved than the strong counterpart, and only very preliminary results have been published concerning the  $NN$  parity-violating amplitude [42].

On the other hand, effective field theories designed to describe hadronic processes do not use the fundamental Lagrangian formulated in terms of quarks and gluons, but one built with only degrees of freedom which are relevant at the low-energy (nuclear) scale. The short range Lagrangian is built in the most general, systematic way, such that all the physics below a certain scale is encapsulated in a minimum set of parameters. This Lagrangian is still connected to the underlying theory by respecting all of its symmetries and symmetry breakings, for instance, the spontaneously broken chiral symmetry of QCD. S. Weinberg made the first step in showing how to apply effective field theories to the nuclear force [43, 44], and a few years later, C. Ordoñez, L. Ray, and U. van Kolck [45] performed the first quantitative calculation for the  $NN$  interaction. Since then, different groups have studied the nuclear force with increasing accuracy (up to next-to-next-to-next-to-leading order, 3NLO, in perturbation theory), [36, 46, 47, 48]. Effective field theories have also been applied for the description of processes involving strangeness, in both, the weak and strong sectors. In Ref. [49] the authors studied the nucleon-nucleon parity violation with a leading order (LO) effective field theory, while  $SU_F(3)$  extensions of the previously developed EFT for the nuclear force were carried out at leading order in Refs. [50, 51, 52, 53, 54] and, more recently, at next-to-leading order (NLO) in Ref. [55].

Our work uses effective field theory techniques to describe the weak,  $|\Delta S| = 1$ ,  $\Lambda N$  transition. The EFT for the  $\Lambda N \rightarrow NN$  interaction was first formulated in Refs. [56] and [57, 58]. While the authors in [56] constructed the effective theory by adding to the long-ranged one-pion-exchange mechanism (OPE) a four-fermion-point interaction, coming from Lorentz four-vector currents, Refs. [57, 58] considered the additional  $K$ -exchange mechanism (OKE) to account for the intermediate range of the interaction, as well as additional operational structures in the form of contact terms, to describe the short-range physics. These structures result when all possible operators compatible with the symmetries fulfilled by the weak  $|\Delta S| = 1$   $\Lambda N$  interaction are considered. The local operators governing short distance dynamics in any EFT appear in the Lagrangian multiplied by low-energy constants (LECs), which have to be determined by a fit to the available experimental data. Although neither the amount nor the quality of hypernuclear weak decay data is comparable with the wealth of information available in the nonstrange sector, these data are enough to fairly constrain the lowest-order LECs. In this thesis we extend and update previous work in this direction, by developing an effective field

---

theory for the  $\Lambda N \rightarrow NN$  interaction which includes explicitly all the possible two-pion exchange contributions. Moreover, the EFT at LO is used to describe the decay of four different hypernuclei and thus, constrain the fundamental weak interaction with the extraction of the LO low energy constants. For three of these hypernuclei,  $^5_{\Lambda}\text{He}$ ,  $^{11}_{\Lambda}\text{B}$  and  $^{12}_{\Lambda}\text{C}$ , we use a shell model approach for the initial hypernuclear wave function. Harmonic oscillator wave functions are used for the  $\Lambda$  and the nucleon in the hypernucleus, and a phenomenological spin-independent correlation function is used to account for the effective strong interaction among the two interacting baryons. For the final state, only the strong interaction between the weakly emerging nucleons is taken into account, through a Lippmann-Schwinger calculation which uses microscopical OBE potentials for the strong NN interaction. Then, the two low-energy constants appearing at LO are fitted to the different hypernuclear decay observables corrected from final state interactions with the residual medium.

An additional calculation is performed for the hypertriton,  $^3_{\Lambda}\text{H}$ , which is the lightest hypernucleus one can think of, and therefore, the best strange system to treat the nuclear medium in a systematic and realistic way. The fact that it only contains three baryons—a proton, a neutron and a  $\Lambda$ —makes it possible to take into account all the possible two-body interactions explicitly and in a exact way. The wave functions for the initial and final state (be it three nucleons or a deuteron plus a neutron) are then calculated using strong chiral EFT forces up to next-to-next-to-leading order (NNLO), reducing the model dependencies that unavoidably appear in calculations involving heavier systems. With a running of the two LO LECs we illustrate how the total and partial decay rates depend on the short range physics. From our study it comes clear that the feasibility of a higher-order description of the weak four-fermion interaction, and therefore, the achievement of a deeper understanding of the fundamental dynamics involved, requires more independent and accurate experimental data, specially involving light strange systems.

In order to get some insight of the dynamical origin of the LECs appearing in the effective theory and at the same time detect possible deficiencies in boson-exchange descriptions of the weak mechanism, we also show the results of a mapping of the EFT to successful one-meson-exchange (OME) models. Following this procedure, we have written the low-energy constants in terms of physical ingredients of the OME models, as masses, strong form factor parameters and couplings of pseudoscalar and vector mesons to baryons, following an approach known as resonance saturation.

This thesis is organized in three main parts: the formalism, the results, and the conclusions. The formalism used to evaluate the hypernuclear decay is described in chapters 2 and 3. In chapter 2 we write the total and partial decay rates, and the asymmetry, in terms of the four-body weak  $\Lambda N \rightarrow NN$  transition. We explicitly show how the strong interactions are accounted for in the initial and final states, and also how the weakly interacting baryons are uncoupled from the rest of nucleons in the initial hypernucleus. In chapter 3 the EFT potential for the weak  $\Delta S = 1$  interaction is derived. In particular, we indicate the different Lagrangians and the power counting used, and display all the possible contributions in terms of Feynman diagrams. The technical details that appear in the formalism (integrals, relations between integrals, and explicit results for the two pion exchanges) are given explicitly in the appendices. The results are shown in chapter 4, and include the values obtained for the different hypernuclear observables, and how these

are best fitted with a particular set of low energy constants. The comparison between the LO EFT with the OME model is also included in this chapter. We conclude in the last chapter, by summarizing the work done and by pointing out possible future perspectives.

# Chapter 2

## Hypernuclear decay formalism

The description of the non-mesonic weak decay of hypernuclei requires the knowledge of the initial and final wave functions and of the two-body mechanism. The wave functions are determined by the strong interactions among the baryons, while the two body transition involves also the weak force. In this chapter we formulate the formalism for the decay of hypernuclei, leaving the derivation of the weak two-body transition potential for chapter 3. More precisely, we describe the hypernuclear decay observables in terms of the  $\Lambda N \rightarrow NN$  amplitude.

To obtain the wave functions for nuclear bound states one needs, in principle, to solve the non-relativistic Schrödinger equation for a many-body system. For light nuclei, ( $A < 5$ ), this has been possible due to the development of few-body techniques, such as the Faddeev-Yakubovsky scheme [59]. For larger nuclei, it becomes too difficult to numerically solve the Schrödinger equation, and one needs to use many-body methods such as the shell model, the coupled-cluster approach, or Monte-Carlo simulation techniques [60].

We use two different approaches in the description of the strong interactions, depending on how massive is the hypernucleus under consideration. For  $A \geq 5$ , it is not feasible to explicitly take into account the two and three-body strong interactions among the baryons in the hypernuclear system on one hand and among the baryons in the final state on the other hand. In our approach, we have used a shell-model to describe the initial hypernucleus. The hyperon and nucleon wave functions have been obtained from a mean field harmonic oscillator potential, adjusting the oscillator parameters to reproduce the experimental binding energy for the  $A$ -hypernucleus and the  $(A - 1)$  core respectively. Regarding the final wave function, we have not included the propagation of the two primary outgoing nucleons within the residual medium. In our approximation, the residual  $(A - 2)$  nucleus acts as a spectator, and only the strong interaction among these two primary nucleons is considered. More specifically, we solve a Lippman-Schwinger scattering equation with the input of modern potential models. This approximation can lead to unrealistic results for exclusive observables — partial decay rates ( $\Gamma(\Lambda n \rightarrow nn)$  and  $\Gamma(\Lambda p \rightarrow np)$ ) and the asymmetry in the distribution of protons coming from the decay of polarized hypernuclei —. In any case, we will always compare our results to observables corrected by these final-state interaction effects.

For lighter hypernuclei ( $A = 3, 4$ ), the initial and final wave functions can be computed using two and three-body forces that act among all the baryons. Faddeev-Yakubovsky

calculations for  $A = 3, 4$  hypernuclear systems have been carried out in [61, 62]. This allows us to describe the decay of light hypernuclei with effective field theory (EFT) potentials in both the nuclear part and the two-body weak transition, which leads to a less model-dependent and more systematic framework.

In this work we describe the decay rate observables for  ${}^5_\Lambda He$ ,  ${}^{11}_\Lambda B$ ,  ${}^{12}_\Lambda C$  and  ${}^3_\Lambda H$ . The decay for the first three hypernuclei is described through the shell-model approach (in Sec. 2.1), while for the hypertriton the EFT formalism is used (in Sec. 2.2).

## 2.1 Light hypernuclei

Our goal in this section is to express the hypernuclear observables for the non-mesonic decay of light hypernuclei in terms of the two-body amplitude and the initial and final wave functions.

The decay rate for a hypernucleus decaying non-mesonically into a residual nuclear part ( $R$ ) and two free nucleons (1 and 2) is written as

$$\Gamma_{nm} = \int \frac{d^3 k_1}{(2\pi)^3} \int \frac{d^3 k_2}{(2\pi)^3} \sum_{\substack{M_I \{R\} \\ \{1\}\{2\}}} (2\pi)\delta(M_H - E_R - E_1 - E_2) \frac{1}{2J+1} |\mathcal{M}_{fi}|^2. \quad (2.1)$$

All the possible angular momentum and momentum final states ( $\{R\}$ ,  $\{1\}$ ,  $\{2\}$ ) have been summed and integrated, while the initial spins,  $M_I$ , have been averaged. The delta function ensures energy conservation:  $M_H$  is the mass of the hypernucleus, and  $E_R$ ,  $E_1$  and  $E_2$  are the energies of the residual nuclear part and the two outgoing nucleons, respectively. Using relative and center of mass momenta coordinates ( $P$  and  $k$ ), the matrix element  $\mathcal{M}_{fi}$  connecting the initial and final states in the decay rate formula is

$$\mathcal{M}_{fi} = \langle F | \mathcal{M} | I \rangle = \left\langle \Psi_R; \vec{P} \vec{k} S M_S T M_T \right| \hat{O}_{\Lambda N \rightarrow NN} | {}_\Lambda A \rangle ,$$

where  $\Psi_R$  is the wave function for the residual part, and  $\vec{P}$ ,  $\vec{k}$ ,  $S$ ,  $M_S$ ,  $T$ ,  $M_T$  are the momenta, spin and isospin of the final two nucleons. We denote the initial state for a  $\Lambda$ -hypernucleus of mass number  $A$  as  $| {}_\Lambda A \rangle$ , and the operator mediating the two-body transition,  $\hat{O}_{\Lambda N \rightarrow NN}$ .

### 2.1.1 Initial hypernuclear wave function

In order to write the decay rate in terms of the 4-body interaction we need to uncouple the  $\Lambda$  and the interacting nucleon from the initial hypernuclear wave function. We assume that the  $\Lambda$  couples to the ground state ( $A-1$ ) nuclear core,

$$\begin{aligned} | {}_\Lambda A \rangle_{T_I T_{3I}}^{J_I M_I} &= | \Lambda \rangle \otimes | A-1 \rangle \\ &= \sum_{m_\Lambda M_C} (j_\Lambda J_C J_I, m_\Lambda M_C M_I) | (n_\Lambda l_\Lambda s_\Lambda) j_\Lambda m_\Lambda \rangle | J_C M_C T_I T_{3I} \rangle , \end{aligned}$$

where we define the initial hypernuclear spin and isospin and their projections as  $J_I$ ,  $M_I$ ,  $T_I$  and  $T_{3I}$ . The quantum numbers (shell, spin and isospin) of the  $\Lambda$  are  $n_\Lambda = 0$ ,  $l_\Lambda = 0$ ,

$s_\Lambda = 1/2$ , which couple to  $j_\Lambda = 1/2$ ,  $m_\Lambda = 1/2$ .  $J_C$ ,  $M_C$ ,  $T_I$  and  $T_{3_I}$  stand for the spin and isospin for the core wave function. To uncouple the nucleon of the core wave function (while maintaining its antisymmetry character) we use the technique of the coefficients of fractional parentage (we use the numerical values given in Ref. [63] for p-shell nucleons and in Ref. [64] for s-shell nucleons),

$$\begin{aligned} |J_C M_C T_I T_{3_I}\rangle &= \sum_{J_R T_R j_N} \langle J_C T_I \{ | J_R T_R, j_N t_N \rangle [ |J_R, T_R\rangle \times |(n_N l_N s_N) j_N, t_N\rangle ]^{J_C M_C}_{T_I T_{3_I}} \\ &= \sum_{J_R T_R j_N} \langle J_C T_I \{ | J_R T_R, j_N t_N \rangle \\ &\quad \times \sum_{M_R m_N} \sum_{T_{3_R} t_{3_i}} (J_R j_N J_C, M_R m_N M_C) (T_R t_N T_I, T_{3_R} t_{3_i} T_{3_I}) \\ &\quad \times |J_R M_R\rangle |T_R T_{3_R}\rangle |(n_N l_N s_N) j_N m_N\rangle |t_N t_{3_i}\rangle, \end{aligned} \quad (2.2)$$

where  $n_N$ ,  $l_N$ ,  $s_N$ ,  $j_N$ , and  $t_N$  ( $= 1/2$ ) denote, respectively, the shell, angular momentum, spin, total spin, and isospin of the uncoupled nucleon; and  $J_R$ ,  $M_R$ , and  $T_R$ ,  $T_{3_R}$  the spin and isospin for the residual system.  $\langle J_C T_I \{ | J_R T_R, j_N t_N \rangle$  are the coefficients of fractional parentage, which allow us to write the core wave function as a residual part coupled to a nucleon.

### 2.1.2 Total and partial decay rates

Considering that the  $\Lambda$  is in a  $l_\Lambda = 0$  state, and writing the coefficients of fractional parentage as spectroscopic factors,  $S(J_C T_C \alpha; J_{R_0} T_{R_0} \alpha_0, j_N) \equiv N \langle J_C T_I \{ | J_R T_R, j_N t_N \rangle^2$  ( $N$  being the total number of active nucleons), the non-mesonic decay rate can be written as,

$$\Gamma_{nm} = \Gamma_n + \Gamma_p, \quad (2.3)$$

where the partial decay rates are written in the general form

$$\begin{aligned} \Gamma_i &= \int \frac{d^3 P}{(2\pi)^3} \int \frac{d^3 k}{(2\pi)^3} (2\pi) \delta(M_H - E_r - E_1 - E_2) \sum_{S M_S} \sum_{J_R M_R} \sum_{T_R T_{3_R}} \frac{1}{2J_I + 1} \\ &\quad \times \sum_{M_I} \left| (T_R \frac{1}{2} T_I, T_{3_R} t_{3_i} T_{3_I}) \right|^2 \\ &\quad \times \left| \sum_{T T_3} \left( \frac{1}{2} \frac{1}{2} T, t_1 t_2 T_3 \right) \sum_{m_\Lambda M_C} (j_\Lambda J_C J_I, m_\Lambda M_C M_I) \sum_{j_N} \sqrt{S(J_C T_I; J_R T_R, j_N t_{3_i})} \right. \\ &\quad \times \sum_{M_R m_N} (J_R j_N J_C, M_R m_N M_C) \sum_{m_{l_N} m_{s_N}} (l_N \frac{1}{2} j_N, m_{l_N} m_{s_N} m_N) \\ &\quad \times \sum_{m_{l_\Lambda} m_{s_\Lambda}} (l_\Lambda \frac{1}{2} j_\Lambda, m_{l_\Lambda} m_{s_\Lambda} m_\Lambda) \sum_{S_0 M_{S_0}} \left( \frac{1}{2} \frac{1}{2} S_0, m_{s_\Lambda} m_{s_N} M_{S_0} \right) \sum_{T_0 T_{3_0}} (\frac{1}{2} \frac{1}{2} T_0, -\frac{1}{2} t_{3_i} T_{3_0}) \\ &\quad \times t_{\Lambda N \rightarrow NN}(S, M_S, T, T_3, S_0, M_{S_0}, T_0, T_{3_0}, l_\Lambda, l_N, \vec{P}, \vec{k}) \Big|^2, \end{aligned} \quad (2.4)$$

	$J_R$	$T_R$	$S$	$S^n$	$S^p$
s-shell	1	0	0.375	0.319	0.300
	1	1	1.125	0.956	0.900
	2	0	0.625	0.531	0.500
	2	1	1.875	1.594	1.500
$p_{3/2}$ -shell	0	0	0.000	0.000	0.000
	0	1	0.653	0.718	0.718
	1	0	0.606	0.667	0.667
	1	1	0.129	0.142	0.142
	2	0	0.097	0.107	0.107
	2	1	3.038	3.341	3.341
	3	0	1.239	1.363	1.363
	3	1	0.125	0.137	0.137
$p_{1/2}$ -shell	1	0	0.312	0.343	0.343
	1	1	0.104	0.115	0.115
	2	0	0.246	0.271	0.271
	2	1	0.451	0.496	0.496

Table 2.1: Spectroscopic factors for s-shell and p-shell for  $^{12}\Lambda C$ . The neutron and proton spectroscopic factors are denoted, respectively as  $S^n$  and  $S^p$ .

with  $t_{3_i} = 1/2$ ,  $t_1 = -1/2$ ,  $t_2 = 1/2$  for the p-induced direct diagram and  $t_{3_i} = -1/2$ ,  $t_1 = -1/2$ ,  $t_2 = -1/2$  for the n-induced one. We denote the spin and isospin for the initial pair  $\Lambda N$  as  $S_0$ ,  $M_{S_0}$  and  $T_0$ ,  $T_{3_0}$ . As an example, the spectroscopic factors  $S(J_C T_C \alpha; J_{R_0} T_{R_0} \alpha_0, j_N)$  for the  $^{12}\Lambda C$  are listed in Table 2.1.2.

### 2.1.3 $\Delta I = \frac{1}{2}$ rule

In Eq. (2.4) the  $\Lambda$  is assumed to be in a  $|1/2, -1/2\rangle$  state due to the isospin  $1/2$  rule. This rule reflects the dominance of the  $\Delta I = 1/2$  weak transitions over the  $\Delta I = 3/2$  ones, and is derived from the experimental value

$$\frac{\Gamma_{\Lambda \rightarrow \pi^- p}^{free}}{\Gamma_{\Lambda \rightarrow \pi^0 n}^{free}} = 1.78. \quad (2.5)$$

Assuming that the  $\Lambda$  is coupled to an isospurion of  $\Delta I = 1/2$  we have:

$$\frac{\Gamma_{\Lambda \rightarrow \pi^- p}^{free}}{\Gamma_{\Lambda \rightarrow \pi^0 n}^{free}} \sim \frac{|\langle \pi^- p | T_{1/2, -1/2} | \Lambda \rangle|^2}{|\langle \pi^0 n | T_{1/2, -1/2} | \Lambda \rangle|^2} = \frac{|\sqrt{2/3}|^2}{|\sqrt{1/3}|^2} = 2, \quad (2.6)$$

while coupling the  $\Lambda$  to an isospurion of  $\Delta I = 3/2$  gives

$$\frac{\Gamma_{\Lambda \rightarrow \pi^- p}^{free}}{\Gamma_{\Lambda \rightarrow \pi^0 n}^{free}} \sim \frac{|\langle \pi^- p | T_{3/2, -1/2} |\Lambda \rangle|^2}{|\langle \pi^0 n | T_{3/2, -1/2} |\Lambda \rangle|^2} = \frac{|\sqrt{1/3}|^2}{|\sqrt{2/3}|^2} = \frac{1}{2}. \quad (2.7)$$

### 2.1.4 Initial $\Lambda N$ wave function

Eqs.(2.3) and (2.4) show how to calculate the total and partial non-mesonic decay rates in terms of the two-body transition  $t_{\Lambda N \rightarrow NN}(S, M_S, T, T_3, S_0, M_{S_0}, T_0, T_{3_0}, l_\Lambda, l_N, \vec{P}, \vec{k})$ . However, we still need to explicitly write the initial and final two-body wave functions. As we already mentioned, for the initial  $\Lambda$  and nucleon states we take the solutions of a harmonic oscillator mean field potential. In writing the relative and center of mass  $\Lambda N$  wave functions, we use an average parameter  $b = \frac{b_\Lambda + b_N}{2}$ , where  $b_\Lambda = 1.87$  fm and  $b_N = 1.64$  fm are such that the corresponding hypernuclear and core binding energies are reproduced. While the  $\Lambda$  is assumed to be always in an s-shell, the nucleon might be in an s-shell or in a p-shell. Expressing the initial two-body wave function in center of mass and relative coordinates we have, for an s-shell nucleon:

$$\Phi_{100}^\Lambda\left(\frac{\vec{r}_1}{b_\Lambda}\right) \Phi_{100}^N\left(\frac{\vec{r}_2}{b_N}\right) = \Phi_{100}^{rel}\left(\frac{\vec{r}}{\sqrt{2}b}\right) \Phi_{100}^{CM}\left(\frac{\vec{R}}{b/\sqrt{2}}\right), \quad (2.8)$$

and for a p-shell nucleon:

$$\Phi_{100}^\Lambda\left(\frac{\vec{r}_1}{b_\Lambda}\right) \Phi_{11m}^N\left(\frac{\vec{r}_2}{b_N}\right) = \frac{1}{\sqrt{2}} \left\{ \Phi_{100}^{rel}\left(\frac{\vec{r}}{\sqrt{2}b}\right) \Phi_{11m}^{CM}\left(\frac{\vec{R}}{b/\sqrt{2}}\right) - \Phi_{11m}^{rel}\left(\frac{\vec{r}}{\sqrt{2}b}\right) \Phi_{100}^{CM}\left(\frac{\vec{R}}{b/\sqrt{2}}\right) \right\}. \quad (2.9)$$

The coefficients relating the wave functions in both coordinate systems and for a general shell (N) and angular momentum (L) are called Moshinsky brackets,  $X(N_r L_r N_R L_R, l_\Lambda l_N)$  [65]. We can write the two-body transition of Eq. (2.4) as a function of these coefficients and of the relative and center of mass momentum,

$$t_{\Lambda N \rightarrow NN} = \sum_{N_r L_r N_R L_R} X(N_r L_r N_R L_R, l_\Lambda l_N) t_{\Lambda N \rightarrow NN}^{N_r L_r N_R L_R}. \quad (2.10)$$

Using this model, the initial  $\Lambda$  and nucleon are assumed to be independent. To account for the strong correlation between the two interacting baryons we replace the harmonic oscillator wave function,  $\Phi^{rel}(\vec{r})$ , by a correlated  $\Lambda N$  wave function which simulates the result of a G-matrix calculation for  ${}^5_\Lambda He$  [66]. This calculation solves a finite-nucleus G-matrix using the soft-core and hard-core Nijmegen models of Refs. [67] and [68]. We follow the approach of Ref. [17], where it is shown that the use of a correlation function of the type

$$f_{\Lambda N}(r) = (1 - e^{-r^2/a^2})^n + br^2 e^{-r^2/c^2} \quad (2.11)$$

produces correlated wave functions in between the results of Ref. [66] for these two potential models. The values of  $a = 0.5$  fm,  $b = 0.25$  fm,  $c = 1.28$  fm and  $n = 2$  give results between those obtained from numerical Nijmegen soft-core correlations and those obtained with the Nijmegen hard-core potential, in both spin channels,  ${}^1S_0$  and  ${}^3S_1$ .

### 2.1.5 Final $NN$ wave function

We now describe the two-body final state. The wave function for two outgoing free nucleons is, in particle coordinates,

$$\left\langle \vec{r}_1 \vec{r}_2 | \vec{k}_1 \vec{k}_2 s_1 m_{s_1}, s_2 m_{s_2}, t_1 m_{t_1}, t_2 m_{t_2} \right\rangle = e^{i\vec{k}_1 \cdot \vec{r}_1} e^{i\vec{k}_2 \cdot \vec{r}_2} \chi_{m_{s_1}}^{s_1} \chi_{m_{s_2}}^{s_2} \chi_{m_{t_1}}^{t_1} \chi_{m_{t_2}}^{t_2}. \quad (2.12)$$

The four  $\chi$ 's denote the spin and isospin states of each of the two particles. In relative ( $\vec{k}$ ,  $\vec{r}$ ) and center of mass ( $\vec{P}$ ,  $\vec{R}$ ) coordinates we have

$$\left\langle \vec{R} \vec{r} | \vec{P} \vec{k} S M_S T M_T \right\rangle = e^{i\vec{P} \cdot \vec{R}} e^{i\vec{k} \cdot \vec{r}} \chi_{M_S}^S \chi_{M_T}^T. \quad (2.13)$$

To antisymmetrize it we must exchange the coordinates and quantum numbers of the two nucleons. In relative and center of mass coordinates this translates into exchanging  $\vec{k} \rightarrow -\vec{k}$  and including a factor  $(-1)^{S+T}$ . Thus, the antisymmetrized wave function is

$$\left\langle \vec{R} \vec{r} | \vec{P} \vec{k} S M_S T M_T \right\rangle = \frac{1}{\sqrt{2}} e^{i\vec{P} \cdot \vec{R}} \left( e^{i\vec{k} \cdot \vec{r}} - (-1)^{S+T} e^{-i\vec{k} \cdot \vec{r}} \right) \chi_{M_S}^S \chi_{M_T}^T, \quad (2.14)$$

where the first and second terms represent the direct and exchanged contributions to  $\Lambda N \rightarrow NN$  process. The nucleons, though, are not free but interact among themselves and with the medium. In our description we only incorporate the strong force among the two nucleons. The Schrödinger equation with a Hamiltonian  $H = H_0 + V$  can be expressed as the Lippmann-Schwinger equation,

$$|\Psi^{(\pm)}\rangle = |\phi\rangle + \frac{1}{E - H_0 \pm i\epsilon} V |\Psi^{(\pm)}\rangle, \quad (2.15)$$

where  $|\phi\rangle$  represents a solution of the free Hamiltonian  $H_0$ , and  $E$  is the energy of the two-nucleon state  $|\Psi^{(\pm)}\rangle$ . The plus and minus signs denote states at an infinite time before and after the interaction. Defining  $V |\Psi^{(\pm)}\rangle \equiv T |\phi\rangle$  one obtains the T-matrix equation,

$$T = V + V \frac{1}{E - H_0 \pm i\epsilon} T. \quad (2.16)$$

We solve this T-matrix equation with two different potential models, Nijmegen Soft-Core 97f [67, 68] and the one from the Jülich group [69]. Once the T-matrix equation is computed, we can use the definition  $V |\Psi^{(\pm)}\rangle \equiv T |\phi\rangle$  and Eq. (2.15) to obtain the correlated NN wave function, which in relative and center of mass coordinates, we denote as  $\Psi_{\vec{k}}$ . Thus, the final nucleon-nucleon wave function is obtained by replacing

$$e^{i\vec{k} \cdot \vec{r}} \rightarrow \Psi_{\vec{k}}(\vec{r}) \quad (2.17)$$

in Eq. (2.13). Finally, the matrix element of Eq. (2.10) for the direct contribution and in momentum space is

$$\begin{aligned} t_{\Lambda N \rightarrow NN}^{N_r L_r N_R L_R} &= \frac{1}{\sqrt{2}} \int d^3 R \int d^3 r e^{-i\vec{P} \cdot \vec{R}} \Psi_{\vec{k}}^*(\vec{r}) \chi_{M_S}^{\dagger S} \chi_{T_3}^{\dagger T} V(\vec{r}) \Phi_{N_R L_R}^{CM} \left( \frac{\vec{R}}{b/\sqrt{2}} \right) \\ &\times \Phi_{N_r L_r}^{rel} \left( \frac{\vec{r}}{\sqrt{2b}} \right) \chi_{M_{S_0}}^{S_0} \chi_{T_{3_0}}^{T_0}. \end{aligned} \quad (2.18)$$

### 2.1.6 Asymmetry

The kinematical conditions of the hypernuclear experiments carried out at Brookhaven (USA) [70] and KEK (Japan) [71], through the reactions  $n(K^-, \pi^-)\Lambda$  and  $n(\pi^+, K^+)\Lambda$ , also allow to extract information about the angular distribution of the outgoing protons with respect to the polarization axis. Due to an interference between the PV and PC amplitudes, there is an angular asymmetry in the intensity of outgoing protons,  $I(\chi)$ , where  $\chi$  is the angle of the proton with respect to the polarization axis. A schematic representation for the  $n(\pi^+, K^+)\Lambda$  reaction is shown in Fig. 2.1. In this section we outline the steps to obtain this asymmetry in terms of the two-body amplitudes. A more complete calculation can be found in the Appendix B of Ref. [72].

For a hypernucleus polarized in the  $y$ -axis, the asymmetry,  $A_p(\chi)$ , is defined by

$$I(\chi) = I_0(1 + P_y A_p(\chi)), \quad (2.19)$$

where  $P_y$  is the hypernuclear polarization created in the production reaction. The asymmetry is given in terms of the transition matrix element  $\mathcal{M}$ , the spin operator in the polarization axis,  $\hat{S}_y$ , and the total spin,  $J$ ,

$$A_p(\chi) = \frac{3}{J+1} \frac{\text{Tr}(\mathcal{M} \hat{S}_y \mathcal{M}^\dagger)}{\text{Tr}(\mathcal{M} \mathcal{M}^\dagger)}. \quad (2.20)$$

For pure vector polarization, this asymmetry only depends on  $\cos(\chi)$  and on the intensities of the outgoing protons with spin projections  $M_i$ ,  $I(M_i)$ :

$$A_p(\chi) = \frac{3}{J+1} \frac{\sum_{M_i} I(M_i) M_i}{\sum_{M_i} I(M_i)} \cos(\chi) = A_p \cos(\chi), \quad (2.21)$$

where  $A_p$  is the asymmetry parameter characteristic of the hypernuclear weak decay. The asymmetry of the proton distribution is then determined by  $P_y A_p$ . In the weak coupling

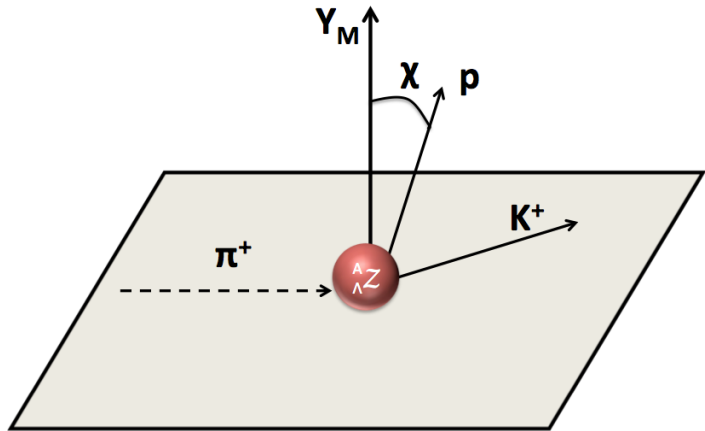


Figure 2.1: Schematic representation of the  $n(\pi^+, K^+)\Lambda$  reaction.  $Y_M$  is the polarization axis, and  $\chi$  is the angle between  $Y_M$  and the direction of the outgoing protons.

scheme, where  $l_\Lambda = 0$ , we can easily relate the hypernuclear polarization  $P_y$  with the  $\Lambda$  polarization  $p_\Lambda$ ,

$$p_\Lambda = \begin{cases} -\frac{J}{J+1}P_y & \text{if } J = J_C - \frac{1}{2} \\ P_y & \text{if } J = J_C + \frac{1}{2} \end{cases}. \quad (2.22)$$

Finally, we define the intrinsic parameter  $a_\Lambda$ , such that it fulfills  $P_y A_p = p_\Lambda a_\Lambda$  and that is characteristic of the  $\Lambda N \rightarrow NN$  transition:

$$a_\Lambda = \begin{cases} -\frac{J+1}{J}A_p & \text{if } J = J_C - \frac{1}{2} \\ A_p & \text{if } J = J_C + \frac{1}{2} \end{cases}. \quad (2.23)$$

## 2.2 Hypertriton

In this section we describe the formalism for the non-mesonic decay rate of the hypertriton. The hypertriton is a bound state of a proton, a neutron and a  $\Lambda$  with positive parity, total isospin zero, and total spin  $J_3 = \frac{1}{2}$ . The fact that the hypertriton is made of only three particles allows us to describe the initial and final strong interactions contributing to the decay by explicitly taking into account the two and three-body interactions among the three baryons.

The initial wave function is calculated using strong effective field theory NLO  $YN$  [54, 55] and NNLO  $NN$  potentials [46, 47] such that the hypertriton binding energy is reproduced. The final state which results from the non-mesonic decay of the hypertriton can be either three free nucleons ( $3N$  break up) or a deuteron and a free neutron ( $d+n$  break up). The interactions among the final three baryons are also calculated using strong NNLO EFT nucleon-nucleon potentials.

The strong Hamiltonian used in the following formalism is separated into a term containing the kinetic energy,  $H_0$ , and the strong potential,  $V_s$ . The strong potential contains three terms  $V_{ij}$  accounting for the strong forces between the three possible pairs  $i - j$ , where  $i, j = 1, 2, 3$ . It is also convenient to separate the three body force into three terms,  $V_{ijk}^{(l)}$ , such that they are symmetric with respect to the exchange of the particles other than  $l$ ,

$$\begin{aligned} H &= H_0 + V_s \\ &= H_0 + V_{12} + V_{13} + V_{23} + V_{123}^{(1)} + V_{123}^{(2)} + V_{123}^{(3)}. \end{aligned} \quad (2.24)$$

### 2.2.1 Decay rate formula

To calculate the decay rate, we must average the initial spin projections ( $\frac{1}{2J_3+1} \sum_{m_{J_3}}$ ) and sum and integrate over final spin projections ( $m_d$  and  $m_n$  for the  $d+n$  break up and  $m_1$ ,  $m_2$  and  $m_3$  for the  $3N$  break up) and momenta ( $\vec{k}_d$  and  $\vec{k}_n$  for the  $d+n$  break up and  $\vec{k}_1$ ,  $\vec{k}_2$  and  $\vec{k}_3$  for the  $3N$  break up). In the center of mass frame, the decay rates for the two

possible final states are:

$$d\Gamma^{d+n} = \frac{1}{2} \sum_{m_{J_3}} \sum_{m_d m_n} \left| \langle \Psi_{m_d m_n}^{(-)} | V^w | \psi_{\Lambda H}^3 \rangle \right|^2 \times d^3 k_d d^3 k_n (2\pi) \delta^3(\vec{k}_d + \vec{k}_n) \delta \left( M_{\Lambda H}^3 - M_d - M_N - \frac{\vec{k}_d^2}{2M_d} - \frac{\vec{k}_n^2}{2M_N} \right), \quad (2.25)$$

$$d\Gamma^{3N} = \frac{1}{2} \sum_{m_{J_3}} \sum_{m_1 m_2 m_3} \left| \langle \Psi_{m_1 m_2 m_3}^{(-)} | V^w | \psi_{\Lambda H}^3 \rangle \right|^2 \times d^3 k_1 d^3 k_2 d^3 k_3 (2\pi) \delta^3(\vec{k}_1 + \vec{k}_2 + \vec{k}_3) \delta \left( M_{\Lambda H}^3 - 3M_N - \frac{\vec{k}_1^2}{2M_N} - \frac{\vec{k}_2^2}{2M_N} - \frac{\vec{k}_3^2}{2M_N} \right), \quad (2.26)$$

where  $M_{\Lambda H}$  is the mass of the hypertriton,  $M_N$  is the mass of the nucleon,  $\psi_{\Lambda H}^3$  is the wave function of the hypertriton and  $\Psi^{(-)}$  is the outgoing wave function.  $V_w$  denotes the potential driving the weak  $\Lambda N \rightarrow NN$  transition. We now change to Jacobi coordinates, which in position space are the relative and center of mass coordinates. For three particles at positions  $x_1$ ,  $x_2$  and  $x_3$  and with masses  $m_1$ ,  $m_2$  and  $m_3$  they are defined as

$$\begin{aligned} \vec{r}_{12} &\equiv \vec{x}_1 - \vec{x}_2, \\ \vec{r}_3 &\equiv \vec{x}_3 - \frac{1}{m_1 + m_2} (m_1 \vec{x}_1 + m_2 \vec{x}_2) \\ \vec{r}_{CM} &\equiv \frac{1}{m_1 + m_2 + m_3} (\vec{x}_1 + \vec{x}_2 + \vec{x}_3). \end{aligned} \quad (2.27)$$

These coordinates are represented in Fig. 2.2. The corresponding Jacobi momenta are

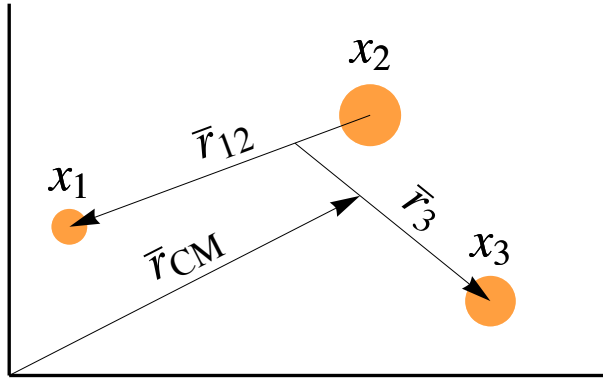


Figure 2.2: Representation of the Jacobi coordinates,  $\vec{r}_{12}$ ,  $\vec{r}_3$  and  $\vec{r}_{CM}$ , for three particles at positions  $x_1$ ,  $x_2$  and  $x_3$ . The masses of the particles are proportional to the areas of the circles representing them.

defined as

$$\begin{aligned}\vec{p}_{12} &\equiv \frac{1}{m_1 + m_2} (m_2 \vec{k}_1 - m_1 \vec{k}_2), \\ \vec{p}_3 &\equiv \frac{1}{m_1 + m_2 + m_3} \left[ (m_1 + m_2) \vec{k}_3 - m_3 (\vec{k}_1 + \vec{k}_2) \right], \\ \vec{p}_{CM} &\equiv \vec{k}_1 + \vec{k}_2 + \vec{k}_3.\end{aligned}\quad (2.28)$$

Using these coordinates and defining  $M_{\Lambda H} = 2M_N + M_\Lambda + \epsilon$  and  $M_d = 2M_N + \epsilon_d$  (where  $\epsilon < 0$  and  $\epsilon_d < 0$ ) we obtain

$$\begin{aligned}d\Gamma^{d+n} &= \frac{1}{2} \sum_{m_{J_3}} \sum_{m_{j_{12}} m_3} \left| \langle \Psi_{m_{j_{12}} m_3}^{(-)} | V^w | \psi_{\Lambda H}^3 \rangle \right|^2 \\ &\times d^3 p_{CM} d^3 p_3 (2\pi) \delta^3(\vec{p}_{CM}) \delta \left( M_\Lambda - M_N + \epsilon - \epsilon_d - \frac{3}{4} \frac{\vec{p}_3^2}{M_N} - \frac{\vec{p}_{CM}^2}{6M_N} \right),\end{aligned}\quad (2.29)$$

$$\begin{aligned}d\Gamma^{3N} &= \frac{1}{2} \sum_{m_{J_3}} \sum_{m_1 m_2 m_3} \left| \langle \Psi_{m_1 m_2 m_3}^{(-)} | V^w | \psi_{\Lambda H}^3 \rangle \right|^2 \\ &\times d^3 p_{12} d^3 p_3 d^3 p_{CM} (2\pi) \delta^3(\vec{p}_{CM}) \delta \left( M_\Lambda - M_N + \epsilon - \frac{\vec{p}_{12}^2}{M_N} - \frac{3}{4} \frac{\vec{p}_3^2}{M_N} - \frac{1}{6} \frac{\vec{p}_{CM}^2}{M_N} \right).\end{aligned}\quad (2.30)$$

We have identified  $\vec{k}_d = \vec{k}_1 + \vec{k}_2$ ,  $m_d = m_{j_{12}}$  and  $\vec{k}_n = \vec{k}_3$ ,  $m_n = m_3$ . Integrating  $\vec{p}_{CM}$  and the modulus of  $\vec{p}_3$ , we get

$$d\Gamma^{d+n} = \frac{1}{2} \sum_{m_{J_3}} \sum_{m_{j_{12}} m_3} \left| \langle \Psi_{m_{j_{12}} m_3}^{(-)} | V^w | \psi_{\Lambda H}^3 \rangle \right|^2 d\hat{p}_3 (2\pi) \frac{2M_N}{3} p_3^{(d+n)}, \quad (2.31)$$

$$d\Gamma^{3N} = \frac{1}{2} \sum_{m_{J_3}} \sum_{m_1 m_2 m_3} \left| \langle \Psi_{m_1 m_2 m_3}^{(-)} | V^w | \psi_{\Lambda H}^3 \rangle \right|^2 p_{12}^2 dp_{12} d\hat{p}_{12} d\hat{p}_3 (2\pi) \frac{2M_N}{3} p_3^{(3N)}, \quad (2.32)$$

with  $p_3^{(d+n)} \equiv \sqrt{\frac{4M_N}{3} (\Delta M + \epsilon - \epsilon_d)}$ ,  $p_3^{(3N)} \equiv \sqrt{\frac{4M_N}{3} (\epsilon + \Delta M - \frac{\vec{p}_{12}^2}{M_N})}$  and  $\Delta M \equiv M_\Lambda - M_N$ . The  $3N$  break up still depends on  $p_{12}$ , which has the upper limit of

$$p_{12} = \sqrt{M_N(\epsilon + \Delta M)}. \quad (2.33)$$

Above this limit the delta gives zero. Also, both decay rates still depend on an angular part. Because of the average over spin projections, the squared matrix element for the  $d + n$  break up does not depend on  $\hat{p}_3$ , and for the  $3N$  break up it only depends on the angle between  $\vec{p}_3$  and  $\vec{p}_{12}$ , which we define as  $\theta$ . Integrating the angular parts (except  $\theta$  for the  $3N$  break up), the decay rates are

$$d\Gamma^{d+n} = 8\pi^2 \frac{2M_N}{3} p_3^{(d+n)} \frac{1}{2} \sum_{m_{J_3}} \sum_{m_{j_{12}} m_3} \left| \langle \Psi_{m_{j_{12}} m_3}^{(-)} | V^w | \psi_{\Lambda H}^3 \rangle \right|^2, \quad (2.34)$$

$$d\Gamma^{3N} = 16\pi^3 \frac{2M_N}{3} p_3^{(3N)} p_{12}^2 dp_{12} \sin(\theta) d\theta \frac{1}{2} \sum_{m_{J_3}} \sum_{m_1, m_2, m_3} \left| \langle \Psi_{m_1 m_2 m_3}^{(-)} | V^w | \psi_{\Lambda H}^3 \rangle \right|^2. \quad (2.35)$$

### 2.2.2 Final state wave function

The wave function for the final state consists of  $d + n$  or  $3N$  states that evolve under the influence of the strong force. The asymptotically free states, normalized and antisymmetrized, are defined as

$$\langle \Psi_{\text{free}} | \mathcal{N} \mathcal{A}, \quad (2.36)$$

where  $\langle \Psi_{\text{free}} |$  is the three-particle non-antisymmetrized state,  $\mathcal{N}$  is the normalization constant and  $\mathcal{A}$  the antisymmetry operator.  $\mathcal{N} \equiv \sqrt{\frac{N!}{\nu_1! \nu_2! \dots}}$  depends on the total number of particles ( $N$ ) and on the number of particles in each bound state ( $\nu_i$ ), and takes into account all the possible configurations in the final state. For the  $d + n$  state we have  $\mathcal{N} = \sqrt{3}$  and for  $3N$ ,  $\mathcal{N} = \sqrt{6}$ . The antisymmetrization operator is defined as

$$\mathcal{A} \equiv \frac{1}{6} (1 + P_{12}P_{23} + P_{13}P_{23}) (1 - P_{12}), \quad (2.37)$$

where  $P_{ij}$  exchanges the coordinates and quantum numbers of particles  $i$  and  $j$ . In order to obtain the evolution of the free and antisymmetrized states,  $d + n$  and  $3N$ , we separate the Hamiltonian into two parts,  $H_1$  and  $H_2$ , such that  $\frac{i\epsilon}{E + i\epsilon - H_1} |\Psi_{\text{free}}\rangle = |\Psi_{\text{free}}\rangle$ . For the  $3N$  wave function  $H_1$  is just the kinetic energy part,  $H_0$ , while for the  $d + n$  we have to take into account the two-body interaction between the hyperon and the nucleon in the deuteron, labeled with 1 and 2, i.e.  $H_1 = H_0 - V_{12}$ . We then define the corresponding identities,

$$\frac{1}{E - H} = \frac{1}{E - H_0} + \frac{1}{E - H_0} V_s \frac{1}{E - H}, \quad (2.38)$$

$$\frac{1}{E - H} = \frac{1}{E - H_0 - V_{12}} + \frac{1}{E - H_0 - V_{12}} (V_s - V_{12}) \frac{1}{E - H}. \quad (2.39)$$

Applying these identities to the  $d + n$  and  $3N$  free states, we obtain the corresponding evolved states,

$$\left\langle \Psi_{d+n}^{(-)} \right| = \langle \Psi | \frac{+i\epsilon}{E + i\epsilon - H} = \langle \Psi | \left( 1 + (V_s - V_{12}) \frac{1}{E + i\epsilon - H} \right), \quad (2.40)$$

$$\left\langle \Psi_{3N}^{(-)} \right| = \langle \Psi | \frac{+i\epsilon}{E + i\epsilon - H} = \langle \Psi | \left( 1 + V_s \frac{1}{E + i\epsilon - H} \right). \quad (2.41)$$

Thus, we can write the decay rate formulas as

$$d\Gamma^{d+n} = 24\pi^2 \frac{2M_N}{3} p_3^{(d+n)} \frac{1}{2} \sum_{m_{J_3}} \sum_{m_{j_{12}} m_3} \left| \langle \Psi_{m_{j_{12}} m_3} | \left( 1 + (V_s - V_{12}) \frac{1}{E + i\epsilon - H} \right) \mathcal{A} V^w | \psi_{\Lambda H}^3 \rangle \right|^2, \quad (2.42)$$

$$d\Gamma^{3N} = 96\pi^3 \frac{2M_N}{3} p_3^{(3N)} p_{12}^2 d\theta \sin(\theta) d\theta \times \frac{1}{2} \sum_{m_{J_3}} \sum_{m_1, m_2, m_3} \left| \langle \Psi_{m_1 m_2 m_3} | \left( 1 + V_s \frac{1}{E + i\epsilon - H} \right) \mathcal{A} V^w | \psi_{\Lambda H}^3 \rangle \right|^2. \quad (2.43)$$

The weak potential  $V^w \equiv V_{12}^w + V_{13}^w$  mediates the transition from a  $\Lambda$  (labeled with 1) and a nucleon (labeled with 2 or 3) to two nucleons. Since the states on the left and the right of  $V^w$  are antisymmetric with respect to the nucleons 2 and 3 we can simplify the weak potential potential so that we only have one term,

$$V_{12}^w + V_{13}^w = V_{12}^w + P_{23}V_{12}^wP_{23} \rightarrow V_{12}^w + (-1)V_{12}^w(-1) = 2V_{12}^w. \quad (2.44)$$

Moreover, working with a basis of states that is antisymmetric in particles 1 and 2, we can effectively replace  $P_{12}$  by  $-1$ , and thus

$$1 - P_{12} \rightarrow 2. \quad (2.45)$$

Finally, we also simplify  $(1 + P_{12}P_{23} + P_{13}P_{23})$  by applying  $P_{12}$  in both sides,

$$1 + P_{12}P_{23} + P_{13}P_{23} \rightarrow 1 + P_{12}P_{23} + P_{12}P_{13}P_{23}P_{12} = 1 + 2P_{12}P_{23} \equiv 1 + P. \quad (2.46)$$

Note that we have defined  $P \equiv 2P_{12}P_{23}$ . Therefore, the quantity  $\mathcal{A}V^w$  can be simplified to

$$\mathcal{A}V^w = \frac{2}{3}(1 + P)V_{12}^w,$$

and the decay rates are then

$$d\Gamma^{d+n} = \frac{32}{9}\pi^2 M_N p_3^{(d+n)} \sum_{m_{J_3}} \sum_{m_{j_{12}}, m_3} \left| \langle \Psi_{m_{j_{12}} m_3} | \left( 1 + (V_s - V_{12}) \frac{1}{E + i\epsilon - H} \right) (1 + P)V_{12}^w | \psi_{\Lambda H}^3 \rangle \right|^2, \quad (2.47)$$

$$d\Gamma^{3N} = \frac{128}{9}\pi^3 M_N p_3^{(3N)} p_{12}^2 d\theta \sin(\theta) \sum_{m_{J_3}} \sum_{m_1, m_2, m_3} \left| \langle \Psi_{m_1 m_2 m_3} | \left( 1 + V_s \frac{1}{E + i\epsilon - H} \right) (1 + P)V_{12}^w | \psi_{\Lambda H}^3 \rangle \right|^2. \quad (2.48)$$

We now use the permutation operators to simplify the strong potential. For the  $d + n$  decay rate we have

$$V_s - V_{12} = V_{13} + V_{23} + V_{123}^{(1)} + V_{123}^{(2)} + V_{123}^{(3)} \quad (2.49)$$

$$= P(V_{12} + V_{123}^{(3)}) + V_{123}^{(3)}, \quad (2.50)$$

and for  $3N$ ,

$$V_s = V_{12} + V_{13} + V_{23} + V_{123}^{(1)} + V_{123}^{(2)} + V_{123}^{(3)} \quad (2.51)$$

$$= (1 + P)(V_{12} + V_{123}^{(3)}). \quad (2.52)$$

Using these identities and defining the following rescattering state,

$$|U\rangle \equiv \left( V_{12} + V_{123}^{(3)} \frac{1}{E + i\epsilon - H} \right) (1 + P)V_{12}^w | \psi_{\Lambda H}^3 \rangle, \quad (2.53)$$

the decay rates become

$$\begin{aligned} d\Gamma^{d+n} = & \frac{32}{9}\pi^2 M_N p_3^{(d+n)} \sum_{m_{J_3}} \sum_{m_{j_{12}} m_3} \left| \langle \Psi_{m_{j_{12}} m_3} | (1 + P) V_{12}^w | \psi_{\Lambda H}^3 \rangle + \langle \Psi_{m_{j_{12}} m_3} | P | U \rangle \right. \\ & \left. + \langle \Psi_{m_{j_{12}} m_3} | V_{123}^{(3)} \frac{1}{E + i\epsilon - H} (1 + P) V_{12}^w | \psi_{\Lambda H}^3 \rangle \right|^2, \\ = & \frac{32}{9}\pi^2 M_N p_3^{(d+n)} \sum_{m_{J_3}} \sum_{m_{j_{12}} m_3} \left| \langle \Psi_{m_{j_{12}} m_3} | \left( 1 + V_{123}^{(3)} G_0 \right) (1 + P) V_{12}^w | \psi_{\Lambda H}^3 \rangle \right. \\ & \left. + \langle \Psi_{m_{j_{12}} m_3} | \left( P + V_{123}^{(3)} G_0 (1 + P) \right) | U \rangle \right|^2, \end{aligned} \quad (2.54)$$

$$\begin{aligned} d\Gamma^{3N} = & \frac{128}{9}\pi^3 M_N p_3^{(3N)} p_{12}^2 dp_{12} \sin(\theta) d\theta \\ & \times \sum_{m_{J_3}} \sum_{m_1, m_2, m_3} \left| \langle \Psi_{m_1 m_2 m_3} | (1 + P) V_{12}^w | \psi_{\Lambda H}^3 \rangle + \langle \Psi_{m_1 m_2 m_3} | (1 + P) | U \rangle \right|^2. \end{aligned} \quad (2.55)$$

In the second step of Eq. (2.54) we have used again the identity defined in Eq. (2.38) and we have defined  $G_0 \equiv \frac{1}{E + i\epsilon - H_0}$ .

We have written the matrix elements for both decays as a sum of a plane-wave part, where no strong interactions are accounted for, and a rescattering part, which contains the state  $|U\rangle$ .

### 2.2.3 Final state interaction: the rescattering part

We now focus on how to solve the rescattering state,  $|U\rangle$ , given the plane-wave one,  $(1 + P) V_{12}^w | \psi_{\Lambda H}^3 \rangle$ . The strong effective potential consists of two and three-body terms. The three body interaction can be expressed as a sum of three terms of type  $V^{(k)}$  such that they are symmetric with respect to the exchange of the particles other than  $k$ . Using this we have,

$$\begin{aligned} V_s(1 + P) &= \left[ (V_{12} + V_{123}^{(3)}) + (V_{13} + V_{123}^{(2)}) + (V_{23} + V_{123}^{(1)}) \right] (1 + P) \\ &= (1 + P)(V_{12} + V_{123}^{(3)})(1 + P). \end{aligned}$$

Applying this equality and the resolvent identity, we obtain the following iterative equation for the rescattering part  $|U\rangle$ ,

$$\begin{aligned} |U\rangle &\equiv (V_{12} + V_{123}^{(3)}) \frac{1}{E + i\epsilon - H} (1 + P) V_{12}^w | \phi_{\Lambda H}^3 \rangle \\ &= (V_{12} + V_{123}^{(3)}) \frac{1}{E + i\epsilon - H_0} (1 + P) V_{12}^w | \phi_{\Lambda H}^3 \rangle \\ &\quad + (V_{12} + V_{123}^{(3)}) \frac{1}{E + i\epsilon - H_0} (1 + P) (V_{12} + V_{123}^{(3)}) \frac{1}{E + i\epsilon - H} (1 + P) V_{12}^w | \phi_{\Lambda H}^3 \rangle \\ &= (V_{12} + V_{123}^{(3)}) \frac{1}{E + i\epsilon - H_0} (1 + P) V_{12}^w | \phi_{\Lambda H}^3 \rangle + (V_{12} + V_{123}^{(3)}) \frac{1}{E + i\epsilon - H_0} (1 + P) | U \rangle. \end{aligned} \quad (2.56)$$

To solve for  $|U\rangle$  we first solve the two-body force using the following t-matrix equation

$$(1 + t_{12}G_0)(1 - V_{12}G_0) = 1, \quad (2.57)$$

with  $G_0 \equiv \frac{1}{E + i\epsilon - H_0}$ , and then solve the iterative equation containing (one third of) the three-body force,

$$\begin{aligned} |U\rangle = & t_{12}G_0(1 + P)V_{12}^w|\phi_{\Lambda H}^3\rangle + (1 + t_{12}G_0)V_{123}^{(3)}G_0(1 + P)V_{12}^w|\phi_{\Lambda H}^3\rangle \\ & + t_{12}G_0P|U\rangle + (1 + t_{12}G_0)V_{123}^{(3)}G_0(1 + P)|U\rangle. \end{aligned} \quad (2.58)$$

Once  $|U\rangle$  is solved, we can insert it in the matrix elements of Eqs. 2.54 and 2.55 and compute the decay rates.

### 2.2.4 Basis of three-body states: $|\alpha, p_{12}, p_3\rangle$

To compute the matrix elements we use the following basis of states

$$|p_{12}, p_3, \alpha\rangle = |p_{12}, p_3\rangle \left| [(l_{12}s_{12})j_{12}(l_3 \frac{1}{2})I_3]J_3 \right\rangle \left| (t_{12} \frac{1}{2})T_3 M_{T_3} \right\rangle. \quad (2.59)$$

We have defined the different quantum numbers as follows:  $l_{12}$  and  $s_{12}$  are the relative angular momenta and spin between particles 1 and 2, and which are coupled to  $j_{12}$ ;  $l_3$  and  $\frac{1}{2}$  are the angular momentum (with respect to the center of mass of particles 1 and 2) and the spin of particle 3, which couple to  $I_3$ . The total spin and its third component are  $J_3$  and  $m_{J_3}$ . Similarly, the isospin of particles 1 and 2 is  $t_{12}$ , which coupled to the isospin of the third particle,  $\frac{1}{2}$ , gives a total isospin  $|T_3, M_{T_3}\rangle$ . As for the momenta states we use the normalization

$$\langle \vec{p} | \vec{p}' \rangle = \delta^3(\vec{p} - \vec{p}'). \quad (2.60)$$

Thus, the hypertriton wave function has the form

$$\left| \psi_{\Lambda H}^3 \right\rangle = \sum_{\alpha} \int d^3 p_{12} d^3 p_3 \phi_{\alpha}(p_{12}, p_3) |p_{12}, p_3, \alpha\rangle, \quad (2.61)$$

where  $\phi_{\alpha}(p_{12}, p_3)$  accounts for the dependence on the momenta and quantum numbers of the interacting baryons. In particular, the hypertriton wave function has positive parity and total spin and isospin  $J_3 = \frac{1}{2}$  and  $|T_3, M_{T_3}\rangle = |0, 0\rangle$ .

Using the same notation, the  $d + n$  and  $3N$  states are defined as

$$\left| \Psi_{m_{j_{12}}^d m_3} \right\rangle = \sum_{l_{12}^d} \int dp_{12}^d p_{12}^{d/2} \phi_{l_{12}^d}(p_{12}^d) |p_{12}^d, (l_{12}^d s_{12}^d) j_{12}^d m_{j_{12}}^d, t_{12}^d m_{t_{12}}^d\rangle |\vec{p}_3, m_3, m_{t_3}^n\rangle, \quad (2.62)$$

$$|\Psi_{m_1 m_2 m_3}\rangle = |\vec{p}_{12} \vec{p}_3, m_1 m_2 m_3, m_{t_1} m_{t_2} m_{t_3}\rangle, \quad (2.63)$$

where the quantum numbers for the deuteron and the neutron are:  $l_{12}^d, m_{l_{12}}^d, s_{12}^d = 1, m_{s_{12}}^d, t_{12}^d = 0, m_{t_{12}}^d = 0, m_{t_3}^n = -\frac{1}{2}$ ; and where the dependence of the deuteron wave function on  $p_{12}$  and  $l_{12}$  is encapsulated in  $\phi_{l_{12}}(p_{12})$ . The modulus  $\vec{p}_3$  is determined by the

mass difference and the binding energies,  $p_3 = p_3^{(d+n)} \equiv \sqrt{\frac{4M_N}{3}(\Delta M + \epsilon - \epsilon_d)}$ , while the orientation  $\hat{p}_3$  is fixed to any value, since the decay does not depend on it (see end of Sec. 2.2.1). Two of the isospins of the 3 nucleons,  $m_{t_1}$ ,  $m_{t_2}$ ,  $m_{t_3}$ , must be  $-\frac{1}{2}$ , and the other one  $\frac{1}{2}$ . Finally, we can insert a complete set of  $|p_{12}, p_3, \alpha\rangle$  states to obtain the  $d+n$  and  $3N$  wave functions in the same basis as in the hypertriton wave function:

$$\begin{aligned} |\Psi_{m_{j_{12}} m_3}\rangle &= \sum_{l_{12}^d} \int dp_{12}^d p_{12}^{d^2} \sum_{\alpha, m_{J_3}} \int dp_{12} p_{12}^2 dp_3 p_3^2 \phi_{l_{12}^d}(p_{12}) |p_{12}, p_3, \alpha m_{J_3}\rangle, \\ &\quad \times \langle p_{12}, p_3, \alpha m_{J_3} | p_{12}^d, (l_{12}^d s_{12}) j_{12}^d m_{j_{12}}^d, t_{12}^d m_{t_{12}}^d \rangle |\vec{p}_3, m_3, m_{t_3}^n\rangle \\ &= \sum_{\alpha, m_{J_3}} \int dp_{12} p_{12}^2 \phi_{l_{12}}(p_{12}) Y_{l_3 m_{J_3} - m_{j_{12}}^d - m_3}(\hat{p}_3) |p_{12}, p_3, \alpha m_{J_3}\rangle \\ &\quad \times (j_{12} I_3 J_3, m_{j_{12}} m_{J_3} - m_{j_{12}} m_{J_3})(l_3 \frac{1}{2} I_3, m_{J_3} - m_{j_{12}}^d - m_3 m_3 m_{J_3} - m_{j_{12}}^d) \\ &\quad \times \delta_{t_{12}0} \delta_{m_{t_{12}}0} \delta_{M_{T_3}-1/2} \delta_{j_{12}1} \delta_{m_{j_{12}} m_{j_{12}}^d} \delta_{l_{12} l_{12}^d} \delta_{s_{12}0}, \end{aligned} \quad (2.64)$$

$$\begin{aligned} |\Psi_{m_1 m_2 m_3}\rangle &= \sum_{\alpha, m_{J_3}} \int dp'_{12} p'_{12}^2 dp'_3 p'_3^2 \langle p'_{12}, p'_3, \alpha m_{J_3} | \vec{p}_{12} \vec{p}_3, m_1 m_2 m_3, m_{t_1} m_{t_2} m_{t_3}\rangle \quad (2.65) \\ &\quad \times |p'_{12}, p'_3, \alpha m_{J_3}\rangle \\ &= \sum_{\alpha, m_{J_3}} |p_{12}, p_3^n, \alpha m_{J_3}\rangle \\ &\quad \times (t_{12} \frac{1}{2} T_3, m_{t_1} + m_{t_2} M_{T_3} - m_{t_1} - m_{t_2} M_{T_3})(\frac{1}{2} \frac{1}{2} t_{12}, m_{t_1} m_{t_2} m_{t_1} + m_{t_2}) \\ &\quad \times \sum_{m_{l_3}} (j_{12} I_3 J_3, m_{J_3} - m_{l_3} - m_3 m_{l_3} + m_3 m_{J_3}) \\ &\quad \times (l_{12} s_{12} j_{12}, m_{J_3} - m_{l_3} - m_1 - m_2 - m_3 m_1 + m_2 m_{J_3} - m_{l_3} - m_3) \\ &\quad \times (l_3 \frac{1}{2} I_3, m_{l_3} m_3 m_{l_3} + m_3)(\frac{1}{2} \frac{1}{2} s_{12}, m_1 m_2 m_1 + m_2) \\ &\quad \times Y_{l_{12}, m_{J_3} - m_{l_3} - m_1 - m_2 - m_3}(\hat{p}_{12}) Y_{l_3, m_{l_3}}(\hat{p}_3). \end{aligned}$$

Note that all the quantum numbers in the  $\alpha$ 's of the  $d+n$  wave function are fixed except for the angular momentum  $l_{12}$ . In order to simplify the spherical harmonics, we choose  $\hat{p}_3$  in the direction of the z-axis and  $\hat{p}_{12}$  to be in the  $x-z$  plane. In this case, the spherical harmonics  $Y_{l_3, m_3}(\theta, \phi)$  appearing in Eqs. (2.64) and (2.65), are simplified to  $\sqrt{\frac{2l_3+1}{4\pi}} \delta_{m_30}$ .

### 2.2.5 Matrix elements

We are now ready to write the decay rates in terms of the two-body transition amplitude. The four matrix elements appearing in the decay rate formulas (2.54) and (2.55)

are

$$M_1 \equiv \langle \Psi_{m_{j_{12}} m_3} | ((1 + P) V_{12}^w + V_{123}^{(3)} G_0) | \psi_{\Lambda H}^3 \rangle, \quad (2.66)$$

$$M_2 \equiv \langle \Psi_{m_{j_{12}} m_3} | (P V_{12}^w + V_{123}^{(3)} G_0) | U \rangle, \quad (2.67)$$

$$M_3 \equiv \langle \Psi_{m_1 m_2 m_3} | (1 + P) V_{12}^w | \psi_{\Lambda H}^3 \rangle, \quad (2.68)$$

$$M_4 \equiv \langle \Psi_{m_1 m_2 m_3} | (1 + P) | U \rangle. \quad (2.69)$$

Using the wave functions in the  $|p'_{12}, p'_3, \alpha m_{J_3}\rangle$  basis defined in Eqs. 2.64 and 2.65 the needed matrix elements are

$$M_1 \equiv \langle p'_{12}, p'_3, \alpha m_{J_3} | ((1 + P) V_{12}^w + V_{123}^{(3)} G_0) | \psi_{\Lambda H}^3 \rangle, \quad (2.70)$$

$$M_2 \equiv \langle p'_{12}, p'_3, \alpha m_{J_3} | (P V_{12}^w + V_{123}^{(3)} G_0) | U \rangle, \quad (2.71)$$

$$M_3 \equiv \langle p'_{12}, p'_3, \alpha m_{J_3} | (1 + P) V_{12}^w | \psi_{\Lambda H}^3 \rangle, \quad (2.72)$$

$$M_4 \equiv \langle p'_{12}, p'_3, \alpha m_{J_3} | (1 + P) | U \rangle. \quad (2.73)$$

Using the definition of the hypertriton wave function of Eq. (2.61), the matrix element of Eq. (2.72) is

$$\begin{aligned} \langle p_{12} p_3 \alpha | (1 + P) V_{12}^w | \psi_{\Lambda H}^3 \rangle = & \langle p_{12} p_3, \alpha | \int dr'_{12} r'^2_{12} dr'_3 r'^2_3 \sum_{\alpha''} (1 + P) | \alpha'', r'_{12} r'_3 \rangle \\ & \times \int dr_{12} r^2_{12} \sum_{\alpha'} \langle \alpha', r_{12} r'_3 | \phi_{\Lambda H}^3 \rangle \sum_{m'_{t_{12}}} (t'_{12} \frac{1}{2} T', m'_{t_{12}} M'_t - m'_{t_{12}} M'_t) \\ & \times (t''_{12} \frac{1}{2} T'', m'_{t_{12}} - M'_t + M''_t M'_t - m'_{t_{12}} M''_t) \\ & \times \delta_{J' J''} \delta_{M' M''} \delta_{m'_{j_{12}} m'_{j''_{12}}} \delta_{l_3 l'_3} \delta_{s_3 s'_3} \delta_{I_3 I'_3} \\ & \times \int d\hat{r}_{12} \int dr'_{12} \langle (l''_{12} s''_{12}) j''_{12} m_{j''_{12}} | \hat{r}'_{12} \rangle \langle t''_{12} m_{t''_{12}} | V(\vec{q}) | t'_{12} m'_{t_{12}} \rangle \\ & \times \langle \hat{r}_{12} | (l'_{12} s'_{12}) j'_{12} m'_{j_{12}} \rangle, \end{aligned} \quad (2.74)$$

where  $\vec{q} \equiv \vec{r}'_{12} - \vec{r}_{12}$ . Once the plane-wave part, Eq. (2.74), is calculated, we insert it in Eq. (2.58) to calculate the rescattering part.

Finally we indicate a few more technicalities. First, in order to not double count final states when calculating the total decay rate for the 3N break-up,  $\Gamma_{3N}$ , we must add a global factor of  $\frac{1}{6}$  in front of the sum and integration over final quantum numbers and momenta. Second, due to the normalization of  $\langle \vec{p} | \vec{p}' \rangle = \delta^3(\vec{p} - \vec{p}')$ , followed in the calculation of the hypertriton decay, the potentials must include a factor of  $\frac{1}{(2\pi)^3}$ .

In the next chapter we proceed to describe the potential  $V(\vec{q})$  mediating the weak transition. The matrix elements of the operators appearing in the weak potential enter the calculation in Eq. (2.18) for the light hypernuclear decay and in Eq. (2.74) for the hypertriton decay. These spin and isospin matrix elements, in position and momentum space, are shown in the Appendices A, B, and C.

# Chapter 3

## Effective field theory description for the $\Lambda N \rightarrow NN$ interaction

In the previous chapter we have presented the formalism to compute the observables of the non-mesonic hypernuclear decay. Schematically, this computation requires 1) a description of the initial hypernuclei, which we can model using a shell model or, for the lightest hypernuclei, by directly solving the Schrödinger equation using few-body techniques, 2) the corresponding description of the decay products of the weak hypernuclear reaction, and 3) a proper understanding of the weak potential driving the  $\Lambda N \rightarrow NN$  transition.

In this chapter we will concentrate on the latter. As mentioned in the introduction, this transition amplitude is responsible for a large fraction of the observed weak hypernuclear decay and as such has received much attention in the last decade [18, 56, 57, 73, 74]. The first attempts to describe the reaction mechanism [16, 17, 18] were motivated by the successful one-meson-exchange potentials, extensively employed for the description of the  $NN \rightarrow NN$  interaction at low energies. These models, with further refinements, had been used since the early work of H. Yukawa, who successfully explained the long-range character of the nucleon-nucleon interaction through the exchange of a new particle termed pion. During the nineties these models—Partovi-Lomon [75, 76], Stony Brook [77, 78], Paris [79, 80] and Bonn [81, 82]—incorporated all known low lying mesons and allowed one to achieve a very precise understanding of the nucleon-nucleon force. This description was from the start intended to describe the experimental data on low energy scattering from the properties of the mesons and baryons that were detected at the accelerators. It was from this point of view an effective description of the problem which avoided solving the involved microscopic theory governing the dynamics of quarks and gluons, quantum chromodynamics (QCD). The impossibility of describing low energy reactions from QCD was circumvented by designing effective field theories which captured the essential features of QCD, such as chiral symmetry.

Chiral effective field theory was founded in the late sixties, well before QCD was established, by the works of S. Weinberg [83] and C. G. Callan, S. Coleman, J. Wess and B. Zumino [84, 85]. These works described the interactions among nucleons and pions at tree level, through phenomenological Lagrangians which were realizations of the spontaneous breaking of chiral symmetry. A decade later, S. Weinberg showed how to include pion loop corrections to these tree level calculations [86][86]—and thus how to

systematically construct an effective field theory—. In the mid eighties J. Gasser and H. Leutwyler successfully applied this theory, up to one loop, to  $\pi\pi$  and  $\pi N$  scattering [87], while also extending the calculation to  $SU(3)_F$  [88]. However, the nucleon-nucleon force was still not solved. The main problem in describing the nuclear force with chiral EFT is that the mass of the nucleon does not vanish in the chiral limit ( $q \rightarrow 0, m_\pi \rightarrow 0$ ), and it destroys the well defined expansion of small external momenta and pion masses. E. Jenkins and A. Manohar solved this problem by treating the baryons as heavy static fields such that the momentum transferred by the pions is small as compared to the baryon masses [89]. In the early nineties S. Weinberg suggested that, in order to compute the nuclear amplitudes, one could use the chiral expansion to calculate the NN potential and then iterate it to all orders in the Schrödinger equation [43, 44]. After this pioneering work, C. Ordóñez, L. Ray and U. Van Kolck calculated the NN potential up to next-to-next-to-leading order (NNLO) using time-ordered perturbation theory [45]. Since then, a few groups have further developed chiral EFT in order to describe nuclear reactions in few-body systems. Nowadays, these theories have reached a very sophisticated status with many observables computed up to several orders in the chiral expansion.

The problem we have at hand, the description of the  $\Lambda N \rightarrow NN$  weak transition, shares several features with the paradigmatic case of the NN strong potential. Namely, in both interactions there is a certain separation of scales—the external momenta of the baryons are quite lower than the QCD energy scale—, the masses of the baryonic fields involved in both processes are of the order of 1 GeV, and the strong interactions are involved in both transitions. This motivated the authors of Ref. [57] to write down the lowest order description of the amplitude. Their model combined the long range one pion exchange and medium-long range one kaon exchange potentials but left the description of the shorter distances to an effective field theory. This lowest order allows to get a reasonable description of the available data. The scarcity of data for hypernuclear decay mentioned in Chapter 1 does not pose, as of today, a very stringent constraint on the effective field theory. This has not stopped us from further developing the theory as the power of effective field theories lies precisely in the fact that one can further improve the results, within a certain range, by computing higher orders. Thus, in this chapter we present the full next order prediction of the theory for the  $\Lambda N \rightarrow NN$  amplitude. This is of course much more involved as it requires the explicit evaluation of all the loop integrals, requiring technical analytic and numerical calculations partly borrowed from the  $NN \rightarrow NN$  case.

The chapter is organized in the following way. First we will write down all the Lagrangians involving the degrees of freedom relevant for our amplitude. Second we will describe an important piece, which is the power counting scheme used to organize the different contributions of the theory. Next we discuss the lowest order contributions, which were partially known before, and finally we describe the main new contribution which is the evaluation of all two pion exchange diagrams entering in the next-to-leading order description. The calculation of the latter requires many intermediate steps which are detailed in the Appendices as they should be helpful for future researchers in the field.

### 3.1 Interaction Lagrangians

The non-mesonic weak decay of the  $\Lambda$  involves both the strong and electroweak interactions. The  $\Lambda$  decay is mediated by the presence of a nucleon which, in the simplest meson-exchange picture, exchanges a meson, e.g.  $\pi$ ,  $K$ , with the  $\Lambda$ . Therefore, computing the transition requires the knowledge of the strong and weak Lagrangians involving all the hadrons participating in the process. Apart from the interacting  $\Lambda$  and nucleon, the relevant degrees of freedom mediating the interaction are the  $\pi$ , the  $K$  and the  $\Sigma$ . The  $\pi$  and the  $K$  are exchanged between the baryons, and the  $\Sigma$  enters in the loop diagrams as an intermediate propagating baryon. The minimum energies necessary to create these hadrons in a  $\Lambda N$  interaction,  $M_\Sigma - M_\Lambda \simeq 77$  MeV,  $m_\pi \simeq 138$  MeV and  $m_K \simeq 495$  MeV, are either smaller or similar than the momentum transferred to each of the final nucleons,  $q \sim 450$  MeV. This large scale comes from the mass difference between the initial and final baryons,  $M_\Lambda - M_N \simeq 177$  MeV. Assuming that each of the initial baryons, the  $\Lambda$  and  $N$ , have a momentum of  $\sim 0 - 200$  MeV—due to their own Fermi motion in the hypernucleus—, the final nucleons obtain a momentum of  $\sim 417 - 463$  MeV. In this section we describe the strong and weak Lagrangians for these degrees of freedom entering at LO and NLO in the  $\Lambda N \rightarrow NN$  transition.

In our approach, we try to describe the weak  $\Delta S = 1$  interaction within the effective field theory (EFT) framework, i.e., in an effective and systematic way, which respects the symmetries of the underlying theory, the standard model. As mentioned in the introduction, chiral symmetry has played a key role in describing the strong nucleon-nucleon force. In particular, chiral EFT's successfully describe nucleon-nucleon scattering S, P and D-wave phase shifts up to energies of the order of  $E_{lab} \sim 200$  MeV and the binding energies of light nuclei [90]. However, the situation in the weak sector is quite less favorable. The short lifetime of the  $\Lambda$  does not allow us to perform  $\Lambda N$  scattering experiments, and the available experimental data on weak  $\Lambda$ -hadron interactions mainly comes from the weak decay of the  $\Lambda$  in free space and in the medium. Moreover, there is a strong disagreement between the experiments and the chiral effective field theory for the hyperon decays. In the works of E. Jenkins [91] and R. Springer [92] the s-wave and p-wave amplitudes for the hyperon decays have been derived using strong and weak effective chiral Lagrangians. The parity-violating amplitudes are automatically described by the vertices appearing in the weak Lagrangian, while the parity-conserving ones are described through pole diagrams, which are formed by weak baryon-baryon and strong baryon-baryon-meson vertices. Thus, one can fit the two parameters,  $h_D$  and  $h_F$ , appearing in the weak chiral Lagrangian to the experimentally known hyperon decays. In that case, one finds that when s-wave amplitudes are correctly reproduced, p-wave amplitude predictions disagree with the experiment. In our description, we obviate this problem by using phenomenological Lagrangians for the vertices  $\Lambda N\pi$  and  $\Sigma N\pi$ . The vertices  $\Lambda N K$  and  $\Sigma N K$  are then related to the pionic ones using  $SU(3)_F$  symmetry. Unfortunately, the vertices  $\Lambda N\pi\pi$  and  $\Lambda N$ , which may play an important role in the NLO description of the  $\Lambda N \rightarrow NN$  interaction, are not experimentally determined and cannot be related to the previous ones by  $SU(3)_F$ , and for these we use the chiral ones. In the following we explicitly list and use the Lagrangians mentioned above.

The weak interactions between the  $\Sigma$ ,  $\Lambda$  and  $N$  baryons and the pseudoscalar  $\pi$  and

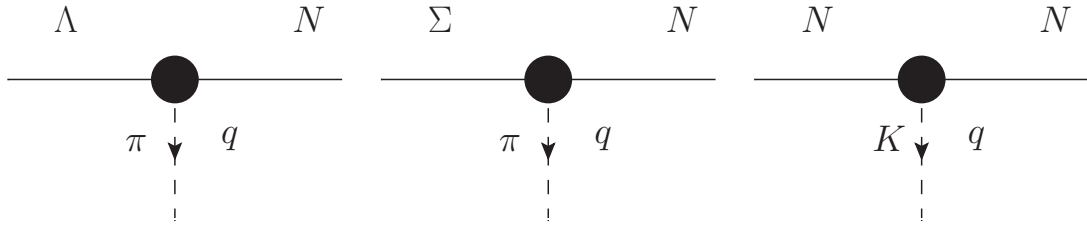


Figure 3.1: Weak vertices for the  $\Lambda N \pi$ ,  $\Sigma N \pi$  and  $NN K$  stemming from the Lagrangians in Eqs. (3.1) to (3.3). The weak vertex is represented by a solid black circle.

$K$  mesons that contribute to the interaction, depicted in Fig. 3.1, are described by the phenomenological Lagrangians

$$\mathcal{L}_{\Lambda N \pi}^w = -i G_F m_\pi^2 \bar{\Psi}_N (A + B \gamma^5) \vec{\tau} \cdot \vec{\pi} \Psi_\Lambda , \quad (3.1)$$

$$\mathcal{L}_{\Sigma N \pi}^w = -i G_F m_\pi^2 \bar{\Psi}_N (\vec{A}_{\Sigma_i} + \vec{B}_{\Sigma_i} \gamma^5) \cdot \vec{\pi} \Psi_{\Sigma_i} , \quad (3.2)$$

$$\begin{aligned} \mathcal{L}_{NNK}^w = & -i G_F m_\pi^2 [\bar{\psi}_N \begin{pmatrix} 0 \\ 1 \end{pmatrix} (C_K^{PV} + C_K^{PC} \gamma_5) (\phi^K)^\dagger \psi_N \\ & + \bar{\psi}_N \psi_N (D_K^{PV} + D_K^{PC} \gamma_5) (\phi^K)^\dagger \begin{pmatrix} 0 \\ 1 \end{pmatrix}] , \end{aligned} \quad (3.3)$$

where  $G_F m_\pi^2 = 2.21 \times 10^{-7}$  is the weak Fermi coupling constant,  $\gamma_5$  is the fifth gamma matrix and  $\tau$  the Pauli matrices. We have implemented the isospin rule of  $\Delta I = 1/2$ , described in Sec. 2.1.3. Within this rule, the  $\Lambda$  and the  $\Sigma$ , with isospins  $I = 0$  and  $I = 1$ , are coupled to and isospin of  $I = 1/2$ . Thus, the  $\Lambda$  behaves as a hyperon with  $I = 1/2$  and the  $\Sigma$  as a hyperon with  $I = 1/2$  or  $I = 3/2$ . The index  $i$  appearing in the  $\Sigma$  field refers to these two isospurion states:

$$\Psi_{\Sigma \frac{1}{2}} = \begin{pmatrix} -\sqrt{\frac{2}{3}} \Sigma_+ \\ \frac{1}{\sqrt{3}} \Sigma_0 \end{pmatrix}, \quad \Psi_{\Sigma \frac{3}{2}} = \begin{pmatrix} 0 \\ -\frac{1}{\sqrt{3}} \Sigma_+ \\ \sqrt{\frac{2}{3}} \Sigma_0 \\ \Sigma_- \end{pmatrix}. \quad (3.4)$$

The PV and PC structures,  $\vec{A}_{\Sigma_i}$  and  $\vec{B}_{\Sigma_i}$  contain the corresponding weak coupling constants together with the isospin operators  $\tau^a$  for  $\frac{1}{2} \rightarrow \frac{1}{2}$  transitions and  $T^a$  for  $\frac{3}{2} \rightarrow \frac{1}{2}$  transitions. The weak couplings  $A = 1.05$ ,  $B = -7.15$ ,  $A_{\Sigma \frac{1}{2}} = -0.59$ ,  $A_{\Sigma \frac{3}{2}} = 2.00$ ,  $B_{\Sigma \frac{1}{2}} = -15.68$ , and  $B_{\Sigma \frac{3}{2}} = -0.26$  are fixed to reproduce the experimental data of the corresponding hyperon decays [93], while the ones involving kaons,  $C_K^{PC} = -18.9$ ,  $D_K^{PC} = 6.63$ ,  $C_K^{PV} = 0.76$  and  $D_K^{PV} = 2.09$ , are derived using  $SU(3)_F$  symmetry.

The other two weak vertices (Fig. 3.2), entering at NLO, are obtained from the weak  $SU(3)_F$  chiral Lagrangian,

$$\mathcal{L}_{\Lambda N \pi \pi}^w = G_F m_\pi^2 \frac{h_{2\pi}}{f_\pi^2} (\vec{\pi} \cdot \vec{\pi}) \bar{\Psi} \Psi_\Lambda , \quad (3.5)$$

$$\mathcal{L}_{\Lambda N}^w = G_F m_\pi^2 h_{\Lambda N} \bar{\Psi} \Psi_\Lambda , \quad (3.6)$$

with  $h_{2\pi} = (h_D + 3h_F)/(8\sqrt{6}G_F m_\pi^2) = 10.13$  MeV and  $h_{\Lambda N} = -(h_D + 3h_F)/(\sqrt{6}G_F m_\pi^2) = -81.02$  MeV and  $f_\pi = 92.4$  MeV. For the parameters appearing in the weak chiral La-

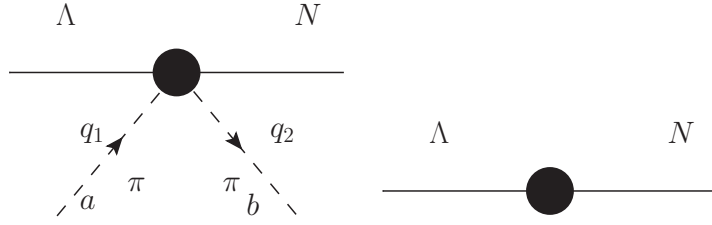


Figure 3.2: Weak vertices corresponding to the  $\Lambda N\pi\pi$  and  $\Lambda N$  interactions, represented by a solid black circle. The corresponding Lagrangians are given in Eqs. (3.5) and (3.6).

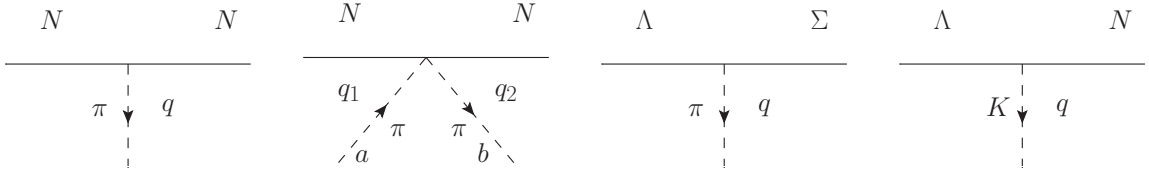


Figure 3.3: Strong vertices for the  $NN\pi$ ,  $NN\pi\pi$ ,  $\Lambda\Sigma\pi$  and  $\Lambda NK$  which arise from the Lagrangians in Eqs. (3.7) to (3.10).

grangian,  $h_D$  and  $h_F$ , we have taken the values  $h_D = -7.14 \cdot 10^{-6}$  MeV and  $h_F = 1.70 \cdot 10^{-5}$  MeV, obtained from a fit to the s-wave amplitudes of the hyperon decays [93].

The strong vertices for the interaction between our baryonic and mesonic degrees of freedom are obtained from the strong  $SU(3)_F$  chiral Lagrangian [93],

$$\mathcal{L}_{NN\pi}^s = -\frac{g_A}{2f_\pi}\bar{\Psi}\gamma^\mu\gamma_5\vec{\tau}\Psi \cdot \partial_\mu\vec{\pi}, \quad (3.7)$$

$$\mathcal{L}_{NN\pi\pi}^s = -\frac{1}{4f_\pi^2}\bar{\Psi}\gamma^\mu\vec{\tau} \cdot (\vec{\pi} \times \partial_\mu\vec{\pi})\Psi, \quad (3.8)$$

$$\mathcal{L}_{\Lambda\Sigma\pi}^s = -\frac{D}{\sqrt{3}}\bar{\Psi}_\Lambda\gamma^\mu\gamma_5\vec{\Psi}_\Sigma \cdot \partial_\mu\vec{\pi}, \quad (3.9)$$

$$\mathcal{L}_{\Lambda NK}^s = \frac{D+3F}{2\sqrt{3}f_\pi}\bar{\Psi}_N\gamma^\mu\gamma_5\partial_\mu\phi_K\Psi_\Lambda, \quad (3.10)$$

where we have taken the convention which gives us  $\vec{\Psi}_\Sigma \cdot \vec{\pi} = \Psi_{\Sigma_+}\pi_- + \Psi_{\Sigma_-}\pi_+ + \Psi_{\Sigma_0}\pi_0$ , and we consider,  $g_A = 1.290$  and  $f_\pi = 92.4$  MeV.  $D = 0.822$  and  $F = 0.468$  parameterize the strong  $SU(3)_F$  chiral Lagrangian. These strong coupling constants are taken from  $NN$  interaction models such as the ones derived by the Jülich [69] or Nijmegen [94, 95] groups. The four interaction vertices corresponding to these Lagrangians are depicted in Fig. 3.3. The kaon field appearing Eq. 3.10 is defined as  $\phi_K = \begin{pmatrix} K^+ \\ K^0 \end{pmatrix}$ .

Once the interaction Lagrangians involving the relevant degrees of freedom have been presented, we need to define the power counting scheme which allows us to organize the different contributions to the full amplitude.

## 3.2 Power counting scheme and non-relativistic expansion

The amplitude for the  $\Lambda N \rightarrow NN$  transition is built as the sum of medium and long-range one meson exchanges (i.e.  $\pi$  and  $K$ ), the contribution from the two-pion exchanges, and the contribution of the contact interactions up to two powers of momentum. The order at which the different terms enter in the perturbative expansion of the amplitudes is given by the so-called Weinberg power counting scheme [43, 44]. Within this scheme, the Feynman diagrams are organized in increasing powers of momenta. From dimensional analysis one can easily see that the baryonic propagators are  $\mathcal{O}(q^{-1})$ , the mesonic ones  $\mathcal{O}(q^{-2})$ , the derivative interactions  $\mathcal{O}(q^1)$  and the four-momentum integrations  $\mathcal{O}(q^4)$ . Applying then some topological identities one has that, the connected and irreducible diagrams, and with four external baryons, contribute with  $\nu$  powers of momenta,

$$\nu = 2L + \sum_i (d_i + \frac{n_i}{2} - 2), \quad (3.11)$$

where  $\nu$  is given by the number of loops ( $L$ ), the number of derivative insertions in each vertex  $i$  ( $d_i$ ), and the number of baryon fields in the vertex ( $n_i$ ).

In our calculations we will employ the heavy baryon formalism developed by E. Jenkins and A. Manohar in the early nineties [89]. This technique introduces a perturbative expansion in the baryon masses appearing in the Lagrangians, so that this new large scale does not disrupt the Weinberg power counting. It is worth noting that, in the heavy baryon formalism, terms of the type  $\bar{\Psi}_B \gamma^5 \Psi_B$  are subleading in front of terms like  $\bar{\Psi}_B \Psi_B$ , since they show up at one order higher in the heavy baryon expansion. In our calculation, we choose to keep both terms in our Lagrangians of Eqs. (3.1) and (3.2) because the experimental values of the couplings  $B$  and  $B_\Sigma$  are much larger than  $A$  and  $A_\Sigma$ . For example,  $A = 1.05$  and  $B = -7.15$  [93].

Our calculation is characterized by the presence of different octet baryons in the relevant Feynman diagrams, contributing in both, the spinors and propagators. In the center of mass system, the spinors for the incoming  $\Lambda$  and  $N$  with masses  $M_\Lambda$  and  $M_N$ , energies  $E_p^\Lambda$  and  $E_p^N$ , and momenta  $\vec{p}$  and  $-\vec{p}$  are given by

$$u_1(E_p^\Lambda, \vec{p}) = \sqrt{\frac{E_p^\Lambda + M_\Lambda}{2M_\Lambda}} \begin{pmatrix} 1 \\ \vec{\sigma}_1 \cdot \vec{p} \\ E_p^\Lambda + M_\Lambda \end{pmatrix}, \quad (3.12)$$

$$u_2(E_p^N, -\vec{p}) = \sqrt{\frac{E_p^N + M_N}{2M_N}} \begin{pmatrix} 1 \\ -\vec{\sigma}_2 \cdot \vec{p} \\ E_p^N + M_N \end{pmatrix}, \quad (3.13)$$

and for the outgoing nucleons with momenta  $\vec{p}'$  and  $-\vec{p}'$ , and energy  $E' \equiv \frac{1}{2} (E_p^\Lambda + E_p^N)$ ,

$$\bar{u}_1(E', \vec{p}') = \sqrt{\frac{E' + M_N}{2M_N}} \left( \begin{array}{cc} 1 & -\frac{\vec{\sigma}_1 \cdot \vec{p}'}{E' + M_N} \end{array} \right), \quad (3.14)$$

$$\bar{u}_2(E', -\vec{p}') = \sqrt{\frac{E' + M_N}{2M_N}} \left( \begin{array}{cc} 1 & \frac{\vec{\sigma}_2 \cdot \vec{p}'}{E' + M_N} \end{array} \right). \quad (3.15)$$

The momenta and the Pauli matrices are labeled according to Fig. 3.4. The relativistic propagator of a baryon with mass  $M_B$  and momentum  $p$  reads

$$\frac{i}{p - M_B + i\epsilon} = \frac{i(\not{p} + M_B)}{\not{p}^2 - M_B^2 + i\epsilon}. \quad (3.16)$$

Heavy-baryon expanding with these spinors and propagators introduces mass differences ( $M_\Lambda - M_N$ ,  $M_\Sigma - M_\Lambda$ ) in the baryonic propagators. A reasonable approach would be to consider these mass differences of order  $\mathcal{O}(\vec{q}^2/\Lambda^2)$ ,  $M_B = \bar{M} + \mathcal{O}(\vec{q}^2/\Lambda^2)$ , and thus they would not enter in the loop diagrams. We have chosen to leave the physical masses in both the initial and final spinors and also in the intermediate propagators; i.e. we consider the mass differences as another scale in the heavy baryon expansion. The corresponding  $SU(3)_F$  symmetric limit is also given, and can be easily obtained from our expressions by setting the mass differences, which we explicitly retain, to zero.

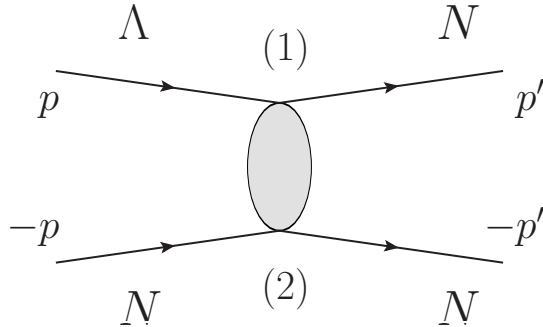


Figure 3.4: General diagram representing the  $\Lambda N \rightarrow NN$  transition in the center of mass frame. The solid ellipse represents any interaction connecting the four baryons. The upper vertex is labeled with (1) and the lower one with (2). The initial and final momenta in the upper legs are denoted with  $p$  and  $p'$ , and the corresponding ones in the lower legs,  $-p$  and  $-p'$ . In all the following diagrams we use these labels.

The procedure we follow to compute the different Feynman diagrams entering the transition amplitude is the following: first we write down the relativistic expressions for each diagram, and afterwards, we perform the heavy baryon expansion. Starting our calculation from the relativistic amplitudes, instead of directly using the heavy-baryon Feynman rules, allows us to keep track on how the mass differences mentioned above affect the final amplitude.

In the next sections we will describe the LO and NLO contributions to the process  $\Lambda N \rightarrow NN$ , following the scheme presented here. The explicit expressions and details of the calculations are given in the App. D and E.

### 3.3 Leading order Contributions

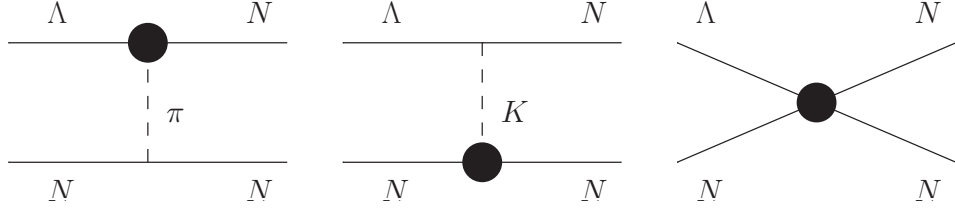


Figure 3.5: One-pion and one-kaon exchange, and four-point baryon contributions to the transition.

At tree level, the transition potential  $\Lambda N \rightarrow NN$  involves the LO contact terms, and  $\pi$  and  $K$  exchanges, as depicted in Fig. 3.5. First, the contact interaction can be written as the most general Lorentz invariant potential with no derivatives. Taking into account the antisymmetry of the final two nucleons, the four-fermion (4P) interaction in momentum space at leading order (in units of  $G_F$ ) is

$$V_{4P}(\vec{q}) = C_{00} + C_{01} \vec{\sigma}_1 \vec{\sigma}_2, \quad (3.17)$$

where  $C_{00}$  and  $C_{01}$  are low energy constants which need to be fitted by direct comparison to experimental data.

The potentials for the one pion and one kaon exchanges read, respectively,

$$V_\pi(\vec{q}) = -\frac{G_F m_\pi^2 g_{NN\pi}}{2M_N} \left( A - \frac{B}{2\bar{M}} \vec{\sigma}_1 \vec{q} \right) \frac{\vec{\sigma}_2 \vec{q}}{-q_0^2 + \vec{q}^2 + m_\pi^2} \vec{\tau}_1 \cdot \vec{\tau}_2, \quad (3.18)$$

$$V_K(\vec{q}) = \frac{G_F m_\pi^2 g_{\Lambda NK}}{2\bar{M}} \left( \hat{A} + \frac{\hat{B}}{2M_N} \vec{\sigma}_2 \vec{q} \right) \frac{\vec{\sigma}_1 \vec{q}}{-q_0^2 + \vec{q}^2 + m_K^2}, \quad (3.19)$$

where  $m_\pi = 138.04$  MeV and  $m_K = 494.99$  MeV,  $q_0 \equiv \frac{1}{2}(M_\Lambda - M_N)$ ,  $\bar{M} \equiv \frac{1}{2}(M_N + M_\Lambda)$ ,  $M_\Lambda = 1115.68$  MeV,  $M_N = 938.92$  MeV,  $g_{NN\pi} \equiv \frac{g_A M_N}{f_\pi}$ ,  $g_{\Lambda NK} \equiv -\frac{D+3F}{2\sqrt{3}f_\pi}$ ,  $A = 1.05$ ,  $B = -7.15$  and

$$\begin{aligned} \hat{A} &= \left( \frac{C_K^{PV}}{2} + D_K^{PV} + \frac{C_K^{PV}}{2} \vec{\tau}_1 \vec{\tau}_2 \right), \\ \hat{B} &= \left( \frac{C_K^{PC}}{2} + D_K^{PC} + \frac{C_K^{PC}}{2} \vec{\tau}_1 \vec{\tau}_2 \right). \end{aligned}$$

The values for the weak PV and PC coupling constants, derived using the NSC97f model, are  $C_K^{PV} = 0.76$ ,  $D_K^{PV} = 2.12$ ,  $C_K^{PC} = -23.75$  and  $D_K^{PC} = 8.33$ . The constants are labeled  $D$  and  $C$  depending if they contribute to the direct or exchange Feynman diagrams. The transferred momentum  $\vec{q} \equiv \vec{p}' - \vec{p}$ , and the spin and isospin operational structures connecting the initial and final states, are defined according to the labels of Fig. 3.4. Since in the hypertriton calculation we use Jacobi coordinates, we should also use them for the transferred momentum. Denoting the Jacobi coordinates for the initial and final states

as  $\vec{p}_{12}$ ,  $\vec{p}_3$ ,  $\vec{p}_{CM}$  and  $\vec{p}_{12}'$ ,  $\vec{p}_3'$ ,  $\vec{p}_{CM}'$ , we have, in the center of mass frame,  $\vec{p}_{CM} = 0$ , and using the spectator condition,  $\vec{p}_3 = \vec{p}_3'$ :

$$\vec{q} \equiv \vec{p}' - \vec{p} = \vec{p}_{12}' - \vec{p}_{12} + \frac{M_\Lambda - M_N}{2(M_\Lambda + M_N)} \vec{p}_3. \quad (3.20)$$

In the computation of the hypernuclear decay observables, we make the approximation  $\vec{q} \simeq \vec{p}_{12}' - \vec{p}_{12}$ .

We note here that the global sign of the one-meson-exchange (OME) potentials, which depends on the sign of the weak hyperon-nucleon-meson vertices, is currently not determined. The experiments constraining these weak vertices are the mesonic weak decays of hyperons, which don't affect the global sign of the vertex, and the non-mesonic weak decays of hypernuclei, which are not precise enough to determine it. Therefore, the global sign of the weak OME potentials driving the  $\Lambda N \rightarrow NN$  is a matter of the convention one uses for the sign of the hyperon-nucleon-meson vertices.

### 3.3.1 LO order contributions to the $\Sigma N \rightarrow NN$ potential

So far we have discussed the formalism for the weak decay of a  $\Lambda$  bounded in hypernuclei. However, the strong interactions among the  $\Lambda$  and the medium of nucleons may convert it to a virtual  $\Sigma$  (and then back to a  $\Lambda$ ). These strong interactions happen many orders of magnitude faster than the weak interactions that make the  $\Lambda$  decay, and therefore the initial hypernuclear wave function must take into account the  $\Sigma$  hyperon as an explicit degree of freedom. This effect has been considered in the LO study of the non-mesonic decay of the hypertriton. Therefore, the weak potential mediating the decay of the hypertriton must also include the  $\Sigma N \rightarrow NN$  transition.

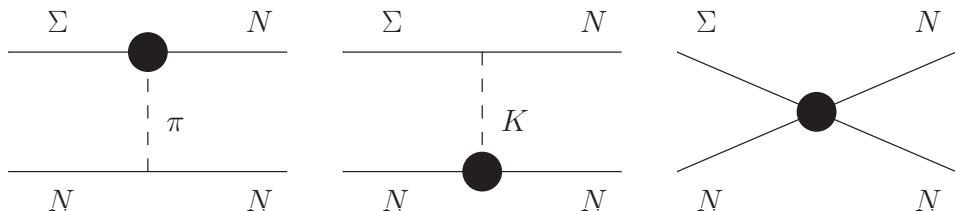


Figure 3.6: One-pion and one-kaon exchange and contact contributions to the transition.

The OPE and OKE mechanisms and the contact interaction driving the  $\Sigma N \rightarrow NN$  interaction are depicted in Fig.3.6. All the vertices involved in this interaction have already been described in Sec. 3.1, except the strong  $\Sigma NK$  one. As the  $\Lambda NK$  vertex, this one is also extracted from the strong chiral  $SU(3)_F$  Lagrangian,

$$\mathcal{L}_{\Sigma NK}^s = \frac{-D + F}{2f_\pi} \bar{\Psi}_N \gamma^\mu \gamma_5 \vec{\tau}^\dagger \cdot \vec{\Psi}_\Sigma \partial_\mu \phi_K, \quad (3.21)$$

where the couplings are defined as before and we use the convention

$$\vec{\tau}^\dagger \cdot \vec{\Psi}_\Sigma = \begin{pmatrix} \Sigma_0 & \sqrt{2}\Sigma_+ \\ \sqrt{2}\Sigma_- & -\Sigma_0 \end{pmatrix}. \quad (3.22)$$

The contact potential is analogous to the one for the  $\Lambda N \rightarrow NN$  transition, with two new independent low energy constants. Thus, the potentials read:

$$V_\pi^{(\Sigma)}(\vec{q}) = -\frac{G_F m_\pi^2 g_{NN\pi}}{2M_N} \left[ \left( A_{\Sigma \frac{1}{2}} \vec{\sigma}_2 \cdot \hat{q} - \frac{B_{\Sigma \frac{1}{2}}}{2M_\Sigma} \vec{q}^2 (\vec{\sigma}_1 \cdot \hat{q})(\vec{\sigma}_2 \cdot \hat{q}) \right) \vec{\tau}_1 \cdot \vec{\tau}_2 + \left( A_{\Sigma \frac{3}{2}} \vec{\sigma}_2 \cdot \hat{q} - \frac{B_{\Sigma \frac{3}{2}}}{2M_\Sigma} \vec{q}^2 (\vec{\sigma}_1 \cdot \hat{q})(\vec{\sigma}_2 \cdot \hat{q}) \right) \vec{T}_1 \cdot \vec{\tau}_2 \right] \frac{1}{-q_0'^2 + \vec{q}^2 + m_\pi^2}, \quad (3.23)$$

$$V_K^{(\Sigma)}(\vec{q}) = \frac{G_F m_\pi^2 g_{\Sigma NK}}{2M_\Sigma} \left( \hat{A}_\Sigma |\vec{q}| \vec{\sigma}_1 \cdot \hat{q} + \frac{\hat{B}_\Sigma}{2M_N} \vec{q}^2 (\vec{\sigma}_1 \cdot \hat{q})(\vec{\sigma}_2 \cdot \hat{q}) \right) \frac{1}{-q_0'^2 + \vec{q}^2 + m_K^2}, \quad (3.24)$$

$$V_{4P}^{(\Sigma)}(\vec{q}) = C_{00}^\Sigma + C_{01}^\Sigma \vec{\sigma}_1 \vec{\sigma}_2, \quad (3.25)$$

where  $A_{\Sigma \frac{1}{2}} = -0.59$ ,  $A_{\Sigma \frac{3}{2}} = 2.00$ ,  $B_{\Sigma \frac{1}{2}} = -15.68$ ,  $B_{\Sigma \frac{3}{2}} = -0.26$ ,  $g_{\Sigma NK} = 5.38$ ,  $M_\Sigma \equiv \frac{M_N + M_\Sigma}{2}$ ,  $M_\Sigma = 1193.15$  MeV,  $q'_0 \equiv \frac{1}{2}(M_\Sigma - M_N)$ , and

$$\begin{aligned} \hat{A}_\Sigma &= -\sqrt{3} \left( \frac{C_K^{PV}}{2} + D_K^{PV} \right) + \frac{1}{2\sqrt{3}} C_K^{PV} \vec{\tau}_1 \vec{\tau}_2 + C_K^{PV} \vec{T}_1 \cdot \vec{\tau}_2 \\ \hat{B}_\Sigma &= -\sqrt{3} \left( \frac{C_K^{PC}}{2} + D_K^{PC} \right) + \frac{1}{2\sqrt{3}} C_K^{PC} \vec{\tau}_1 \vec{\tau}_2 + C_K^{PC} \vec{T}_1 \cdot \vec{\tau}_2 \end{aligned}$$

The transferred momenta and the operational structures are defined as in the previous section. The matrix elements for the different spin and isospin structures that appear in both transitions,  $\Lambda N \rightarrow NN$  and  $\Sigma N \rightarrow NN$ , are shown in the App. B and C.

## 3.4 Next-to-leading order contributions

The NLO contribution to the weak decay process,  $\Lambda N \rightarrow NN$ , includes contact interactions with one and two derivative operators, caramel diagrams and two-pion-exchange diagrams, as shown in the following sections.

### 3.4.1 NLO contact potential

Order	Parity	Structures
1	PV	$\vec{\sigma}_1 \cdot \vec{q}, \vec{\sigma}_1 \cdot \vec{p}, \vec{\sigma}_2 \cdot \vec{q},$ $\vec{\sigma}_2 \cdot \vec{p}, (\vec{\sigma}_1 \times \vec{\sigma}_2) \cdot \vec{q}, (\vec{\sigma}_1 \times \vec{\sigma}_2) \cdot \vec{p},$
2	PC	$\vec{q}^2, \vec{p}^2, (\vec{\sigma}_1 \cdot \vec{\sigma}_2) \vec{q}^2, (\vec{\sigma}_1 \cdot \vec{\sigma}_2) \vec{p}^2, (\vec{\sigma}_1 \cdot \vec{q})(\vec{\sigma}_2 \cdot \vec{q}),$ $(\vec{\sigma}_1 \cdot \vec{p})(\vec{\sigma}_2 \cdot \vec{p}), (\vec{\sigma}_1 + \vec{\sigma}_2) \cdot (\vec{q} \times \vec{p})$

Table 3.1: All possible PC and PV NLO operational structures connecting the initial and final spin and angular momentum states. There are a total of thirteen.

In principle the NLO contact potential should include, in the center of mass frame, structures involving both the initial ( $\vec{p}$ ) and final ( $\vec{p}'$ ) momenta, or independent linear

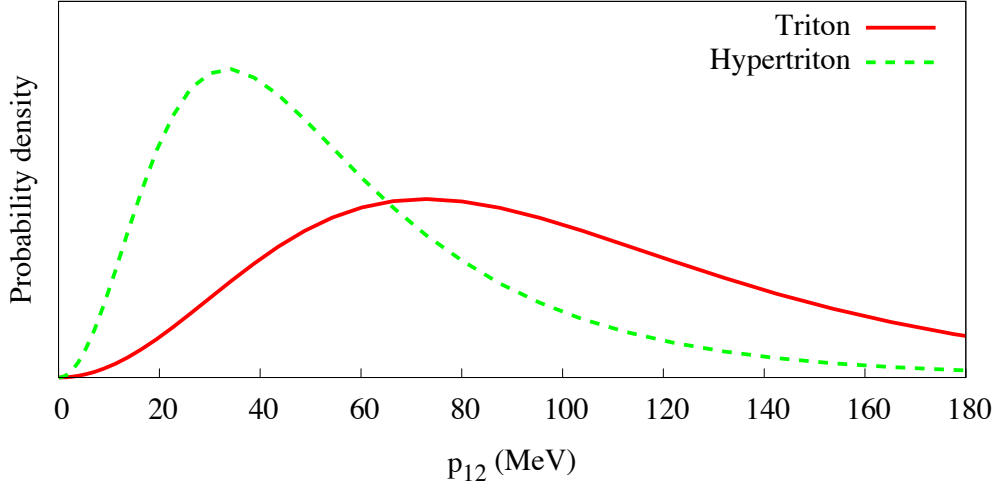


Figure 3.7: Probability densities for the relative momentum between two nucleons in the triton (solid red) and between a  $\Lambda$  and a nucleon in the hypertriton (dashed green). The wave functions are calculated using strong effective potentials such that the corresponding binding energies are reproduced [96]. Due to the  $\Lambda$  being less bound than the nucleons, the momentum in the hypertriton is peaked at lower values.

combinations of these two momenta, e.g.  $\vec{q} \equiv \vec{p}' - \vec{p}$  and  $\vec{p}$ . Table 3.1 lists all these possible structures. At NLO there are 13 LEC's—6 PV ones at order  $\mathcal{O}(q/M)$  and 7 PC ones at order  $\mathcal{O}(q^2/M^2)$ —, which must be fitted to experiment. This is not feasible with current experimental data on hypernuclear decay. A reasonable way to reduce the number of LEC's and render the fitting procedure more tractable is to note that the pionless weak decay mechanism we are interested in takes place inside a  $\Lambda$ -hypernucleus. Therefore, one can assume that in the  $\Lambda N \rightarrow NN$  transition potential the initial baryons have a fairly small momentum. For example, for the hypertriton, the typical relative momentum between the  $\Lambda$  and a nucleon is of the order of a few tens of MeV. In comparison, the relative momentum between two nucleons in its nuclear partner, the triton, is peaked at quite larger values, as shown in Fig. 3.7. Moreover, the final nucleons gain an extra momentum from the surplus mass of the  $\Lambda$  ( $M_\Lambda - M_N \simeq 116$  MeV), which in most cases allows to consider,  $|\vec{p}'| \gg |\vec{p}|$ . In this case, one may approximate  $\vec{q} \simeq \vec{p}'$  and  $\vec{p} = 0$ . Within this approximation, the contact potential up to  $\mathcal{O}(\vec{q}^2)$  contains only eight LEC's and reads (in units of  $G_F$ ):

$$\begin{aligned}
V_{4P}(\vec{q}) &= C_{00} + C_{01}(\vec{\sigma}_1 \cdot \vec{\sigma}_2) \\
&\quad + C_{10} \frac{\vec{\sigma}_1 \vec{q}}{2M_N} + C_{11} \frac{\vec{\sigma}_2 \vec{q}}{2M_N} + iC_{12} \frac{(\vec{\sigma}_1 \times \vec{\sigma}_2) \vec{q}}{2M_N} \\
&\quad + C_{20} \frac{\vec{\sigma}_1 \vec{q} \vec{\sigma}_2 \vec{q}}{4M_N^2} + C_{21} \frac{\vec{\sigma}_1 \vec{\sigma}_2 \vec{q}^2}{4M_N^2} + C_{22} \frac{\vec{q}^2}{4M_N^2}.
\end{aligned} \tag{3.26}$$

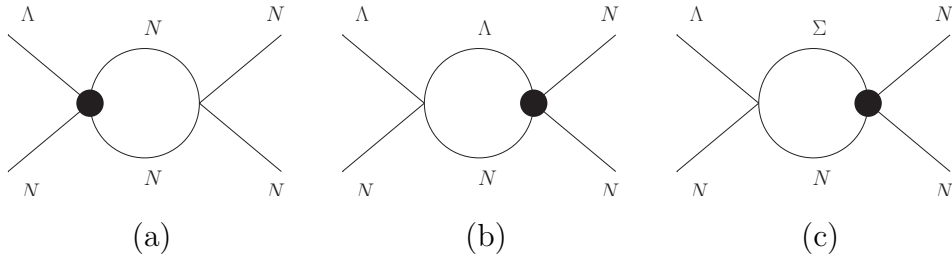


Figure 3.8: Caramel diagrams contributing to the process at NLO. The solid circle represents the weak vertex.

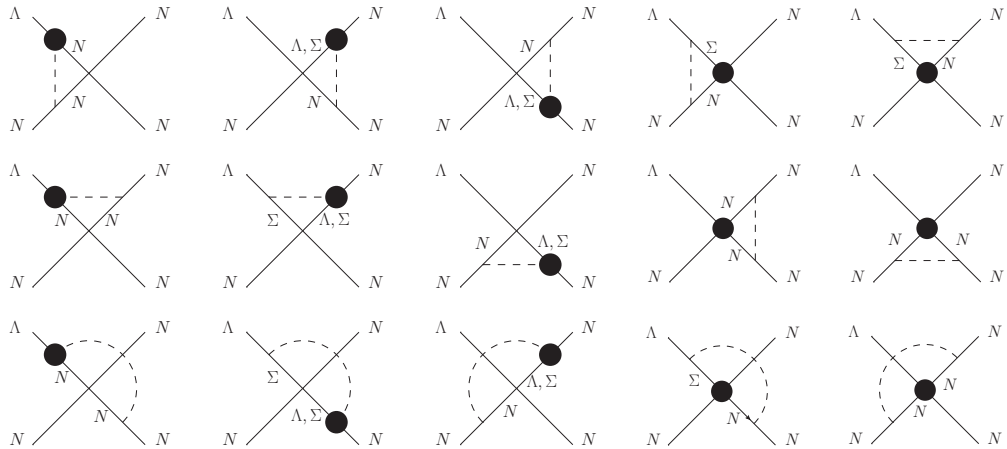


Figure 3.9: Corrections to the LO contact interactions. The contributions of all these diagrams can be accounted for by an adequate shift of the coefficients of the LO contact terms.

Using strong and weak LO contact interactions and two baryonic propagators one can also build three diagrams that enter at NLO. These caramel-like diagrams are shown in Fig. 3.8. They only differ in the position of the strong and weak vertices and in the mass of the upper-leg baryonic propagator. In order to write a general expression for the three caramel diagrams we label the mass of the upper-leg propagating baryon  $M_\alpha$  ( $M_a = M_N$ ,  $M_b = M_\Lambda$  and  $M_c = M_\Sigma$ ) and the corresponding strong and weak contact vertices  $C_{00(s)}^\alpha + C_{01(s)}^\alpha \vec{\sigma}_1 \cdot \vec{\sigma}_2$  and  $C_{00(w)}^\alpha + C_{01(w)}^\alpha \vec{\sigma}_1 \cdot \vec{\sigma}_2$ , where  $\alpha = a, b, c$  correspond to the labels of Fig. 3.8. It is also convenient to define  $M_\alpha = M_N + \Delta_\alpha$ . In the heavy baryon formalism these diagrams only contribute with an imaginary part of the form

$$V_\alpha = i \frac{G_F m_\pi^2}{16\pi M_N} (C_{00(s)}^\alpha + C_{01(s)}^\alpha \vec{\sigma}_1 \cdot \vec{\sigma}_2) (C_{00(w)}^\alpha + C_{01(w)}^\alpha \vec{\sigma}_1 \cdot \vec{\sigma}_2) \times \sqrt{(\Delta_b - \Delta_\alpha)(\frac{1}{2}(\Delta_b + \Delta_\alpha) + M_N) + \vec{p}^2}. \quad (3.27)$$

The only dependence on momenta is due to the  $\vec{p}^2$  inside the square root, which should be neglected in the approximations  $|\vec{p}'| \gg |\vec{p}|$ . Few more details of this calculation are given in App. D.1.

One pion corrections to the LO contact interactions, shown in Fig. 3.9, also enter at

NLO. However, the net contribution of these diagrams is to shift the coefficients of the LO contact terms with functions which depend on  $m_\pi$ ,  $M_\Lambda - M_N$  and  $M_\Sigma - M_N$ , and therefore we do not include them.

### 3.4.2 Two-pion-exchange diagrams

The two-pion-exchange contributions are organized according to the different topologies—balls, triangles, and boxes—, such that most of the integration techniques are shared by each class of diagrams. There are two types of ball diagrams, among which only one gives a non-zero contribution, depicted in Fig. 3.10. In addition, there are four triangle diagrams, shown in Fig. 3.11, and two box and two crossed box diagrams, shown in Fig. 3.12. The topologies contain, respectively, zero, one, and two baryonic propagators, which may correspond to  $N$  or  $\Sigma$  baryons. All the diagrams contain two relativistic propagators corresponding to the  $2-\pi$  exchange.

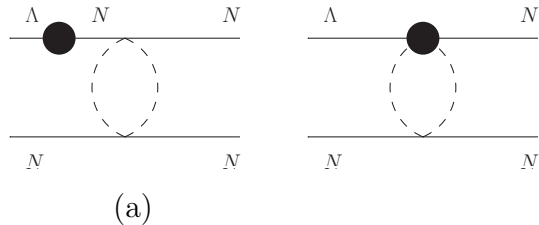


Figure 3.10: Possible ball diagrams contributing to the process at NLO. The right one gives a zero contribution due to isospin cancellations. The solid circle represents the weak vertex.

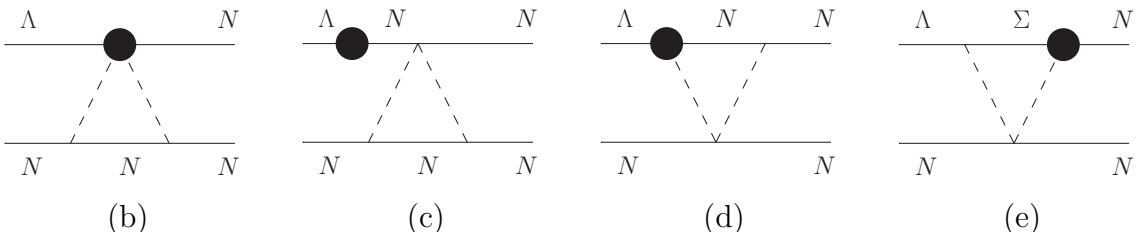


Figure 3.11: Triangle diagrams which contribute to the process at NLO. The solid circle represents the weak interaction vertex.

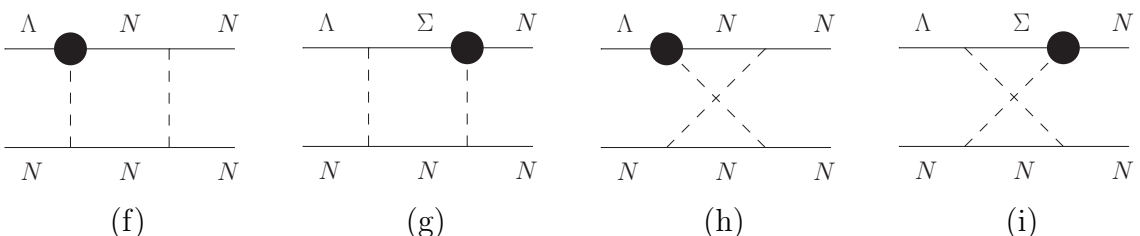


Figure 3.12: Box diagrams which contribute to the process at NLO. The solid circle stands for the weak interaction vertex.

The technical details of the evaluation of the Feynman diagrams for the ball, triangle and box diagrams are given in App. D.2, D.3, and D.4, respectively. The main technique used is to introduce a number of master integrals (the simplest ones), which appear in different diagrams, and which reduce the mathematical complexity of the problem (see App. E). Once they are defined, we derive a number of relations between the master integrals and the more complicated ones, which can in most cases be easily checked. Full details are provided to ensure the future use of these expressions. In the next section we provide a few more details on how this calculation technique is applied.

Using the labels defined in Figs. 3.10, 3.11 and 3.12 we organize the contributions of all the  $2 - \pi$  exchange diagrams in Eqs. (3.28) to (3.36). The corresponding coefficients in terms of the coupling constants, baryon and meson masses, and momenta can be read off from the full expressions given in the App. D.2, D.3 and D.4.

$$V_a = c_{a1} \vec{\tau}_1 \cdot \vec{\tau}_2, \quad (3.28)$$

$$V_b = c_{b1}, \quad (3.29)$$

$$V_c = c_{c1} \vec{\tau}_1 \cdot \vec{\tau}_2, \quad (3.30)$$

$$V_d = [c_{d1} + c_{d2} \vec{\sigma}_1 \cdot \vec{q} + c_{d3} (\vec{q} \cdot \vec{p}) + c_{d4} \vec{\sigma}_1 \cdot (\vec{q} \times \vec{p})] (\vec{\tau}_1 \cdot \vec{\tau}_2), \quad (3.31)$$

$$V_e = (c_{e1} + c_{e2} \vec{\sigma}_1 \cdot \vec{q}) (\vec{\tau}_1 \cdot \vec{\tau}_2), \quad (3.32)$$

$$V_f = \left[ c_{f1} + c_{f2} \vec{\sigma}_1 \cdot \vec{\sigma}_2 + c_{f3} \vec{\sigma}_1 \cdot \vec{q} + c_{f4} (\vec{\sigma}_1 \times \vec{\sigma}_2) \cdot \vec{q} + c_{f5} (\vec{\sigma}_1 \cdot \vec{q}) (\vec{\sigma}_2 \cdot \vec{q}) + c_{f6} (\vec{\sigma}_1 \cdot \vec{q}) (\vec{\sigma}_2 \cdot \vec{p}) + c_{f7} \vec{\sigma}_1 \cdot (\vec{p} \times \vec{q}) + c_{f8} \vec{\sigma}_2 \cdot (\vec{p} \times \vec{q}) \right] (c'_{f1} + c'_{f2} \vec{\tau}_1 \cdot \vec{\tau}_2), \quad (3.33)$$

$$V_g = \left[ c_{g1} + c_{g2} \vec{\sigma}_1 \cdot \vec{\sigma}_2 + c_{g3} (\vec{\sigma}_1 \cdot \vec{q}) (\vec{\sigma}_2 \cdot \vec{q}) \right] (c'_{g1} + c'_{g2} \vec{\tau}_1 \cdot \vec{\tau}_2) + \left[ c_{g4} \vec{\sigma}_1 \cdot \vec{q} + c_{g5} (\vec{\sigma}_1 \times \vec{\sigma}_2) \cdot \vec{q} \right] (c''_{g1} + c''_{g2} \vec{\tau}_1 \cdot \vec{\tau}_2), \quad (3.34)$$

$$V_h = \left[ c_{h1} + c_{h2} \vec{\sigma}_1 \cdot \vec{\sigma}_2 + c_{h3} \vec{\sigma}_1 \cdot \vec{q} + c_{h4} (\vec{\sigma}_1 \times \vec{\sigma}_2) \cdot \vec{q} + c_{h5} (\vec{\sigma}_1 \cdot \vec{q}) (\vec{\sigma}_2 \cdot \vec{q}) + c_{h6} (\vec{\sigma}_1 \cdot \vec{q}) (\vec{\sigma}_2 \cdot \vec{p}) + c_{h7} \vec{\sigma}_1 \cdot (\vec{p} \times \vec{q}) + c_{h8} \vec{\sigma}_2 \cdot (\vec{p} \times \vec{q}) \right] (c'_{h1} + c'_{h2} \vec{\tau}_1 \cdot \vec{\tau}_2), \quad (3.35)$$

$$V_i = \left[ c_{i1} + c_{i2} \vec{\sigma}_1 \cdot \vec{\sigma}_2 + c_{i3} (\vec{\sigma}_1 \cdot \vec{q}) (\vec{\sigma}_2 \cdot \vec{q}) \right] (c'_{i1} + c'_{i2} \vec{\tau}_1 \cdot \vec{\tau}_2) + \left[ c_{i4} \vec{\sigma}_1 \cdot \vec{q} + c_{i5} (\vec{\sigma}_1 \times \vec{\sigma}_2) \cdot \vec{q} \right] (c''_{i1} + c''_{i2} \vec{\tau}_1 \cdot \vec{\tau}_2). \quad (3.36)$$

Considering the  $SU(3)_F$  limit where all the baryon masses are considered to take the same value ( $q_0 = q'_0 = 0$ ) the expressions above become much more simple. Defining

$$At(q) \equiv \frac{1}{2q} \arctan \left( \frac{q}{2m_\pi} \right), \quad (3.37)$$

$$L(q) \equiv \frac{\sqrt{4m_\pi^2 + q^2}}{q} \ln \left( \frac{\sqrt{4m_\pi^2 + q^2} + q}{2m_\pi} \right), \quad (3.38)$$

with  $q \equiv \sqrt{\vec{q}^2}$ , and extracting the baryonic poles and the polynomial terms, one obtains,

$$V_a = -\frac{h_{\Lambda N}}{192\pi^2 f_\pi^4 (M_\Lambda - M_N)} (4m_\pi^2 + q^2) L(q) (\vec{\tau}_1 \cdot \vec{\tau}_2), \quad (3.39)$$

$$V_b = \frac{3g_A^2 h_{2\pi}}{32\pi f_\pi^4} (2m_\pi^2 + q^2) A t(q), \quad (3.40)$$

$$V_c = -\frac{g_A^2 h_{\Lambda N}}{384\pi^2 f_\pi^4 (M_\Lambda - M_N)} (8m_\pi^2 + 5q^2) L(q) (\vec{\tau}_1 \cdot \vec{\tau}_2), \quad (3.41)$$

$$V_d = \frac{g_A}{64\pi^2 f_\pi^3 M_N} L(q) (\vec{\tau}_1 \cdot \vec{\tau}_2) (-2Bm_\pi^2 - B\vec{q}^2 + B(\vec{q} \cdot \vec{p}) + 6AM_N(\vec{\sigma}_1 \cdot \vec{q}) - 3iB\vec{\sigma}_1 \cdot (\vec{q} \times \vec{p})), \quad (3.42)$$

$$V_e = \frac{\sqrt{3}D}{384\pi^2 f_\pi^3 M_N} L(q) (B_{\Sigma 1}(4m_\pi^2 + 3\vec{q}^2) - 4A_{\Sigma 1}M_N(\vec{\sigma}_1 \cdot \vec{q})), \quad (3.43)$$

$$\begin{aligned} V_f = & \frac{g_A^3}{512\pi^2 f_\pi^3 M_N (4m_\pi^2 + \vec{q}^2)} L(q) (-3 + 2\vec{\tau}_1 \cdot \vec{\tau}_2) \\ & \times \left[ \frac{1}{6} B(448m_\pi^4 + 4m_\pi^2(-24\vec{q} \cdot \vec{p} + 47\vec{q}^2) + 25\vec{q}^4 - 36\vec{q}^2(\vec{q} \cdot \vec{p})) \right. \\ & + 4iB(4m_\pi^2 + \vec{q}^2)\vec{\sigma}_2 \cdot (\vec{q} \times \vec{p}) - 4AM_N(8m_\pi^2 + 3\vec{q}^2)\vec{\sigma}_1 \cdot \vec{q} + 2iB(8m_\pi^2 + 3\vec{q}^2)\vec{\sigma}_1 \cdot (\vec{q} \times \vec{p}) \\ & + 4B(4m_\pi^2 + \vec{q}^2)(\vec{\sigma}_1 \cdot \vec{q})(\vec{\sigma}_2 \cdot \vec{p}) - 4B(4m_\pi^2 + \vec{q}^2)(\vec{\sigma}_1 \cdot \vec{q})(\vec{\sigma}_2 \cdot \vec{q}) \\ & \left. - 4B(4m_\pi^2 + \vec{q}^2)(\vec{q} \cdot \vec{p} - \vec{q}^2)(\vec{\sigma}_1 \cdot \vec{\sigma}_2) - 8iAM_N(4m_\pi^2 + \vec{q}^2)(\vec{\sigma}_1 \times \vec{\sigma}_2) \cdot \vec{q} \right], \end{aligned} \quad (3.44)$$

$$\begin{aligned} V_g = & \frac{Dg_A^2}{256\sqrt{3}\pi^2 f_\pi^3 M_N (4m_\pi^2 + \vec{q}^2)} L(q) \left[ -\frac{1}{6} B_{\Sigma 2}(448m_\pi^4 + 188m_\pi^2\vec{q}^2 + 25\vec{q}^4) \right. \\ & + 4A_{\Sigma 2}M_N(8m_\pi^2 + 3\vec{q}^2)(\vec{\sigma}_1 \cdot \vec{q}) + 4B_{\Sigma 2}(4m_\pi^2 + \vec{q}^2)(\vec{\sigma}_1 \cdot \vec{q})(\vec{\sigma}_2 \cdot \vec{q}) \\ & \left. - 4B_{\Sigma 2}(4m_\pi^2 + \vec{q}^2)\vec{q}^2(\vec{\sigma}_1 \cdot \vec{\sigma}_2) - 8iA_{\Sigma 2}M_N(4m_\pi^2 + \vec{q}^2)(\vec{\sigma}_1 \times \vec{\sigma}_2) \cdot \vec{q} \right], \end{aligned} \quad (3.45)$$

$$\begin{aligned} V_h = & \frac{g_A^3}{512\pi^2 f_\pi^3 M_N (4m_\pi^2 + \vec{q}^2)} L(q) (3 + 2\vec{\tau}_1 \cdot \vec{\tau}_2) \\ & \times \left[ \frac{1}{6} B(448m_\pi^4 + 4m_\pi^2(-24\vec{q} \cdot \vec{p} + 47\vec{q}^2) + 25\vec{q}^4 - 36\vec{q}^2(\vec{q} \cdot \vec{p})) \right. \\ & - 4iB(4m_\pi^2 + \vec{q}^2)\vec{\sigma}_2 \cdot (\vec{q} \times \vec{p}) - 4AM_N(8m_\pi^2 + 3\vec{q}^2)\vec{\sigma}_1 \cdot \vec{q} - 2iB(8m_\pi^2 + 3\vec{q}^2)\vec{\sigma}_1 \cdot (\vec{q} \times \vec{p}) \\ & + 4B(4m_\pi^2 + \vec{q}^2)(\vec{\sigma}_1 \cdot \vec{q})(\vec{\sigma}_2 \cdot \vec{p}) - 4B(4m_\pi^2 + \vec{q}^2)(\vec{\sigma}_1 \cdot \vec{q})(\vec{\sigma}_2 \cdot \vec{q}) \\ & \left. - 4B(4m_\pi^2 + \vec{q}^2)(\vec{q} \cdot \vec{p} - \vec{q}^2)(\vec{\sigma}_1 \cdot \vec{\sigma}_2) + 8iAM_N(4m_\pi^2 + \vec{q}^2)(\vec{\sigma}_1 \times \vec{\sigma}_2) \cdot \vec{q} \right], \end{aligned} \quad (3.46)$$

$$\begin{aligned} V_i = & \frac{Dg_A^2}{256\sqrt{3}\pi^2 f_\pi^3 M_N (4m_\pi^2 + \vec{q}^2)} L(q) \times \left[ \frac{1}{6} B_{\Sigma 3}(448m_\pi^4 + 188m_\pi^2\vec{q}^2 + 25\vec{q}^4) \right. \\ & + A_{\Sigma 3}M_N(8m_\pi^2 + 3\vec{q}^2)(\vec{\sigma}_1 \cdot \vec{q}) + 4B_{\Sigma 3}(4m_\pi^2 + \vec{q}^2)(\vec{\sigma}_1 \cdot \vec{q})(\vec{\sigma}_2 \cdot \vec{q}) \\ & \left. - 4B_{\Sigma 3}(4m_\pi^2 + \vec{q}^2)\vec{q}^2(\vec{\sigma}_1 \cdot \vec{\sigma}_2) + 4iA_{\Sigma 3}M_N(4m_\pi^2 + \vec{q}^2)(\vec{\sigma}_1 \times \vec{\sigma}_2) \cdot \vec{q} \right]. \end{aligned} \quad (3.47)$$

The isospin part for the potentials that contain  $\Sigma$  propagators ( $V_e$ ,  $V_g$ ,  $V_i$ ) is taken into account by making the replacements:

$$\begin{aligned} A_{\Sigma 1} &\rightarrow \frac{2}{3} \left( \sqrt{3} A_{\Sigma \frac{1}{2}} + A_{\Sigma \frac{3}{2}} \right) \vec{\tau}_1 \cdot \vec{\tau}_2, \\ B_{\Sigma 1} &\rightarrow \frac{2}{3} \left( \sqrt{3} B_{\Sigma \frac{1}{2}} + B_{\Sigma \frac{3}{2}} \right) \vec{\tau}_1 \cdot \vec{\tau}_2; \end{aligned} \quad (3.48)$$

$$\begin{aligned} A_{\Sigma 2} &\rightarrow -\sqrt{3} A_{\Sigma \frac{1}{2}} + 2 A_{\Sigma \frac{3}{2}} + \frac{2}{3} (\sqrt{3} A_{\Sigma \frac{1}{2}} + A_{\Sigma \frac{3}{2}}) \vec{\tau}_1 \cdot \vec{\tau}_2, \\ B_{\Sigma 2} &\rightarrow -\sqrt{3} B_{\Sigma \frac{1}{2}} + 2 B_{\Sigma \frac{3}{2}} + \frac{2}{3} (\sqrt{3} B_{\Sigma \frac{1}{2}} + B_{\Sigma \frac{3}{2}}) \vec{\tau}_1 \cdot \vec{\tau}_2; \end{aligned} \quad (3.49)$$

$$\begin{aligned} A_{\Sigma 3} &\rightarrow -\sqrt{3} A_{\Sigma \frac{1}{2}} + 2 A_{\Sigma \frac{3}{2}} - \frac{2}{3} (\sqrt{3} A_{\Sigma \frac{1}{2}} + 2 A_{\Sigma \frac{3}{2}}) \vec{\tau}_1 \cdot \vec{\tau}_2, \\ B_{\Sigma 3} &\rightarrow -\sqrt{3} B_{\Sigma \frac{1}{2}} + 2 B_{\Sigma \frac{3}{2}} - \frac{2}{3} (\sqrt{3} B_{\Sigma \frac{1}{2}} + 2 B_{\Sigma \frac{3}{2}}) \vec{\tau}_1 \cdot \vec{\tau}_2. \end{aligned} \quad (3.50)$$

To obtain the coefficients accompanying the isospin operators 1 and  $\vec{\tau} \cdot \vec{\tau}$  we calculate each diagram in the particle basis and then relate them to the results obtained by the isospin operators. Note that Eqs. (3.39) and (3.41) only have physical meaning away from the  $SU(3)_F$  limit.

We note here that the role played by the two-pion exchange mechanism in the weak decay of hypernuclei was also considered in Ref. [18]. This work scaled the expressions obtained in the strong NN sector within the chiral unitary approach [97] to account for the parity-conserving amplitudes in the weak transitions, the scaling factor being the ratio between the weak and strong baryon-baryon-meson coupling constants. Although a direct comparison between our EFT approach and Ref. [18] cannot be made, the results of Ref. [18] provide an insight effective field theory approach, provide an insight on the role played by the interferences between the different diagrams considered (one-meson exchange and uncorrelated and correlated two-pion exchanges).

### 3.4.3 Master integrals and their relations

In this section we briefly review the technical part of the loop calculation. The main complication arises from the integrals that appear in the different NLO two-pion exchange diagrams. These loop diagrams contain a momentum, carried by the hadrons forming the loop, that is not constrained by the external momenta and that must be integrated to account for all the possibilities. The corresponding integrals have ultraviolet divergences and therefore must be regularized. In our work, we use the dimensional regularization approach. These integrals depend on the number and type of propagators (baryonic or mesonic), which appear as denominators, and on the type of vertices, which appear as momenta in the numerator. The integrals are therefore classified according to the different topologies the diagrams may have: balls, triangles and boxes. Let us focus on the triangle diagrams, which contain a baryonic (non-relativistic) propagator, two pionic (relativistic)

ones, and up to three momenta in the numerator (one for each vertex):

$$I_{;\mu;\mu\nu;\mu\nu\rho} \equiv \frac{1}{i} \int \frac{d^4 l}{(2\pi)^4} \frac{1}{l^2 - m^2 + i\epsilon} \frac{1}{(l+q)^2 - m^2 + i\epsilon} \frac{1}{-l_0 - q'_0 + i\epsilon} (1; l_\mu; l_\mu l_\nu; l_\mu l_\nu l_\rho),$$

where the semicolons separate the different possible numerators.

These integrals, as well as the ones appearing in the ball and box diagrams, have already been calculated with  $q_0 = q'_0 = 0$  (for example see Ref. [98]). In our calculation, we choose to keep these quantities explicitly, but the strategy we follow is the same: we calculate only the integrals without momenta in the numerator, which are called master integrals, and then relate the others with them through Veltman-Passarino tricks [99]. For example, one can replace an  $l_0$  in the numerator of  $I_0$  by  $(l_0 + q'_0) - q'_0$  and obtain thus two simpler integrals (one with one denominator less and one with one momentum less in the numerator). The full set of relations and master integrals are shown in the App. E.

To show how  $q_0$  and  $q'_0$  contribute at this level of the calculation, we plot in Fig. 3.13 the master integral  $I$  as a function of  $q$  and with the quantities  $q_0$  and  $q'_0$  that appear in the different triangle diagrams. Fig. 3.13 shows that the master integral is quite sensible of  $q_0$  and  $q'_0$ . In the next chapter we show the comparison of the potentials with and without these quantities taken into account.

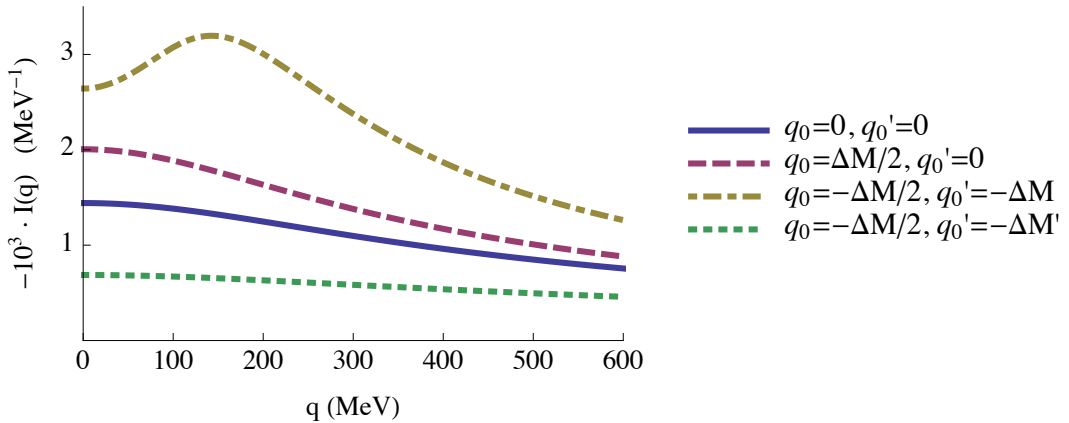


Figure 3.13: Comparison of the master integral  $I$  with  $q_0 = q'_0 = 0$  and with the actual  $q_0$  and  $q'_0$  that appear in the heavy baryon expansion of the different triangle diagrams. We have defined  $\Delta M = M_\Lambda - M_N$  and  $\Delta M' = M_\Sigma - M_N$ .



# Chapter 4

## Results

The formalism developed in the two previous chapters allows us to compute the different hypernuclear decay observables. First, in Chapter 2, we have presented the formalism describing the strong interactions taking place in the initial hypernuclei and in the nuclear products which result from the weak decay. Following the two schemes presented in Chapter 2, this chapter is also mainly divided in two sections, one for light hypernuclei and one for the hypertriton. Second, the potential driving the weak  $\Lambda N \rightarrow NN$  transition, has been derived in Chapter 3.

In the description of light hypernuclei, we have used different models to account for the strong interactions. The initial wave function has been described by a shell model approach, while making use of spectroscopic factors to account for the nuclear structure. For the final strong interactions among the two outgoing nucleons two potentials have been used, one from the Nijmegen group (NSC97f) and one from the Jülich group. These potentials were developed in the late eighties and nineties and are based on one-meson-exchange models for the baryon-baryon interaction. They are  $SU(3)_F$  extensions of previously and successfully developed nucleon-nucleon potential models.  $SU(3)_F$  symmetry is then broken in several ways, as for example by using the physical values for the masses of the mesons and the baryons or by including charge-symmetry breaking terms and the Coulomb interaction explicitly. In the case of NSC97, the potential includes the contribution of the pseudoscalar  $\pi$ ,  $\eta$ ,  $\eta'$  and  $K$  mesons the vector  $\rho$ ,  $\phi$ ,  $\omega$  and  $K^*$  mesons, the scalar  $a_0(980)$ ,  $f_0(975)$ , and  $\kappa(880)$ , and the diffractive contribution from the pomeron  $P$  and from the tensor  $f_2(1285)$ ,  $f'_2(1525)$ ,  $a_2(1270)$  mesons [94]. The Jülich model is based on the Bonn meson-exchange model for the  $NN$  interaction, which includes not only one-meson-exchange potentials but also explicit two-pion-exchange contributions involving the  $\Delta$ -isobar in intermediate states. Additionally, the Jülich model includes the degrees of freedom relevant in the  $YN$  interaction, namely the  $\Lambda$ ,  $\Sigma$  and  $Y^*$  hyperons, the pseudoscalar  $\pi$ ,  $K$  mesons and the vector  $\rho$  and  $\omega$  mesons. Both models reproduce, with great precision, the properties of the deuteron, e.g. binding energy, and also the low energy  $NN$  and  $YN$  scattering experimental data. However, these models show differences in the baryon-baryon phase shifts and are subject to predict different results when applied in other processes, as for example in the study of the hypernuclear decay quantities [29]. More recently, new versions of these meson-exchange based models have been developed. As an example, the extended soft-core potential [100] includes apart from the one-boson

exchanges, the exchanges of two-mesons, meson pairs and multiple gluons, together with quark-core effects. Although we have not used these more recent versions in our problem, they are being tested by other groups in different physical situations where the strangeness plays an important role, specially in the study of hypernuclear structure.

From the discussion above, one expects that the predictions for the observables of the decay of light hypernuclei is subject to a model dependence tied to different baryon-baryon strong interaction models used to describe the initial hypernuclear wave function and the final interactions among the decay products. In order to reduce these model dependencies we have performed a calculation for the decay of the hypertriton, where the strong interactions in both the initial and final state have been described with potentials derived within an effective field theory (EFT) framework. These strong EFT potentials, in contrast with the one-meson-exchange ones, include the most general interactions up to a certain order in the momentum expansion, while being constrained by the chiral symmetry of QCD. During the last decade the EFT for the nucleon-nucleon interaction has been developed up to next-to-next-to-next-to-leading order (3NLO) in the momentum expansion, and the corresponding low-energy coefficients (LEC's) have been fitted to the experimental data on low energy NN and YN scattering and nuclear bound states.

The weak four-body  $\Delta S = 1$  transition has also been described with an EFT potential. This potential has been derived in Chapter 3 up to order  $\mathcal{O}(\vec{q}^2)$  order. All the parameters entering this potential—the couplings among mesons and baryons and the form factors—have been provided correspondingly. We note that for the kaon strong couplings to the baryons, which are not known experimentally and must be derived using  $SU(3)_F$  symmetry, we have used the ones given by the NSC97f and Jülich models. The weak vertices for the coupling of the mesons to the baryons have two different amplitudes, one that conserves parity and one that violates parity. The corresponding coupling constants are taken from Ref. [17], where the soft-meson reduction theorem and the pole model are used to derive their values. The short range part of the potential is described by a set of contact interactions that are accompanied by low energy constants. These constants are not known and must be fitted by the available experimental data constraining the  $\Lambda N \rightarrow NN$  transition.

In the first section of this chapter we review the available experimental data set for the non-mesonic hypernuclear decay. There are three independent quantities that have been measured for various hypernuclei: the total and partial decay rates and the parity violating asymmetry in the outgoing protons respect to the hypernuclear polarization axis. In s-shell hypernuclei, such as  ${}^5_{\Lambda}\text{He}$ , both of the initial interacting baryons, the  $\Lambda$  and the nucleon, are in an s-shell, while in p-shell hypernuclei the nucleons may be in an s-shell or a p-shell. Therefore, most optimistically, one may consider to have six independent observables, three for s-shell hypernuclei and three for p-shell hypernuclei. In contrast, the EFT weak potential contains two LEC's at order  $\mathcal{O}(\vec{q}^0)$ , six at order  $\mathcal{O}(\vec{q})$ , and seven at order  $\mathcal{O}(\vec{q}^2)$ . The current number and precision of the measurements on the non-mesonic decay of light hypernuclei only allow us to fairly constrain the two leading order (LO) LEC's.

In Sec. 4.2 we fit these two LEC's to the total and partial decay rates and the parity violating asymmetry for three light hypernuclei:  ${}^5_{\Lambda}\text{He}$ ,  ${}^{11}_{\Lambda}\text{B}$ , and  ${}^{12}_{\Lambda}\text{C}$ . As an alternative way to fix the two LO LEC's, in Sec. 4.3, we compare the corresponding LO EFT potential

with the one-meson exchange (OME) potential. Through this comparison, we write the two LO LEC's in terms of the parameters appearing in the OME description.

There are no experimental data on the decay of the hypertriton and therefore it is currently not possible to fit the LEC's using the Faddeev-Yakubovski scheme and EFT formalism developed in Chapter 2. In Sec. 4.3 we show how our prediction for the hypertriton nonmesonic decay depends on the values of the two LO LEC's. We also briefly compare our results with previous works that have studied the decay of the hypertriton.

In order to get some insight into the size of the loop corrections to the tree-level calculation, in the last section we compare the pion and kaon contributions with the different terms coming from the two-pion exchange diagrams.

The OME potentials entering the calculation in the two first sections, 4.2 and 4.3, have been calculated using the Lagrangians listed in the Appendix F. The potentials used in the sections 4.4 and 4.5, i.e. the one-pion, the one-kaon and the two-pion exchanges, have been explicitly derived in the previous chapter.

## 4.1 Experimental data on the hypernuclear decay observables

In this section we briefly review the recent experimental data on the non-mesonic weak decay of hypernuclei, focusing mainly on the values we use in the fitting, which are obtained from the different experiments carried in KEK, Japan.

The decay of hypernuclei was first measured in emulsion and bubble chamber experiments in the 50's, where a few light hypernuclei were observed to decay. The first counter experiments capable of measuring the total and partial decay rates were carried at Brookhaven National Laboratory (BNL) in the early 90's, through the  $n(K^-, \pi^-)\Lambda$  reaction. However, these experiments were restricted to measurements of the decays of only the  $^{11}\Lambda$ B and the  $^{12}\Lambda$ C systems. During the last two decades the decay observables of a wider variety of hypernuclei have been measured with greater precision through different reactions; namely at BNL with the  $n(K^-, \pi^-)\Lambda$  reaction, at KEK with the  $n(\pi^+, K^+)\Lambda$  reaction, and more recently at the Laboratori Nazionali di Frascati (LNF) with the  $n(K_{stop}^-, \pi^-)\Lambda$  reaction.

In Table 4.1, we show, in chronological order, the different experiments on hypernuclear decay and the corresponding observables that have been measured. These observables consist of the total and partial decay rates,  $\Gamma_{nm}$  and  $\Gamma_n/\Gamma_p$ , and the asymmetry in the angular distribution of protons coming from the decay of polarized hypernuclei. The same table also shows the experiments that have focused in the extraction of two-particle energy and angular correlated spectra, a method that has proved to be more convenient to extract a clean value for the relation of the partial decay rates. In recent years it has also been possible to measure the two-nucleon induced decay,  $\Gamma_{2N}$ , in the LNF facility. The corresponding hypernuclei range from the very light,  $^4\Lambda$ He, up to the medium-heavy ones,  $^{27}\Lambda$ Al,  $^{28}\Lambda$ Si, with the exception of  $^{89}\Lambda$ Y.

In our calculation we have focused in describing the non-mesonic decay observables of three hypernuclei,  $^5\Lambda$ He,  $^{11}\Lambda$ B, and  $^{12}\Lambda$ C, representing both s-shell and p-shell nuclei. In Table 4.2 we list the eleven experimental data points and their errors that are used in the

Experiment	Measurement
BNL-AGS LESB I (1991)	${}^5_{\Lambda}\text{He}$ : p spectrum, $\Gamma_p$ , $\Gamma_n$ , $\Gamma_{nm}$ and $\Gamma_n/\Gamma_p$ . ${}^{12}_{\Lambda}\text{C}$ : $\Gamma_{nm}$ and $\Gamma_n/\Gamma_p$ .
KEK-PS E160 (1995)	${}^{11}_{\Lambda}\text{B}$ : $\Gamma_p$ , $\Gamma_{nm}$ and $\Gamma_n/\Gamma_p$ . ${}^{12}_{\Lambda}\text{C}$ : p spectrum, $\Gamma_p$ , $\Gamma_{nm}$ and $\Gamma_n/\Gamma_p$ .
KEK-PS E307 (2002)	${}^{12}_{\Lambda}\text{C}$ , ${}^{28}\text{Si}$ : p spectrum and $\Gamma_n/\Gamma_p$ .
KEK-PS E369 (2003)	${}^{12}_{\Lambda}\text{C}$ : n spectrum and $\Gamma_n/\Gamma_p$ . ${}^{89}\text{Y}$ : n spectrum.
KEK-PS E462-E508 (2004)	${}^5_{\Lambda}\text{He}$ , ${}^{12}_{\Lambda}\text{C}$ : p and n spectra and $\Gamma_n/\Gamma_p$ .
KEK-PS E307 (2005)	${}^{11}_{\Lambda}\text{B}$ , ${}^{12}_{\Lambda}\text{C}$ , ${}^{27}\text{Al}$ , ${}^{28}\text{Si}$ , ${}_{\Lambda}\text{Fe}$ : p spectrum and $\Gamma_{nm}$ .
KEK-PS E462 (2006)	${}^5_{\Lambda}\text{He}$ : p and n spectra and $\Gamma_n/\Gamma_p$ .
KEK-PS E508 (2006)	${}^{12}_{\Lambda}\text{C}$ : p and n spectra and $\Gamma_n/\Gamma_p$ .
KEK-PS E462-E508 (2007)	${}^5_{\Lambda}\text{He}$ : p and n spectra. ${}^{12}_{\Lambda}\text{C}$ : p and n spectra and $\Gamma_n/\Gamma_p$ (reanalysis).
BNL-AGS LESB II (2007)	${}^4_{\Lambda}\text{He}$ : $\Gamma_n$ , $\Gamma_p$ and $\Gamma_n/\Gamma_p$ .
LNF (2008)	${}^5_{\Lambda}\text{He}$ , ${}^7_{\Lambda}\text{Li}$ and ${}^{12}_{\Lambda}\text{C}$ : p spectrum.
KEK-PS E508 (2009)	${}^{12}_{\Lambda}\text{C}$ : p and n spectra, $\Gamma_n$ , $\Gamma_p$ , $\Gamma_{2N}$ (reanalysis).
LNF (2010)	${}^5_{\Lambda}\text{He}$ , ${}^7_{\Lambda}\text{Li}$ , ${}^{11}\text{B}$ , ${}^{12}_{\Lambda}\text{C}$ , ${}^{13}_{\Lambda}\text{C}$ , ${}^{15}\text{N}$ and ${}^{16}_{\Lambda}\text{O}$ : p spectrum
LNF (2011)	${}^5_{\Lambda}\text{He}$ , ${}^7_{\Lambda}\text{Li}$ , ${}^9\text{Be}$ , ${}^{11}\text{B}$ , ${}^{12}_{\Lambda}\text{C}$ , ${}^{13}_{\Lambda}\text{C}$ , ${}^{15}\text{N}$ and ${}^{16}_{\Lambda}\text{O}$ : n and p coincidence

Table 4.1: Experiments on the non-mesonic weak decay of hypernuclei together with the observables that have been measured and studied. The laboratories BNL, KEK and LNF use, respectively, the reactions  $(K^-, \pi^-)$ ,  $(\pi^+, K^+)$  and  $(K_{stop}^-, \pi^-)$  [101].

fitting process described in the following section. Only the more recent and/or precise results are included in the fit. Note that the only available asymmetries are for  ${}^5_{\Lambda}\text{He}$ , all of which are compatible with zero, and that for  ${}^{11}\text{B}$  we only use the total decay rate.

## 4.2 LO EFT for ${}^5_{\Lambda}\text{He}$ , ${}^{11}\text{B}$ , and ${}^{12}_{\Lambda}\text{C}$

According to Eq. (3.17) the LO EFT potential for the weak  $\Lambda N \rightarrow NN$  transition accounts for the short range part with two contact interactions,

$$V_{4P} = C_{00} + C_{01} \vec{\sigma}_1 \cdot \vec{\sigma}_2. \quad (4.1)$$

The constants  $C_{00}$  and  $C_{01}$  depend on the short range physics of the  $\Lambda N \rightarrow NN$  transition. To fix their values we use the different hypernuclear decay observables: the total and partial decay rates and the parity violating asymmetry for  ${}^5_{\Lambda}\text{He}$ ,  ${}^{11}\text{B}$ , and  ${}^{12}_{\Lambda}\text{C}$ . While the interacting  $\Lambda$  and nucleon in  ${}^5_{\Lambda}\text{He}$  are always on an s-shell, in the  ${}^{11}\text{B}$ , and  ${}^{12}_{\Lambda}\text{C}$  they may

Hypernucleus	Experiment	Observable
${}^5_{\Lambda}\text{He}$	KEK-PS E160 (1995)	$\Gamma_{nm} = 0.50 \pm 0.07$ [102]
	KEK-PS E462 (2006)	$\Gamma_n/\Gamma_p = 0.450 \pm 0.114$ [12]
	KEK-PS E160 (2000)	$\mathcal{A} = 0.24 \pm 0.22$ [103]
	KEK-PS E462 (2006)	$\mathcal{A} = 0.11 \pm 0.09$ [12]
	KEK-PS E462 (2006)	$\mathcal{A} = 0.07 \pm 0.08$ [104]
${}^{11}_{\Lambda}\text{B}$	KEK-PS E160 (1995)	$\Gamma_{nm} = 0.95 \pm 0.14$ [105]
	KEK-PS E307 (2005)	$\Gamma_{nm} = 0.861 \pm 0.096$ [13]
${}^{12}_{\Lambda}\text{C}$	KEK-PS E160 (1995)	$\Gamma_{nm} = 0.89 \pm 0.18$ [105]
	KEK-PS E307 (2000)	$\Gamma_{nm} = 0.83 \pm 0.11$ [106]
	KEK-PS E307 (2005)	$\Gamma_{nm} = 0.828 \pm 0.087$ [13]
	KEK-PS E369 (2003)	$\Gamma_n/\Gamma_p = 0.51 \pm 0.14$ [107]

Table 4.2: Experimental values for the total and partial decay rates and the parity violating asymmetry and their errors that have been used in the fitting of the LO LEC's.

be either on an s-shell or a p-shell. Therefore, most optimistically, one may consider to have six independent observables. In our approach we have considered the most recently measured observables and with most accuracy, all obtained in the KEK experiments in Japan. These add up to a total of eleven experimental data points and are listed in the Table 4.2 of the previous section.

The fitting of the LEC's has been computed by implementing the weak EFT potential, described in the previous section, in a hypernuclear code that uses the subroutine minuit [108] to minimize the corresponding chi-squared test,  $\chi^2$ . Since in our formalism we have used two strong interaction models, Nijmegen Soft-Core 97f (NSC97f) and Jülich, we obtain two different set of results.

For each one of the strong interaction models we obtain two different minima. The two models not only differ on the kaon exchange contribution (coupling constants and cutoffs), but they also generate different  $NN$  wave functions. The low energy constants that account for the different observables are listed inn Tab. 4.3. The  $\chi^2$  values for the corresponding fits to 11 observables are also given in the table. Three of the minima have total  $\chi^2$  well below the total number of points. However the LEC's for these three minima are not compatible with each other. The strong model dependencies that we see in these results suggest the use of EFT also in the strong sector. This has motivated us to study the decay of the lightest hypernucleus, the hypertriton, within the EFT framework in both the weak and the strong parts. We show and discuss the corresponding results in Sec. 4.4.

In Fig. 4.1 we show the values for the observables used in the present fit together with their respective fitted values, while Fig. 4.2 shows the contribution of each point to the  $\chi^2$ . Almost all the fitted points fall into the error bars of the corresponding experimental data points, and therefore contribute with a  $\chi^2$  per point smaller than one. For both strong

	Nijmegen		Jülich	
	LO PC calculation		LO PC calculation	
$C_{00}$	$-0.92 \pm 0.31$	$4.01 \pm 0.23$	$4.03 \pm 0.50$	$0.89 \pm 0.58$
$C_{10}$	$-2.41 \pm 0.11$	$0.02 \pm 0.33$	$-0.30 \pm 0.28$	$-1.52 \pm 0.18$
$\chi^2$	3.89	13.43	4.26	4.58

Table 4.3: Values for the LEC's obtained from the two sources: OME expansion and LO (PC) EFT calculation, using the NSC97f and Jülich strong interaction models. All the quantities are in units of  $G_F = 1.166 \times 10^{-11} \text{ MeV}^{-2}$ .

models used, NSC97f and Jülich, a set of LEC's is found to be compatible with the data. One can see that the LO EFT is already capable to describe the current experimental data on hypernuclear decay.

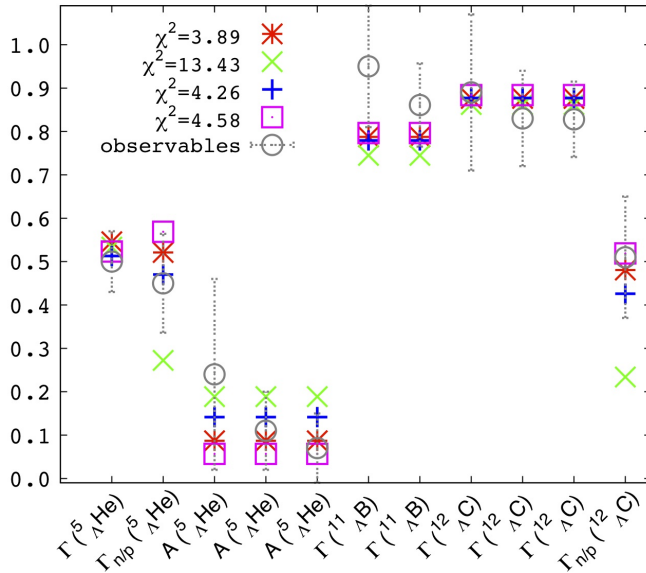


Figure 4.1: Hypernuclear decay observables (total and partial decay rates and asymmetry for  ${}^5\Lambda\text{He}$ ,  ${}^{11}\Lambda\text{B}$  and  ${}^{12}\Lambda\text{C}$ ), including their error bars and their fitted values. The total decay rates are in units of the  $\Lambda$  decay rate in free space ( $\Gamma_\Lambda = 3.8 \times 10^9 \text{ s}^{-1}$ ). All the quantities are adimensional.

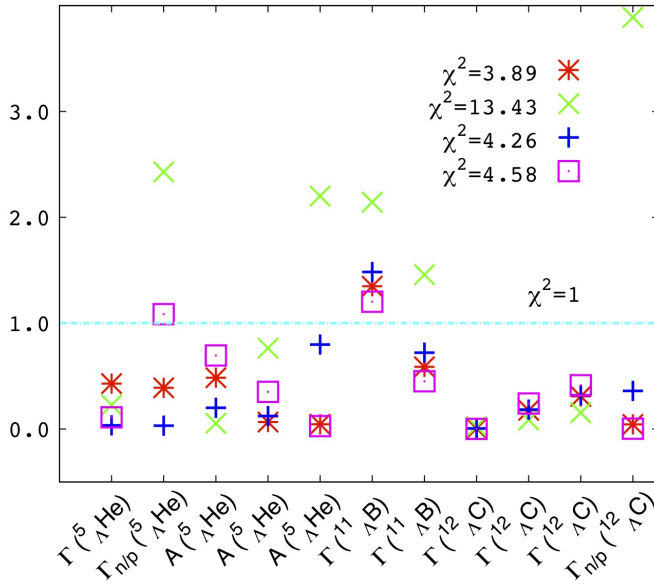


Figure 4.2: Contribution of each experimental point included in the fit to the total  $\chi^2$  for the four different fits discussed in the text.

### 4.3 Relations between the one-meson exchange potentials and the EFT

In the previous section we show that the LO LEC's can be fairly constrained by the experiments on hypernuclear decay. An alternative way to obtain the numerical values for these constants, and at the same time get some insight on their dynamical origin, is by a direct comparison to the one-meson-exchange model describing the same interaction. This idea is called resonance saturation and has been applied before in the strong NN contact interaction [109]. In this case, the values found from a fit to the low energy partial waves appear to be very close to the ones extracted from the phenomenological one-boson-exchange and various other modern nucleon-nucleon potentials.

In the OME picture the  $\Lambda N \rightarrow NN$  transition is described by the exchange of the lightest pseudoscalar ( $\pi$ ,  $K$  and  $\eta$ ) and vector ( $\rho$ ,  $\omega$  and  $K^*$ ) mesons. While the short range part in the EFT potential is accounted by the two contact operational structures, in the OME picture is accounted by the heavy meson exchanges. This kind of comparison can also shed some light into identifying possible deficiencies (disregarded contributions) in the OME picture. To relate the meson-exchange constants to the LEC's in the effective  $\Lambda N \rightarrow NN$  potential, we perform a low-momentum expansion of the various (regularized) meson-exchange potentials other than the pion and the kaon, since these two are explicitly included in both, the OME and the EFT approaches. This procedure leads to a series of contact terms organized by their increasing dimension (i.e., with increasing powers of momenta), an appropriate form to compare with the EFT potential. Therefore, one can

write these terms up to  $\mathcal{O}(\vec{q}^2/M^2)$  order (in units of  $G_F = 1.166 \times 10^{-11}$  MeV $^{-2}$ ) as:

$$\begin{aligned} V_{OME}^{(0)}(\vec{q}) &= \left[ \frac{g_{\Lambda NK^*}^V}{m_{K^*}^2} \left( \frac{C_{K^*}^{PC,V}}{2} + D_{K^*}^{PC,V} \right) + \frac{g_{NN\omega}^V \alpha_\omega}{m_\omega^2} \right. \\ &\quad \left. + \left( \frac{g_{\Lambda NK^*}^V C_{K^*}^{PC,V}}{2m_{K^*}^2} + \frac{g_{NN\rho}^V \alpha_\rho}{m_\rho^2} \right) \vec{\tau}_1 \cdot \vec{\tau}_2 \right] m_\pi^2 , \end{aligned} \quad (4.2)$$

$$\begin{aligned} V_{OME}^{(1)}(\vec{q}) &= \frac{-m_\pi^2}{2M} \frac{A_\eta g_{NN\eta}}{m_\eta^2} \vec{\sigma}_2 \vec{q} \\ &\quad - \frac{m_\pi^2}{2M} \left[ \left( \frac{i(g_{\Lambda NK^*}^V + g_{\Lambda NK^*}^T)(C_{K^*}^{PV}/2 + D_{K^*}^{PV}) m_\pi^2}{m_{K^*}^2} + \frac{i(g_{NN\omega}^V + g_{NN\omega}^T) \epsilon_\omega m_\pi^2}{m_\omega^2} \right) \right. \\ &\quad \left. + \left( \frac{i(g_{\Lambda NK^*}^V + g_{\Lambda NK^*}^T) C_{K^*}^{PV} m_\pi^2}{2m_{K^*}^2} + \frac{i(g_{NN\rho}^V + g_{NN\rho}^T) \epsilon_\rho m_\pi^2}{m_\rho^2} \right) \vec{\tau}_1 \cdot \vec{\tau}_2 \right] (\vec{\sigma}_1 \times \vec{\sigma}_2) \vec{q} , \end{aligned} \quad (4.3)$$

$$\begin{aligned} V_{OME}^{(2)}(\vec{q}) &= \frac{m_\pi^2}{4M\bar{M}} \left[ \left( \frac{C_{K^*}^{PC,V}}{2} + D_{K^*}^{PC,V} + \frac{C_{K^*}^{PC,T}}{2} + D_{K^*}^{PC,T} \right) \frac{g_{\Lambda NK^*}^V + g_{\Lambda NK^*}^T}{m_{K^*}^2} \right. \\ &\quad + \frac{(\alpha_\omega + \beta_\omega)(g_{NN\omega}^V + g_{NN\omega}^T)}{m_\omega^2} + \left( \frac{(C_{K^*}^{PC,V} + C_{K^*}^{PC,T})(g_{\Lambda NK^*}^V + g_{\Lambda NK^*}^T)}{2m_{K^*}^2} \right. \\ &\quad \left. + \frac{(\alpha_\rho + \beta_\rho)(g_{NN\rho}^V + g_{NN\rho}^T)}{m_\rho^2} \right) \vec{\tau}_1 \cdot \vec{\tau}_2 (\vec{\sigma}_1 \vec{q} \vec{\sigma}_2 \vec{q} - \vec{\sigma}_1 \vec{\sigma}_2 \vec{q}^2) \\ &\quad - \frac{m_\pi^2}{4M\bar{M}} \frac{B_\eta g_{NN\eta}}{m_\eta^2} \vec{\sigma}_1 \vec{q} \vec{\sigma}_2 \vec{q} + \left[ \frac{g_{\Lambda NK^*}^V}{m_{K^*}^2} \left( \frac{C_{K^*}^{PC,V}}{2} + D_{K^*}^{PC,V} \right) \left( -\frac{1}{m_{K^*}^2} - \frac{2}{\Lambda^2} \right) \right. \\ &\quad + \frac{g_{NN\omega}^V \alpha_\omega}{m_\omega^2} \left( -\frac{1}{m_\omega^2} - \frac{2}{\Lambda^2} \right) \\ &\quad \left. + \left( \frac{g_{\Lambda NK^*}^V C_{K^*}^{PC,V}}{2m_{K^*}^2} \left( -\frac{1}{m_{K^*}^2} - \frac{2}{\Lambda^2} \right) + \frac{g_{NN\rho}^V \alpha_\rho}{m_\rho^2} \left( -\frac{1}{m_\rho^2} - \frac{2}{\Lambda^2} \right) \right) \vec{\tau}_1 \cdot \vec{\tau}_2 \right] m_\pi^2 , \end{aligned} \quad (4.4)$$

where the values for all the couplings, masses and form cut-offs are listed in the Appendix G.

We have chosen to show the explicit expressions of the LEC's in terms of meson-exchange parameters in the Appendix H. Here we only quote the relations at LO. In order to compare these expressions with the 4P potential of Eq. (4.1) we need to use the same basis of operators. Note that, in principle, one could write, at order  $\mathcal{O}(\vec{q}^2)$ , another set of eight operators containing the isospin structure  $\vec{\tau}_1 \cdot \vec{\tau}_2$ . However, once one imposes that the final two-nucleon state must be antisymmetric, the number of structures in the effective potential is reduced to half the original, leaving to only eight independent operators. The relation between the LO constants appearing in Eq. (4.1) and the ones in the non-antisymmetrized potential,

$$V_{4P}^{(0)}(\vec{q}) = C_{00}^{sc} + C_{00}^{vec} \vec{\tau}_1 \vec{\tau}_2 + C_{01}^{sc} \vec{\sigma}_1 \vec{\sigma}_2 + C_{01}^{vec} \vec{\sigma}_1 \vec{\sigma}_2 \vec{\tau}_1 \vec{\tau}_2 , \quad (4.5)$$

is the following:

$$C_{00} = C_{00}^{sc} - 2 C_{01}^{vec} - 3 C_{01}^{vec} \quad (4.6)$$

$$C_{01} = C_{01}^{sc} - C_{01}^{vec}. \quad (4.7)$$

Comparing Eq. (4.5) and Eq. (4.2) we obtain the LO LEC's in terms of the meson parameters:

$$C_{00} = \left[ \frac{g_{\Lambda N K^*}^V}{m_{K^*}^2} \left( \frac{C_{K^*}^{PC,V}}{2} + D_{K^*}^{PC,V} \right) + \frac{g_{NN\omega}^V \alpha_\omega}{m_\omega^2} - \frac{g_{\Lambda N K^*}^V C_{K^*}^{PC,V}}{m_{K^*}^2} - \frac{2 g_{NN\rho}^V \alpha_\rho}{m_\rho^2} \right] m_\pi^2, \quad (4.8)$$

$$C_{01} = \left[ -\frac{g_{\Lambda N K^*}^V C_{K^*}^{PC,V}}{2m_{K^*}^2} - \frac{g_{NN\rho}^V \alpha_\rho}{m_\rho^2} \right] m_\pi^2. \quad (4.9)$$

In Table 4.4 we show the results for the LEC's obtained within both formalisms. On the one hand, we quote the values for the coefficients obtained from Eqs. (4.8) and (4.9) (left column, under the label: OME expansion). The numerical values for the constants in front of the spin-isospin operators have been obtained for each strong interaction model, and Eqs. (4.6) and (4.7) have been used to obtain the LO coefficients in the basis of operators  $\hat{1}$ ,  $\vec{\sigma}_1 \cdot \vec{\sigma}_2$ . On the other hand, we show the values obtained from the fit of our EFT to reproduce the experimental data, as described in the previous section (right column, under the label: LO calculation). Notice that the values derived from the OME approach do not arise from any fit to the observables but from  $SU(3)_F$  symmetry considerations together with studies of the strong baryon-baryon interaction. Their errors are estimated considering an uncertainty in the couplings of  $\pm 30\%$  based on an upper limit for  $SU(3)_F$  symmetry breaking.

The results in Table 4.4 show two important features. First, the LEC's derived using the input of the two strong OME models considered, NSC97f and Jülich, are compatible albeit mostly due to the large theoretical uncertainties. The OME prediction for  $C_{01}$  is in both cases compatible with zero. Second, the comparison between the OME extracted LEC's values and the LO PC fitted ones shows only partial agreement. The largest disagreement is seen in  $C_{00}$  in all cases. In the next section we will discuss how this disagreement can be concealed with the requirement of an extra exchange in the weak OME model, compatible with the inclusion of a scalar meson.

Note that the results for the LEC's presented here are different from the ones given in Ref. [58]. This comparison has to be made with the results obtained with the Nijmegen

	Nijmegen		Jülich			
	OME expansion	LO PC calculation	OME expansion	LO PC calculation		
$C_{00}$	$1.07 \pm 0.88$	$-0.92 \pm 0.31$	$4.01 \pm 0.23$	$-1.7 \pm 2.6$	$4.03 \pm 0.50$	$0.89 \pm 0.58$
$C_{01}$	$0.02 \pm 0.36$	$-2.41 \pm 0.11$	$0.02 \pm 0.33$	$0.12 \pm 0.37$	$-0.30 \pm 0.28$	$-1.52 \pm 0.18$
$\chi^2$		3.89	13.43		4.26	4.58

Table 4.4: Values for the LEC's obtained from the two sources: OME expansion and LO (PC) EFT calculation, using the Nijmegen Soft-Core 97f and Jülich strong interaction models. All the quantities are in units of  $G_F = 1.166 \times 10^{-11}$  MeV $^{-2}$ .

NSC97f strong interaction model, which is the only one used in [58]. Apart from small (kinematical) changes in the final  $NN$  wave functions, and in the regularization of the OKE mechanism, the main difference between both calculations resides in the experimental values used to perform the fit. The data set has been updated in comparison to Ref. [58] in order to include the recent rates extracted from the single and correlated energy and angular particle spectra, with the measure in coincidence of the two nucleons in the final state. This method, for example, allows the experimentalist to extract more cleanly the value of the  $\Gamma_n/\Gamma_p$  ratio, which has been placed to values 0.5, in contrast to previous measures which quote a number close to 1 for this quantity. Therefore, values of the neutron-to-proton ratio ( $\Gamma_n/\Gamma_p$ ) close to one have been disregarded, following the last experimental and theoretical analysis, and more accurate data with smaller error bars have been included.

### 4.3.1 Scalar exchange interaction

By inspecting Table 4.4 one clearly sees that the largest discrepancy affects the  $C_{00}$  coefficient, which determines the size of the scalar isoscalar contribution in the EFT. This could be an indication of the need of a scalar exchange, previously disregarded, in meson-exchange models of the weak baryon-baryon interaction.

A sensible way of inferring qualitatively the physical properties of such scalar would be to add it to the meson exchange model described before. The one-scalar-exchange (OSE) contribution can be obtained from the following weak and strong vertices:

$$\mathcal{L}_{NN\sigma}^S = -g_{NN\sigma}\bar{\psi}_N\phi^\sigma\psi_N, \quad (4.10)$$

$$\mathcal{L}_{\Lambda N\sigma}^W = -G_F m_\pi^2 \bar{\psi}_N (A_\sigma + B_\sigma \gamma_5) \phi^\sigma \psi_\Lambda \begin{pmatrix} 0 \\ 1 \end{pmatrix}, \quad (4.11)$$

where  $A_\sigma$  and  $B_\sigma$  parameterize the parity-conserving and parity-violating weak amplitudes. In the non-relativistic approximation, the corresponding potential reads,

$$V_{OSE}(\vec{q}) = -G_F m_\pi^2 g_{NN\sigma} \left( A_\sigma + \frac{B_\sigma}{2M_W} \vec{\sigma}_1 \vec{q} \right) \frac{1}{\vec{q}^2 + m_\sigma^2}. \quad (4.12)$$

We can now try to establish the values of the weak couplings  $A_\sigma$  and  $B_\sigma$  by direct comparison to the results of the fits, and obtain information about  $A_\sigma$  using the numbers obtained in our LO (parity-conserving) result. Insight on  $B_\sigma$  would require a NLO fit, which, as we already mentioned, is not needed to reproduce reasonable well our observables.

The OSE gives contribution, in particular, to  $C_{00}$ , which now becomes:

$$C_{00}^{(\sigma)} = \left[ \frac{g_{\Lambda N K^*}^V}{m_{K^*}^2} \left( \frac{C_{K^*}^{PC,V}}{2} + D_{K^*}^{PC,V} \right) + \frac{g_{NN\omega}^V \alpha_\omega}{m_\omega^2} \right. \\ \left. - \frac{g_{\Lambda N K^*}^V C_{K^*}^{PC,V}}{m_{K^*}^2} - \frac{2 g_{NN\rho}^V \alpha_\rho}{m_\rho^2} - \frac{A_\sigma g_{NN\sigma}}{m_\sigma^2} \right] m_\pi^{-2}. \quad (4.13)$$

Since  $C_{01}$  is not modified by the inclusion of the  $\sigma$ , the minima that may be improved via this mechanism are the ones in which this coefficient is already in agreement with the one obtained from the OME expansion. Focusing on these minima (the ones with

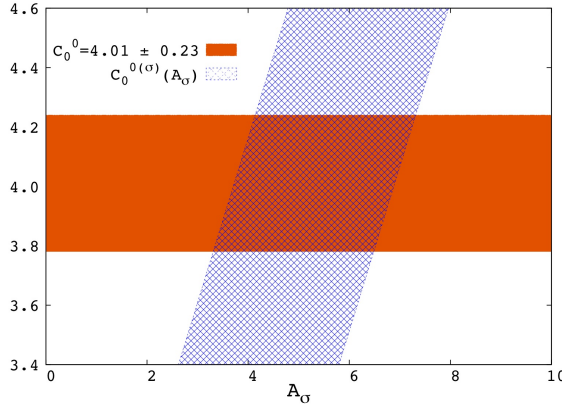


Figure 4.3: Comparison between  $C_{00}$  and  $C_{00}^{(\sigma)}$  for the Nijmegen minimum. The shaded (blue) area represents the dependence of  $C_{00}^{(\sigma)}$  on  $A_\sigma$  given by Eq. (4.13), while the fitted EFT  $C_{00}$  value is represented by the solid (orange) area. See text for details.

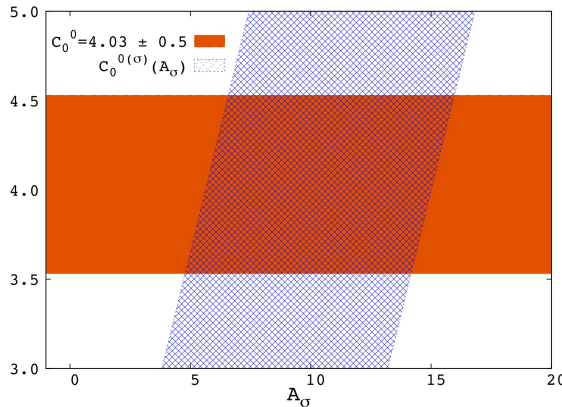


Figure 4.4: Same as Fig. 4.3 but for the Jülich minimum.

$\chi^2 = 13.43$  and  $\chi^2 = 4.26$ ), we can extract the value of  $A_\sigma$  needed to make the two formalisms agree (at LO) within each strong interaction model. Using  $m_\sigma = 550$  MeV and  $g_{NN\sigma} = 8.8$  [81] we get values for  $A_\sigma$  in the range  $3.3 \rightarrow 7.3$  for the Nijmegen minimum and in the range  $4.8 \rightarrow 16$  for the Jülich one.

The shaded (blue) band in Figs. 4.3 and 4.4 shows the value of  $C_{00}^{(\sigma)}$  given by Eq. (4.13) as a function of  $A_\sigma$ , when the Nijmegen or Jülich strong interaction model is used, respectively. Note that the error band in  $C_{00}^{(\sigma)}$  is given by the propagation of the uncertainties in the baryon-baryon-meson coupling constants, taken to be of the order of 30%. In the same plot we represent the corresponding fitted value in the EFT approach by a solid (orange) band. The range for  $A_\sigma$  quoted before corresponds to the intersection of both bands in the plot, *i.e.* the values for  $A_\sigma$  that make compatible the OME and EFT formalisms.

Other works have fitted this same parameter using different approaches. For instance, Ref. [110], which incorporates the OPE, OKE, and OSE mechanisms together with a direct-quark transition, uses the phenomenological approach of Block and Dalitz [111] to write the nonmesonic decay rates in terms of the squares of the amplitudes driving the  $\Lambda N \rightarrow NN$  transitions for the  $s$ -shell  ${}^5_\Lambda\text{He}$ ,  ${}^4_\Lambda\text{He}$ , and  ${}^4_\Lambda\text{H}$  hypernuclei. This factorization in terms of two-body amplitudes is possible when effective (spin-independent) correlations are used to account for the strong interaction among baryons, where no mixing between the different partial waves is possible. The strong interaction model used in this work is NSC97f. This approach leads to a quadratic equation to determine the couplings, resulting in two values for  $A_\sigma$ , 3.9 and  $-1.0$  (note that the first of these two values is compatible with the range we are quoting for this constant when the same strong interaction model is used). Another approach was followed in Ref. [74], where the exchanges of all the mesons belonging to the pseudoscalar and vector mesons octets are considered in the weak transition in addition to the  $\sigma$  meson, while again, effective (spin-independent) correlations are used in the strong sector. Fixing the value of the strong  $NN\sigma$  coupling to be the same as the  $NN\pi$  one, a range of variation for the  $\sigma$  mass and cutoff leads to different values for the weak couplings, once a fit to the nonmesonic decay rate and the neutron-to-proton ratio for  ${}^5_\Lambda\text{He}$  is performed. Even though the inclusion of the  $\sigma$ -exchange mechanism does modify their prediction for the intrinsic asymmetry, their results are insensitive to the particular values of the  $A_\sigma$  and  $B_\sigma$  couplings, and a simultaneous reproduction of all the data is not achieved.

## 4.4 The Hypertriton decay rate at leading order

As explained in Chapter 2, the observables of the weak decay of the hypertriton can be predicted in a less model-dependent way. This is because it is only made of three particles and both the initial and final wave functions can be computed using few-body techniques with the same strong interaction obtained from the same EFT. The downside, however, is the scarce experimental data for the decay of the hypertriton. As this calculation employs a different strong interaction kernel we would like to extract the corresponding LEC's by directly comparing to hypertriton decay data. Unfortunately, this is not the case and solely from the hypertriton decay data it is not possible to fit the LEC's. With this important experimental shortcoming what we do instead is to discuss how the total decay rate varies when we vary the LEC's within natural values. The total decay rate should, in principle, be comparable to the decay of the  $\Lambda$  in free space and to the decay of light hypernuclei.

The formalism needed to calculate the non-mesonic decay rate of the hypertriton has been derived in Sec. 2.2. There, the decay rate has been written in terms of the hypertriton wave function and the  $\Lambda N \rightarrow NN$  weak potential, which has been described in Chapter 3. We have distinguished between the two possible final nuclear products in which the hypertriton can decay: a deuteron and a neutron or three free nucleons. In the first case, the decay rate also depends on the deuteron wave function. The wave functions for the hypertriton and the deuteron used in our calculation have been calculated using NLO EFT YN and NN potentials [54].

The hypertriton wave function takes into account the strong couplings among the

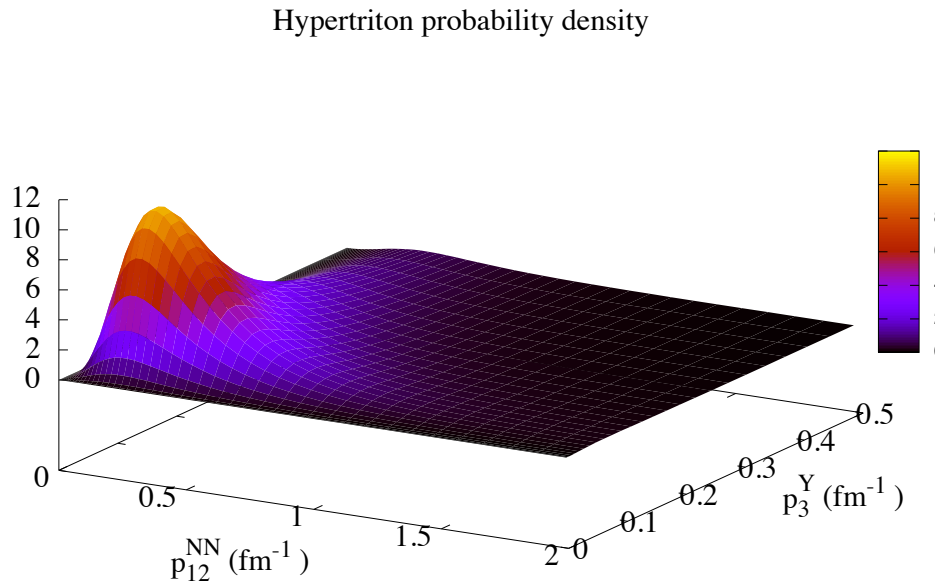


Figure 4.5: Momenta probability density for the hypertriton.  $p_3^Y$  corresponds to the momentum of the hyperon and  $p_{12}^{NN}$  to the relative momentum among the two nucleons.

Sigma contribution to the hypertriton probability density

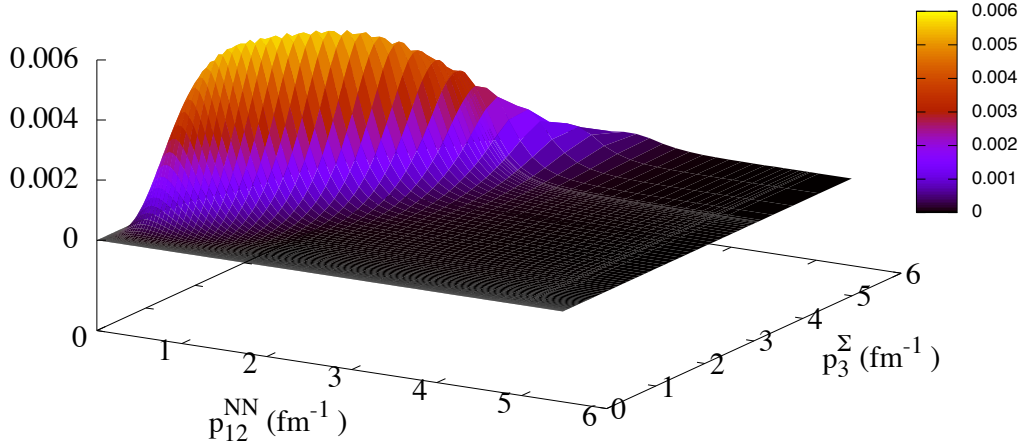


Figure 4.6: Contribution of the  $\Sigma$  hyperon to the momenta probability density for the hypertriton.  $p_3^\Sigma$  corresponds to the momentum of the  $\Sigma$  and  $p_{12}^{NN}$  to the relative momentum among the two nucleons.

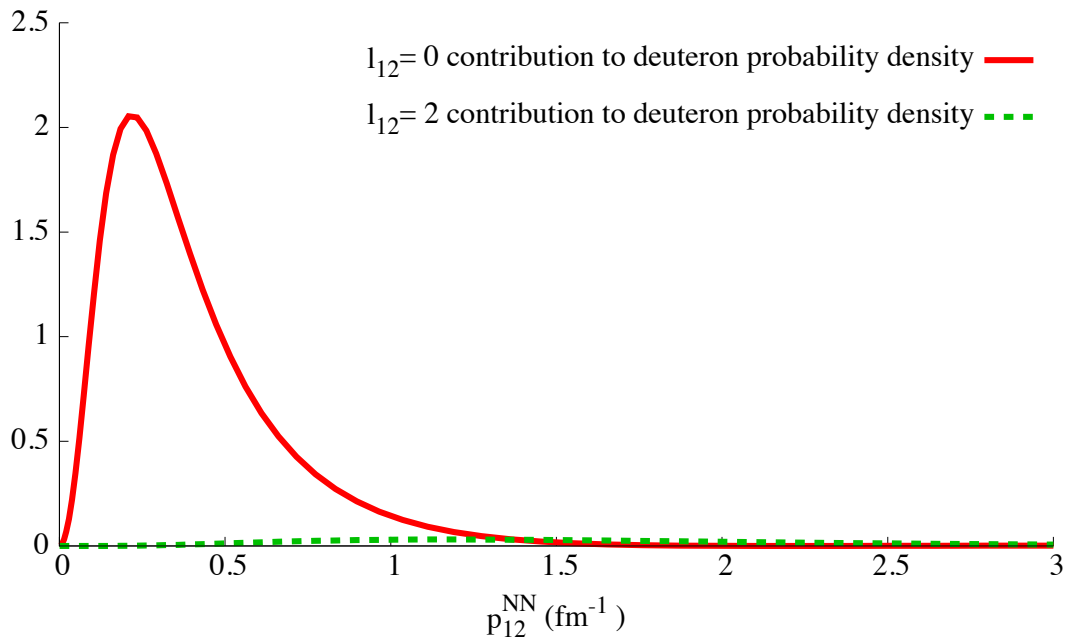


Figure 4.7: Contributions  $l_{12} = 0$  and  $l_{12} = 2$  to the momenta probability density for the deuteron. The deuteron is mainly an  $l_{12} = 0$  state.

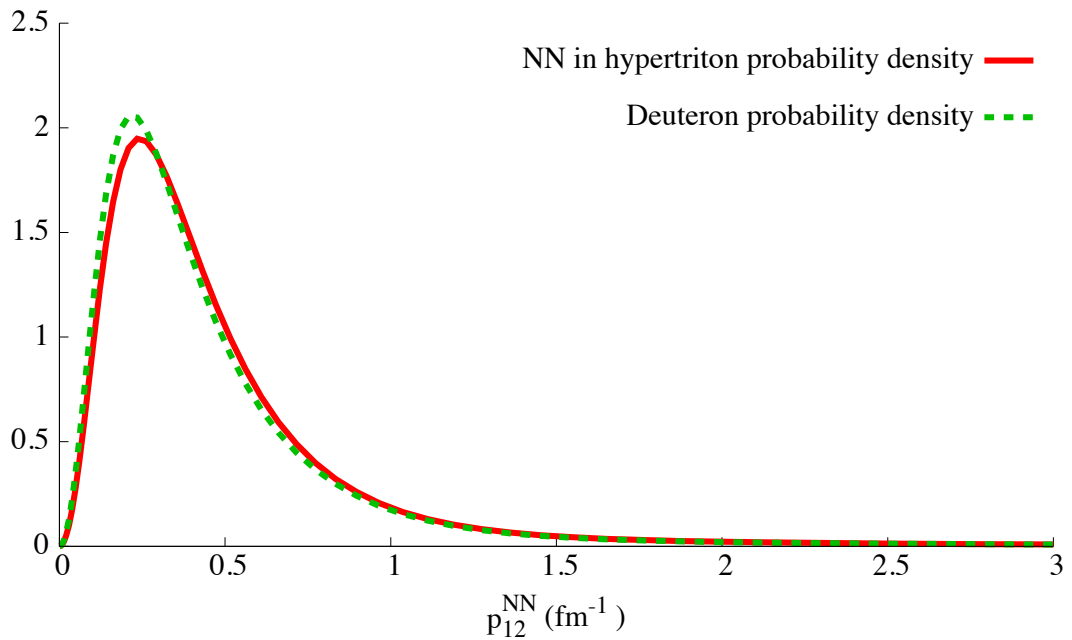


Figure 4.8:  $p_{12}$  probability density for the two nucleons in the hypertriton and for the two nucleons in the deuteron. The similarity of the two densities reflects the fact that the hypertriton is mainly a deuteron with a low bounded  $\Lambda$ .

different baryonic channels,  $\Lambda N - \Sigma N$ . Hence, both hyperons, the  $\Lambda$  and the  $\Sigma$ , contribute to the wave function. In order to illustrate what are the typical momenta of the baryons forming the hypertriton we show, in Fig. 4.5, the probability density distribution of their momenta. In Fig. 4.5  $p_{12}^{NN}$  represents the relative momenta of the two nucleons and  $p_3^Y$  the spectator momenta of the hyperon, which may be a  $\Lambda$  or a  $\Sigma$ . The first thing which we observe is that the contribution of the  $\Sigma$  hyperon to the hypertriton momenta distribution is much smaller than the one of the  $\Lambda$ , and cannot be appreciated in Fig. 4.5. The momenta distribution for the  $\Sigma$  is plotted in a different scale in Fig. 4.6.

Two features can be easily distinguished between the two figures. On the one hand, the momentum distribution for the  $\Lambda$  is peaked at values very close to zero, of the order of  $p_3^\Lambda \sim 0.1 \text{ fm}^{-1}$ , while the  $\Sigma$  distribution is peaked at  $p_3^\Sigma \sim 2 \text{ fm}^{-1}$ . On the other hand, the probability density for  $p_3^\Sigma$  is much more spread than the one for  $p_3^\Lambda$ . These two features can be associated to the  $\Sigma$  having a larger mass than the  $\Lambda$ . A heavier baryon is expected to contribute less to the wave function but with a larger momentum.

The deuteron has zero isospin and positive parity and can be in two angular states,  $l_{12} = 0$  or  $l_{12} = 2$ . In Fig. 4.7 we show the momentum distribution of the deuteron for each of these two channels. As it can be easily seen in the figure, the main contribution to the wave function comes from the  $l_{12} = 0$  channel. It is also interesting to compare the probability density of the relative momentum among the nucleons in the deuteron and in the hypertriton. This comparison is shown in Fig. 4.8. The similarity of both distributions, as it can be appreciated in the figure, reflects the fact that the  $\Lambda$  is much less bound than the nucleons forming the hypertriton. The lightest hypernucleus can thus be regarded as a loosely bound-state of a deuteron and  $\Lambda$  hyperon. The latter orbiting the deuteron with a very small momentum.

In Table 4.5, we show the values we obtain for the total decay rates of the hypertriton, taking into account only the one-pion exchange, and the one-pion and the one-kaon exchanges. These values show a clear dominance of the  $3N$  break up in front of the decay to a deuteron and a neutron. It can also be seen that the pion and the kaon interfere destructively, reducing the total decay rate when both one-meson exchanges are included. This destructive interference comes from the strong baryon-baryon-meson couplings, which have opposite signs for the pion and the kaon, or more precisely,  $g_{\Lambda NK} = -14.1$  and  $g_{NN\pi} = 13.16$ .

	$\Gamma_{d+n} (s^{-1})$	$\Gamma_{3N} (s^{-1})$
$\pi$	$0.54 \cdot 10^7$	$0.57 \cdot 10^8$
$\pi+K$	$0.15 \cdot 10^7$	$0.18 \cdot 10^8$

Table 4.5: Values for the total decay rates of the hypertriton including the one pion exchange and both, the one pion and one-kaon exchanges.

In Figs. 4.9 and 4.10, the total decay rate for both channels,  $3N$  and  $d+n$ , and including the one-pion and one-kaon exchange mechanisms, is plotted as a function of the two low-energy constants,  $C_{00}$  and  $C_{01}$ . Both figures show that, by varying the two low-energy constants within a small range, from  $-1$  to  $1$ , the total decay rates are quantitatively quite affected. Moreover, the two contact operational structures interfere constructively

when they have opposite signs, giving thus a much larger decay rate, and destructively when both LEC's have the same sign.

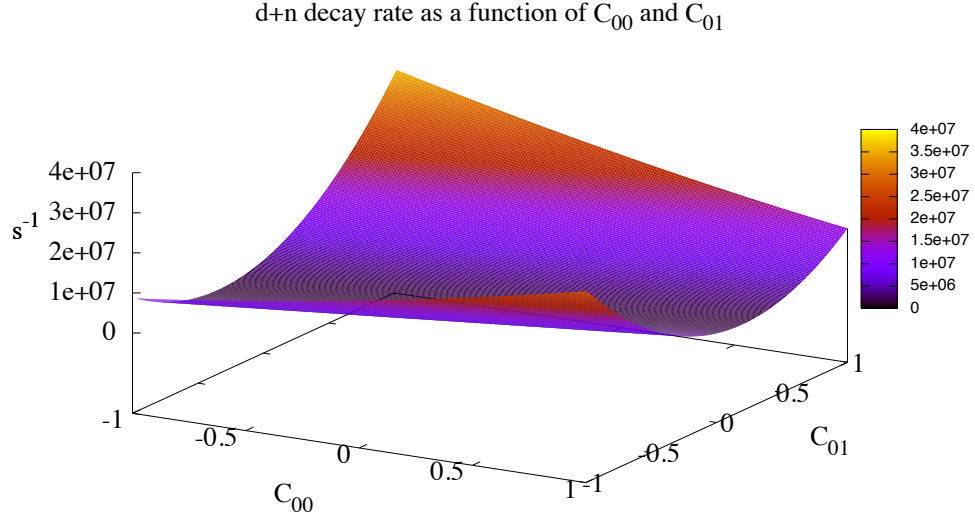


Figure 4.9: Hypertriton total decay rate for the deuteron plus nucleon channel, including the one-pion and one-kaon exchange mechanisms and as a function of the two low-energy constants  $C_{00}$  and  $C_{01}$ .

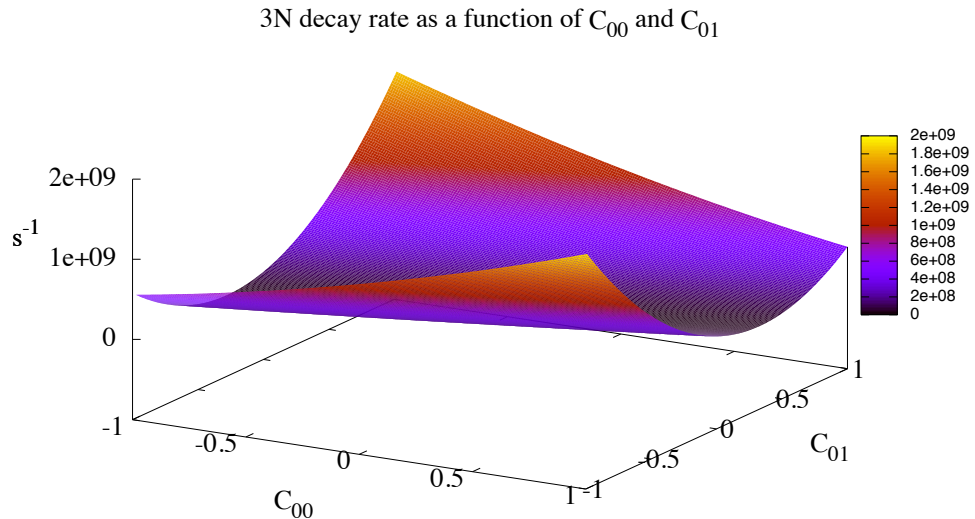


Figure 4.10: Hypertriton total decay rate for the deuteron plus nucleon channel, including the one-pion and one-kaon exchange mechanisms and as a function of the two low-energy constants  $C_{00}$  and  $C_{01}$ .

The study of the decay of the hypertriton has been carried out previously in [112]. The authors of this work computed the decay by using one-meson-exchange potentials from

the Nijmegen group in both, the weak and strong interactions. The values for the total decay rates listed in their work agree with ours, both from a quantitative and qualitative point of view. In particular, we confirm their prediction that the total decay rate of the hypertriton into a deuteron and a neutron is one order of magnitude smaller than the total decay rate for the  $3N$  break up.

## 4.5 Comparison of LO and NLO contributions

In this last section we briefly analyze the two-pion exchange potentials described in Sec. 3.4.2 while comparing them to the one-pion and one-kaon exchanges LO potentials. In Eqs. (3.28)-(3.36) and (3.39)-(3.47) we provided the explicit momentum and spin structures arising from the different Feynman diagrams. Some features can be easily read off from the different terms. First, the ball (a) and first two triangle diagrams (b,c) only contribute to the parity conserving part of the transition potential. Most other diagrams have a non-trivial contribution, involving all allowed momenta and spin structures.

To provide a sample of the contribution of the different diagrams to the full amplitude, we illustrate the case of the triplet central transition,  ${}^3S_1 \rightarrow {}^3S_1$ . In particular, we compare the  $\pi$  and  $K$  exchanges with the ball, triangle and box diagrams for the  $\Lambda n \rightarrow nn$  channel. Since the interaction is parity conserving, none of the parity violating structures of Table 3.1 contribute. For structures of the type  $(\vec{\sigma}_1 \cdot \vec{q})(\vec{\sigma}_2 \cdot \vec{q})$  we have that

$$(\vec{\sigma}_1 \cdot \vec{q})(\vec{\sigma}_2 \cdot \vec{q}) = \frac{\vec{q}^2}{3}(\vec{\sigma}_1 \cdot \vec{\sigma}_2) + \frac{\vec{q}^2}{3}\hat{S}_{12}(\hat{q}), \quad (4.14)$$

where the tensor operator  $\hat{S}_{12}(\hat{q})$  changes either zero or two units of angular momentum and does not contribute to this transition (see its definition and matrix elements in App. A). The potential, therefore, depends only on the modulus of the momentum (or  $\vec{q}^2$ ). To obtain the potential in position space we Fourier-transform the expressions for the one-meson-exchange contributions, Eqs. (3.18) and (3.19), and the loop expressions in the appendices D.2, D.3 and D.4. More explicitly, we compute the following,

$$\tilde{V}(r) = \mathcal{F}[V(\vec{q}^2)F(\vec{q}^2)] \equiv \int_{-\infty}^{\infty} \frac{d^3q}{(2\pi)^3} e^{i\vec{q} \cdot \vec{r}} V(\vec{q}^2) F(\vec{q}^2)$$

with  $q \equiv |\vec{q}|$  and  $r \equiv |\vec{r}|$  and where we have included a form factor in order to regularize the potential. Following the formalism developed in Ref. [17] we use a monopole form factor for the meson exchange contribution at each vertex, while the  $2 - \pi$  terms use a Gaussian form of the type  $F(\vec{q}^2) = e^{-\vec{q}^4/\Lambda^4}$ .

The expressions for each loop integral, shown in App. D, have been calculated using dimensional regularization. Details of this calculation are given in App. E, where the integrals are written in terms of the couplings appearing in Chapter 3 and of some master integrals.  $\eta$  is the regularization parameter that appears when integrating in  $D \equiv 4 - \eta$  dimensions. The modified minimal subtraction scheme ( $\overline{MS}$ ) has been used—we have expanded in powers of  $\eta$  the expressions for the different loop contributions and then subtracted the term  $R \equiv -\frac{2}{\eta} + \gamma - 1 - \ln(4\pi)$ .

In Fig. 4.11, we show the respective contributions to the potential in position space. The one-pion-exchange potential is repulsive while the one kaon-exchange one is attractive.

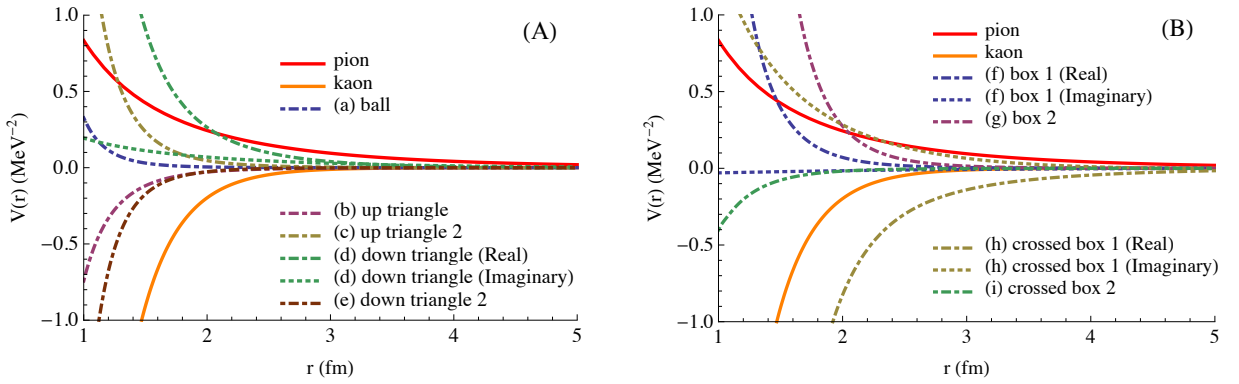


Figure 4.11: (A) Medium-Long range part of the potentials for the one-pion-exchange, one-kaon-exchange, ball diagram and triangle diagrams. (B) Medium-Long range part of the potentials for the one-pion-exchange, one-kaon-exchange, box and crossed box diagrams.

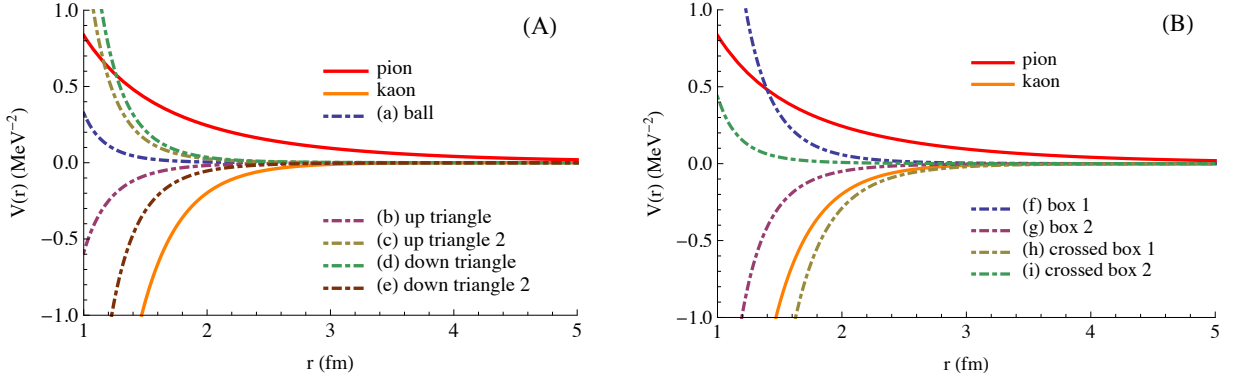


Figure 4.12: (A) Medium-Long range part of the potentials in the SU(3) limit for the one-pion-exchange, one-kaon-exchange, ball diagram and triangle diagrams. (B) Medium-Long range part of the potentials in the SU(3) limit for the one-pion-exchange, one-kaon-exchange, box and crossed box diagrams.

This destructive interference does not depend on the weak coupling constants accompanying the different isospin and spin structures, but on the global strong baryon-baryon-meson couplings, as commented in the previous section. The contribution from the different  $2-\pi$  exchange potentials are seen to be sizable at all distances. The triangles (b) and (e) and the crossed box diagrams (h) and (i) are attractive and hence interfere destructively with the pion, while all the others are repulsive and interact constructively. The largest contributions come from the box (f, g, h) and triangle (d) diagrams, which are comparable to the pion and the kaon. Note that diagrams (d), (f) and (h) contribute with an imaginary part. This is characteristic of diagrams with a  $\Lambda N\pi$  vertex, which may be on shell since  $M_\Lambda > M_N + m_\pi$ . This imaginary part is taking into account the amplitude for the possible  $\Lambda N \rightarrow NN\pi$  transition. We stress that the imaginary part of the box diagram (f) that comes from the baryonic pole has been extracted, so no iterated part is considered in Fig. 4.11.

Fig. 4.12, shows the same potentials but taking  $q_0 = q'_0 = 0$ . In this limit, the baryon

mass differences are neglected and the vertices  $\Lambda N\pi$  cannot be on shell anymore. Therefore, all the imaginary parts disappear. All diagrams seem to have a smaller contribution with this approximation. The attractive and repulsive character of the different potentials does not change except for the second box diagram and the (very short-ranged) second crossed box diagram, which turn to be attractive and repulsive, respectively, when taking the SU(3) limit.

The  $2 - \pi$  loop diagrams play an important role due to the different interferences among them and among the one-meson-exchange contributions.



# Chapter 5

## Summary and future perspectives

In this thesis we have developed an effective field theory description to understand in a fundamental and systematic way the weak decay of hypernuclei. This decay, as elaborated in the thesis and in previous works, is an extremely rich process. It involves several ingredients which range from a precise understanding of the strong interactions between low-lying hadrons, to a proper description of the weak coupling mechanisms which trigger the decay of the hypernuclei. Notably, hypernuclei are routinely produced nowadays in a number of facilities around the world and their decay products can be measured with good accuracy. This makes these systems a nice laboratory to study the physics of the weak interaction among the baryons.

We have concentrated on the less-known pieces in the description of the weak hypernuclear decay, the weak decay mechanisms. In particular we have studied the  $\Lambda N \rightarrow NN$  transition mechanism, which is the main responsible for the decay of medium mass heavier hypernuclei. The reason is that the nominal decay of the  $\Lambda$  in free space, which is to decay into a nucleon and a pion, is forbidden for large enough nuclei. This is because the final nucleon does not have enough momentum to either escape the nucleus or occupy energy levels above the Fermi momentum. This weak transition amplitude has been studied before using one-meson-exchange models [16, 17, 18] and a combination of one-pion-exchange and quark degrees of freedom to account for the short range part of the interaction [27]. Within these models the resulting amplitude, embedded in the proper many-body theory to account for the nuclear structure of the initial hypernuclei and final decay products, allowed one to get a good phenomenological understanding of the weak mechanism, and a good reproduction of the decay observables measured by the experimentalists [113]. This success triggered us to go one step further and develop an effective field theory description of the weak process.

The formal development of the effective field theory (EFT) for the  $\Lambda N \rightarrow NN$  is the main result of this thesis. To develop such a theory is essential in order to have a firm understanding of the problem from the theoretical point of view. It provides a less model-dependent description of the decay process and allows to systematically improve the predictions of the theory. EFTs are built based on a significant separation of scales in the physical problem under study and on the existence of a small parameter, built from the ratio of two of those scales, which is used to define an expansion. In the case of  $NN$  scattering at very low energies, where EFTs have been developed in the last decay with

extremely successful results, this parameter is the momentum exchanged between the two nucleons. In our case, the two nucleons in the final state carry a non-negligible momentum as a consequence of the different mass between the  $\Lambda$  hyperon and the nucleon in the initial state, therefore, it is more convenient to think on the ratio of the final momentum over the typical mass as an expansion parameter.

With both the leading order and next-to-leading-order of the theory computed, we have turned our sight into the experimental data available. Due to the few available data existing for non-mesonic hypernuclear decay we have decided to concentrate on the leading order piece of the transition amplitude. This piece has been employed to compute the decay observables for light nuclei,  $^5_\Lambda\text{He}$ ,  $^{11}_\Lambda\text{B}$  and  $^{12}_\Lambda\text{C}$ , and for the smallest known hypernucleus, the hypertriton. To get the detail of how the whole procedure has been pursued let us in the following provide a brief rendition of the results presented in Chapters 2, 3, and 4.

## **Chapter 2. Hypernuclear decay formalism**

In this Chapter we introduced the formalism and detailed the wave functions used to compute the hypernuclear decay observables. We considered two different approaches. The first one was the decay of hypernuclei for which a full microscopic description is not feasible, due to the complexity in numerically solving the many-body problem in an exact way. These are  $^5_\Lambda\text{He}$ ,  $^{11}_\Lambda\text{B}$  and  $^{12}_\Lambda\text{C}$ . The initial wave function describing the hypernuclei was obtained by means of a shell model with a mean-field harmonic oscillator potential. The parameters in the single-particle wave functions were chosen such that the binding energies of the  $A$  hypernuclei and its  $A - 1$  core nucleus were correctly reproduced. The decay products, i.e. a residual nucleus and two nucleons, are treated in the following way. The residual nucleus acts as an spectator, and the corresponding nuclear structure details are not relevant for the calculation. In order to account for the short range physics stemming from the strong interaction among baryons, realistic NN potentials have been used to obtain a correlated wave function for the final NN system though the solution of a scattering T-matrix equation. With respect to the strong interaction acting on the initial hyperon-nucleon pair, we have chosen to use a phenomenological correlation function that simulates the effects of performing a much more involved G-matrix calculation.

In the second approach we study the weak decay of the hypertriton. This hypernucleus is fairly small, it is made of only two nucleons and a  $\Lambda$  particle, and an exact treatment of the few-body problem is feasible in terms of Faddeev-Yakubovsky equations. Interestingly, we can study exactly two important decay modes of the hypertriton, the decay into a deuteron and a nucleon and the decay into three nucleons.

## **Chapter 3. EFT description for the $\Lambda N \rightarrow NN$ interaction**

In Chapter 3 we presented the effective field theory description of the weak decay amplitude. The EFT is built in the following way. First we note that due to the mass difference between the  $\Lambda$  and the nucleon, the outgoing nucleons have a nonzero minimum value of their momentum. This feature forces us to explicitly take into account the low-lying mesonic degrees of freedom, and develop the EFT to describe the smaller distances. The

---

latter are usually accounted for in one-meson-exchange models by the exchange of heavier mesons, e.g.  $\rho$ ,  $\omega$ , etc.

Thus, we describe the weak amplitude by means of explicit one pion/kaon exchange contributions plus contact terms entering at different orders in the transferred momentum. The vertexes entering the one pion/kaon exchanges are all either known experimentally or derived from SU(3) symmetry. The leading order (LO) contribution to the EFT is readily written down by noting the possible momentum-spin-isospin structures which are compatible with the existing symmetries. This LO contribution has solely two low energy constants.

The virtue of the EFT description is that, within the appropriate bounds for the small parameter used to define the theory, one can further investigate the contributions of the next-to-leading order and higher terms. In this chapter we have derived the full next-to-leading contribution to the amplitude. First, the next-to-leading contact interactions are written down, and secondly, we computed all two-pion exchange diagrams. All details entering the computation of these diagrams, grouped by their topology as balls, triangles and squares, are provided in the Appendices D and E. They do contribute to all possible spin-isospin-momentum structures and thus their effect should be taken into account in future studies. Let us remark that the next-to-leading description includes 15 low energy constants (two of them already present at LO).

## Chapter 4. Results

Chapter 4 compares the predictions of the EFT derived in the previous chapter, in combination with the formalism employed to compute the hypernuclear decay observables as derived in Chapter 2, to the existing experimental data. The world database of the non-mesonic weak decay observables is notably meager. There are just a handful of observables measured with good prediction which we can aim at describing with our theory. This scarcity of data led us to consider only the leading order contribution to the  $\Lambda N \rightarrow NN$  decay amplitude. This order only contains two independent parameters which we are able to constraint by means of a minimization routine. A fit to the total and partial decay rates and the final proton asymmetry for these hypernuclei has been done, which allowed us to constrain the values of the two low-energy constants entering at LO. The obtained LO potential provides a description of the existing data within errorbars. Unfortunately, the low-energy constants found show a noticeable dependence on the strong baryon-baryon interaction model used to fix the parameters entering the one-pion and one-kaon exchange mechanisms. To shed further light into the problem we compare the low-energy constants with the one-meson-exchange potentials widely used and tested in the literature. This is done by expanding the one-meson-exchange potentials in powers of the transferred momentum and matching both the EFT and the OME model order by order. In this way we were able to discuss the presence of a sizable scalar exchange contribution to the amplitude, which had been previously proposed [114].

Then we turned into the calculation of the hypertriton decay. As mentioned above all strong interaction ingredients for this calculation were obtained consistently. In this case, we gave the result for the decay of the hypertriton into three uncorrelated nucleons and into a nucleon and a deuteron within the partial-wave impulse approximation.

Finally, we have presented an academic comparison between the contributions coming from the next-to-leading order two-pion exchange diagrams and the ones coming from the leading one-meson exchange diagrams. As we do not have enough data to constrain all the LECs appearing at NLO, we have decided to show the contribution of the two-pion exchange diagrams with arbitrary natural values for the low energy constants. The contribution of the two-pion exchange terms have been found to be comparable in size to those arising from the one-pion and one-kaon exchange terms.

## 5.1 Future Perspectives

### Two nucleon induced decay mechanism

As mentioned above, an appealing feature of the EFT framework is that, once settled, it can be applied to other regimes and reactions. A notable example is the  $\Lambda NN \rightarrow NNN$  mechanism. This two nucleon induced decay mechanism, has recently been shown by the FINUDA collaboration to be responsible for one fifth of the total non-mesonic decay,  $\Gamma_{2N}/\Gamma_{nm} = 0.21 \pm 0.07^{+0.03sys}_{-0.02sys}$  [115]. Thus, we hope we can in the near future evaluate this mechanism within our EFT and be able to use this data to further constrain the theory.

### Weak decay of $A = 4$ hypernuclei

Our EFT for the  $\Lambda N \rightarrow NN$  transition can also be implemented in other hypernuclei other than the hypertriton, as for example the  $A = 4$   ${}^4_\Lambda H$  and  ${}^4_\Lambda He$  systems. The next would be  $A = 4$  hypernuclei, namely  ${}^4_\Lambda H$  and  ${}^4_\Lambda He$ . To perform a similar study to the one presented in this thesis for the hypertriton, one would need to use the Faddeev-Yakubovsky scheme for four baryons. This framework was already developed a decade ago, and was used to compute the wave functions for these hypernuclei [62]. These calculations would provide more accurate (in the sense of employing an exact description of the four-body problem) results as compared to the ones that can be obtained using a shell-model prescription. In addition, it has been shown [116] that these systems are more useful than others s-shell nuclei to test the validity of the  $\Delta I = \frac{1}{2}$  rule, which makes the calculation of their decay rates even more interesting.

In order to achieve a more complete description of the decay of  ${}^3_\Lambda H$ ,  ${}^4_\Lambda H$  and  ${}^4_\Lambda He$ , the mesonic decay rates should also be computed. This can in principle be done using the phenomenological amplitude for the weak process,  $\Lambda \rightarrow N\pi$ , combined with the strong EFT potentials. The latter could consistently be employed to account for initial and final correlations due to the strong force. In this manner, we would provide a full description of all the decay modes for these light hypernuclei. It is worth stressing that experimental information of the total and partial decay rates of these three hypernuclei would be of great value, and we hope that the future E22 experiment at J-PARC would definitely give us accurate numbers for these observables.

## Weak decay of double $\Lambda$ hypernuclei

Another research avenue which is worth exploring within a similar framework is the EFT description of the weak decay of double- $\Lambda$  hypernuclei. In this case new decay channels involving octet baryons other than the  $\Lambda$  appear, thus providing more insight into the weak interaction. Namely, each of the two  $\Lambda$ 's can decay mesonically, but also through non-mesonic channels, which now include apart from the standard  $\Lambda N \rightarrow NN$  mode, new  $\Lambda\Lambda \rightarrow YN$  reactions, where  $Y$  can be either a  $\Lambda$  or a  $\Sigma$  hyperon.

## Other sources of information on the weak $|\Delta S| = 1$ interaction

As mentioned several times in this thesis, in order to constrain the EFT at NLO, more and accurate experimental input is needed. The data constraining the weak  $\Delta S = 1$  interaction is mainly obtained through the accurate measurement of hypernuclear decay observables, which are the experiments we have discussed. We again emphasize on the need of data for light hypernuclear systems. A different way to obtain this information would be through the measurement of the inverse reaction in free space,  $np \rightarrow \Lambda p$ , which would give us a clean extraction of the observables. Unfortunately, the values of the cross sections for the weak strangeness production mechanism, of the order of  $10^{-12}$  mb, is very small [6, 7, 8]. This has prevented, for the time being, its consideration as part of the experimental data set, despite the effort invested in extracting different polarization observables for this process in the past [9, 10]. In the near future we hope there will be advances along this line.

Finally, let us comment on a promising and important tool we have to obtain information about these hadronic interactions. This is lattice quantum chromodynamics (LQCD). There are already proposals to obtain useful information on the description of weak baryonic processes from LQCD in the strange sector [53]. For instance, the mesonic and nonmesonic decays of hyperons can in principle be studied in the lattice. The former could help to understand why the lowest order effective Lagrangians are unable to simultaneously reproduce the parity-conserving and parity-violating amplitudes for the mesonic decay of hyperons. The latter would provide clean information on the weak  $|\Delta S| = 1$  four-fermion interaction. In contrast to the study of the nonmesonic decay in hypernuclei, LQCD has the great advantage to study the interaction without the contamination due to the presence of the nuclear medium. However, computing weak baryonic processes with LQCD represents a great challenge, specially from the computationally point of view, and constitutes an avenue that is still in a very preliminary stage. Up to now, only [42] has performed a calculation of weak baryon-baryon matrix elements in the lattice, with the computation of the leading-order momentum-independent parity-violating coupling between pions and nucleons. Although there are some ingredients that have been disregarded in this calculation—basically to make the computation feasible—as disconnected (quark-loop) diagrams, it represents an encouraging step forward the use of LQCD as a reliable alternative to investigate physical processes poorly constrained by experiments.



# Appendix A

## Spin matrix elements in position space

In this appendix we show the matrix elements for the operators appearing in the leading order potential for the  $\Lambda N \rightarrow NN$  transition. We define the matrix elements of an operator  $O_\alpha$  in position space, between an initial pair of baryons with spin and angular momentum  $l$  and  $s$ , and a final one with spin and angular momentum  $l'$  and  $s'$  as

$$\langle(l', s')j | \mathcal{O}_\alpha | (l, s)j \rangle \equiv \int d\hat{r} \int d\hat{r}' \langle(l' s')jm_j | \hat{r}' \rangle O_\alpha \langle \hat{r} | (ls)jm_j \rangle. \quad (\text{A.1})$$

The total spin and its projection are denoted  $j$  and  $m_j$  and both are conserved quantities.

### A.1 Central spin-independent transition ( $\hat{1}$ )

$$\langle(l' s')j | 1 | (ls)j \rangle = \delta_{ss'} \delta_{ll'} \quad (\text{A.2})$$

### A.2 Spin-spin transition ( $\vec{\sigma}_1 \cdot \vec{\sigma}_2$ )

$$\langle(l' s')j | (\vec{\sigma}_1 \cdot \vec{\sigma}_2) | (ls)j \rangle = [2s(s+1) - 3] \delta_{ss'} \delta_{ll'} \quad (\text{A.3})$$

### A.3 Parity-violating transition ( $\vec{\sigma}_1 \cdot \hat{r}$ )

$$\begin{aligned} \langle(l' s')j | (\vec{\sigma}_1 \cdot \hat{r}) | (ls)j \rangle &= (-1)^{1+j-l'+s+s'} \sqrt{6} \sqrt{(2l+1)(2s'+1)(2s+1)} C_{10l0}^{l'0} \\ &\times \left\{ \begin{array}{ccc} \frac{1}{2} & \frac{1}{2} & s \\ s' & 1 & \frac{1}{2} \end{array} \right\} \left\{ \begin{array}{ccc} l' & l & 1 \\ s & s' & j \end{array} \right\} \end{aligned} \quad (\text{A.4})$$

The matrix element for the operator  $\vec{\sigma}_2 \cdot \hat{r}$  gives the same result but for a factor  $(-1)^{s+s'}$ .

## A.4 Tensor transition $3(\vec{\sigma}_1 \cdot \hat{r})(\vec{\sigma}_2 \cdot \hat{r}) - (\vec{\sigma}_1 \cdot \vec{\sigma}_2)$

$$\langle (l's')j | 3(\vec{\sigma}_1 \cdot \hat{r})(\vec{\sigma}_2 \cdot \hat{r}) - (\vec{\sigma}_1 \cdot \vec{\sigma}_2) | (ls)j \rangle = \delta_{ss'}\delta_{s1}S_{ll'}^j, \quad (\text{A.5})$$

where  $S_{ll'}^j$  is defined in Table A.1.

$S_{ll'}^j$	$l' = j + 1$	$l' = j$	$l' = j - 1$
$l = j + 1$	$-\frac{2(j+2)}{2j+1}$	0	$\frac{6\sqrt{j(j+1)}}{2j+1}$
$l = j$	0	2	0
$l = j - 1$	$\frac{6\sqrt{j(j+1)}}{2j+1}$	0	$\frac{2-2j}{2j+1}$

Table A.1: Values of  $S_{ll'}^j$

## Appendix B

# Spin matrix elements in momentum space

In the following sections the matrix elements for the operators in momentum space appearing in the leading order potential for the  $\Lambda N \rightarrow NN$  transition are shown. The quantum numbers are defined as in the previous appendix. The general expression for these matrix elements is

$$\langle j, (l', s') | \mathcal{O}_\alpha | j, (l, s) \rangle \equiv \int d\hat{p} \int d\hat{p}' \langle (l' s') jm_j | \hat{p}' \rangle f(q) O_\alpha \langle \hat{p} | (ls) jm_j \rangle, \quad (\text{B.1})$$

where  $p$  and  $p'$  are the modulus of the initial and final momenta,  $\vec{p}$  and  $\vec{p}'$ , and  $f(q)$  denotes a general function dependent on the modulus of the momentum difference  $q \equiv |\vec{p}' - \vec{p}|$ . We also define the angle between  $\vec{p}'$  and  $\vec{p}$  as  $\hat{q}$ , and its cosine as  $x$ . The matrix elements will depend on the Legendre polynomials, which we denote as  $P_l$ . The matrices  $\sigma$  appearing in the operators are the Pauli matrices, defined as following,

$$\sigma_1 = \begin{pmatrix} 0 & 1 \\ 1 & 0 \end{pmatrix}, \quad \sigma_2 = \begin{pmatrix} 0 & -i \\ i & 0 \end{pmatrix}, \quad \sigma_3 = \begin{pmatrix} 1 & 0 \\ 0 & -1 \end{pmatrix}. \quad (\text{B.2})$$

### B.1 Central spin-independent transition ( $\hat{1}$ )

$$\langle p'(l' s') jm | f(q) | p(ls) jm \rangle = \delta_{ss'} \delta_{ll'} (2\pi) g_l(\hat{q}), \quad (\text{B.3})$$

with

$$g_l(\vec{q}) \equiv \int_{-1}^1 dx' P_l(x') f(q). \quad (\text{B.4})$$

### B.2 Central spin dependent transition ( $(\vec{\sigma}_1 \cdot \vec{\sigma}_2)$ )

$$\langle p'(l' s') jm | f(q) (\vec{\sigma}_1 \cdot \vec{\sigma}_2) | p(ls) jm \rangle = 2\pi(2s(s+1) - 3) g_l(q) \delta_{ss'} \delta_{ll'}, \quad (\text{B.5})$$

with

$$g_l(\vec{q}) \equiv \int_{-1}^1 dx' P_l(x') f(q). \quad (\text{B.6})$$

### B.3 Parity violating transition ( $\vec{\sigma}_2 \cdot \vec{q}$ )

$$\begin{aligned} \langle p'(l's')jm|f(q)(\vec{\sigma}_2 \cdot \vec{q})|p'(l's')jm\rangle &= -36\sqrt{6}\pi\sqrt{\hat{s}\hat{s}'\hat{j}} \left\{ \begin{array}{ccc} l' & l & 1 \\ s' & s & 1 \\ j & j & 0 \end{array} \right\} \left\{ \begin{array}{ccc} \frac{1}{2} & \frac{1}{2} & 0 \\ \frac{1}{2} & \frac{1}{2} & 1 \\ s' & s & 1 \end{array} \right\} \\ &\times \sum_k \sum_{\lambda_1+\lambda_2=1} (-1)^{k+l} \hat{k}^{\frac{3}{2}} g_k(q) \sqrt{\frac{\hat{\lambda}_1 \hat{\lambda}_2}{\hat{\lambda}_1! \hat{\lambda}_2!}} (p')^{\lambda_1} (-p)^{\lambda_2} \\ &\times (k\lambda_1 l', 000)(k\lambda_2 l, 000) \left\{ \begin{array}{ccc} k & k & 0 \\ \lambda_1 & \lambda_2 & 1 \\ l' & l & 1 \end{array} \right\}, \end{aligned}$$

with

$$g_k(\vec{q}) \equiv \int_{-1}^1 dx' P_k(x') f(q).$$

The matrix element for the operator  $(\vec{\sigma}_1 \cdot \vec{q})$ , instead of the  $(\vec{\sigma}_2 \cdot \vec{q})$  one, is the same except for a factor of  $(-1)^{s+s'}$ .

### B.4 Tensor transition operator ( $\vec{\sigma}_1 \cdot \vec{q})(\vec{\sigma}_2 \cdot \vec{q})$ )

$$\begin{aligned} \langle p'(l's')j'm'|f(q)(\vec{\sigma}_1 \cdot \vec{q})(\vec{\sigma}_2 \cdot \vec{q})|p(ls)jm\rangle &= 36\pi\delta_{jj'}\delta_{mm'} \sum_f \sum_{\lambda_1+\lambda_2=f} \sum_k (-1)^{k+l} \\ &\times \hat{k}^{\frac{3}{2}} \hat{f}^2 \hat{s} \sqrt{\hat{j}} \sqrt{\frac{\hat{f}!}{(2\lambda_1)!(2\lambda_2)!}} g_k^f(\hat{q}) (p')^{\lambda_1} (-\hat{p})^{\lambda_2} \\ &\times (11f, 000)(k\lambda_1 l', 000)(k\lambda_2 l, 000) \\ &\times \left\{ \begin{array}{ccc} 1 & 1 & 0 \\ 1 & 1 & 0 \\ f & f & 0 \end{array} \right\} \left\{ \begin{array}{ccc} l' & l & f \\ s & s & f \\ j & j & 0 \end{array} \right\} \\ &\times \left\{ \begin{array}{ccc} \frac{1}{2} & \frac{1}{2} & 1 \\ \frac{1}{2} & \frac{1}{2} & 1 \\ s & s & f \end{array} \right\} \left\{ \begin{array}{ccc} k & k & 0 \\ \lambda_1 & \lambda_2 & f \\ l' & l & f \end{array} \right\}, \end{aligned}$$

with

$$g_k^f(\vec{q}) \equiv \int_{-1}^1 dx' P_k(x') f(q) \vec{q}^{2-f}.$$

# Appendix C

## Isospin matrix elements

In order to use the isospin formalism we couple an isospin  $I = \frac{1}{2}$  to the hyperons. This is the way to implement the  $\Delta I = \frac{1}{2}$  rule to the weak interactions (see Sec. 2.1.3). Thus, the  $\Lambda$  behaves as a hyperon with  $I = \frac{1}{2}$  and the  $\Sigma$  as a hyperon with  $I = \frac{1}{2}$  or  $I = \frac{3}{2}$ . The necessary isospin operators are then the ones allowing for isospin  $(\frac{1}{2}\frac{1}{2})t'm'_t \rightarrow (\frac{1}{2}\frac{1}{2})tm_t$  and  $(\frac{3}{2}\frac{1}{2})t'm'_t \rightarrow (\frac{1}{2}\frac{1}{2})tm_t$  transitions. The first transition is driven by the unity operator and by  $\vec{\tau}_1 \cdot \vec{\tau}_2$ , where  $\vec{\tau}_i$  are the Pauli matrices for the i-vertex defined in Eq. (B.2). The second transition is driven by  $\vec{T} \cdot \vec{\tau}$ , where  $\vec{T}$  are the matrices mediating  $\frac{3}{2} \rightarrow \frac{1}{2}$  transitions, with components

$$T_1 = \begin{pmatrix} -\frac{1}{\sqrt{2}} & 0 & \frac{1}{\sqrt{6}} & 0 \\ 0 & -\frac{1}{\sqrt{6}} & 0 & \frac{1}{\sqrt{2}} \end{pmatrix}, \quad (C.1)$$

$$T_2 = \begin{pmatrix} -\frac{i}{\sqrt{2}} & 0 & -\frac{i}{\sqrt{6}} & 0 \\ 0 & -\frac{i}{\sqrt{6}} & 0 & -\frac{i}{\sqrt{2}} \end{pmatrix}, \quad (C.2)$$

$$T_3 = \begin{pmatrix} 0 & \sqrt{\frac{2}{3}} & 0 & 0 \\ 0 & 0 & \sqrt{\frac{2}{3}} & 0 \end{pmatrix}. \quad (C.3)$$

These operators connect a final NN state with an initial  $\tilde{Y}N$  one, where  $\tilde{Y}$  indicates a hyperon coupled to an isospin of  $|\frac{1}{2}, -\frac{1}{2}\rangle$ . The following sections show the isospin matrix elements for the three operators, namely 1,  $\vec{\tau}_1 \cdot \vec{\tau}_2$ , and  $\vec{T}_1 \cdot \vec{\tau}_2$ . In the last section we relate the possible initial isospin states for the  $\Lambda N$  and  $\Sigma N$  pairs appearing in the hypertriton wave function, with the  $\tilde{\Lambda}N$  and  $\tilde{\Sigma}N$  ones.

### C.1 Unity operator ( $\hat{1}$ )

$$\langle (\frac{1}{2}\frac{1}{2})t'm'_t | (\frac{1}{2}\frac{1}{2})tm_t \rangle = \delta_{tt'} \delta_{m_tm'_t} \quad (C.4)$$

### C.2 Operator ( $\vec{\tau}_1 \cdot \vec{\tau}_2$ )

$$\langle (\frac{1}{2}\frac{1}{2})t'm'_t | \vec{\tau}_1 \cdot \vec{\tau}_2 | (\frac{1}{2}\frac{1}{2})tm_t \rangle = [2t(t+1) - 3] \delta_{tt'} \delta_{m_tm'_t} \quad (C.5)$$

### C.3 Operator $(\vec{T}_1 \cdot \vec{\tau}_2)$

$$\left\langle \left(\frac{1}{2}\frac{1}{2}\right)t'm'_t \middle| \vec{T}_1 \cdot \vec{\tau}_2 \middle| \left(\frac{3}{2}\frac{1}{2}\right)tm_t \right\rangle = -\frac{4}{\sqrt{6}}\delta_{tt'}\delta_{m_tm'_t}\delta_{t1} \quad (\text{C.6})$$

### C.4 Relation between isospin basis and isopurious basis

In this section we relate the isospin states of the  $\Lambda N$  and  $\Sigma N$  pairs contributing to the hypertriton wave function with the isospin states where an isospin of  $|\frac{1}{2} - \frac{1}{2}\rangle$  has been coupled to the hyperons. We proceed as following: first, we define the isospin states for the  $\Lambda$  and the  $\Sigma$  hyperons; second, we define the isopurious states  $\tilde{\Lambda}$  and  $\tilde{\Sigma}$  by coupling  $|\frac{1}{2} - \frac{1}{2}\rangle$  to the  $\Lambda$  and the  $\Sigma$  states; third, we couple the isopurious states to a nucleon isospin state; and fourth, we write these isopurious states in the isospin basis.

The  $\Lambda$  and the  $\Sigma$  isospin states are defined as

$$\begin{aligned} |\Lambda\rangle &= |0, 0\rangle ; \\ |\Sigma^+\rangle &= -|1, 1\rangle , \\ |\Sigma^0\rangle &= |1, 0\rangle , \\ |\Sigma^-\rangle &= |1, -1\rangle . \end{aligned} \quad (\text{C.7})$$

Coupling  $|\frac{1}{2} - \frac{1}{2}\rangle$  to these states we obtain

$$\begin{aligned} |\tilde{\Lambda}\rangle &= |\frac{1}{2}, -\frac{1}{2}\rangle ; \\ |\tilde{\Sigma}^+\rangle &= -\sqrt{\frac{2}{3}}|\frac{1}{2}\frac{1}{2}\rangle - \frac{1}{\sqrt{3}}|\frac{3}{2}\frac{1}{2}\rangle , \\ |\tilde{\Sigma}^0\rangle &= \frac{1}{\sqrt{3}}|\frac{1}{2} - \frac{1}{2}\rangle + \sqrt{\frac{2}{3}}|\frac{3}{2} - \frac{1}{2}\rangle , \\ |\tilde{\Sigma}^-\rangle &= |\frac{3}{2} - \frac{3}{2}\rangle . \end{aligned} \quad (\text{C.8})$$

We now couple the states above to the isospin of a nucleon. Since the operators mediating the transitions  $(\frac{1}{2}\frac{1}{2})t'm'_t \rightarrow (\frac{1}{2}\frac{1}{2})tm_t$  and  $(\frac{3}{2}\frac{1}{2})t'm'_t \rightarrow (\frac{1}{2}\frac{1}{2})tm_t$  have independent couplings we must keep the contributions with  $I = \frac{1}{2}$  and  $I = \frac{3}{2}$  separate. We label them with the

subscripts  $\frac{1}{2}$  and  $\frac{3}{2}$ .

$$\begin{aligned}
|\tilde{\Lambda}p\rangle &= |\frac{1}{2} - \frac{1}{2}\rangle |\frac{1}{2} \frac{1}{2}\rangle \\
&= \frac{1}{\sqrt{2}} |1, 0\rangle_{1/2} - \frac{1}{\sqrt{2}} |0, 0\rangle_{1/2} \\
|\tilde{\Lambda}n\rangle &= |\frac{1}{2} - \frac{1}{2}\rangle |\frac{1}{2} - \frac{1}{2}\rangle \\
&= |1, -1\rangle_{1/2} \\
|\tilde{\Sigma}^+ p\rangle &= -\sqrt{\frac{2}{3}} |\frac{1}{2} \frac{1}{2}\rangle |\frac{1}{2} \frac{1}{2}\rangle - \frac{1}{\sqrt{3}} |\frac{3}{2} \frac{1}{2}\rangle |\frac{1}{2} \frac{1}{2}\rangle \\
&= -\sqrt{\frac{2}{3}} |1, 1\rangle_{1/2} - \frac{1}{2} |2, 1\rangle_{3/2} + \frac{1}{\sqrt{12}} |1, 1\rangle_{3/2} \\
|\tilde{\Sigma}^0 p\rangle &= \frac{1}{\sqrt{3}} |\frac{1}{2} - \frac{1}{2}\rangle |\frac{1}{2} \frac{1}{2}\rangle + \sqrt{\frac{2}{3}} |\frac{3}{2} - \frac{1}{2}\rangle |\frac{1}{2} \frac{1}{2}\rangle \\
&= \frac{1}{\sqrt{6}} |1, 0\rangle_{1/2} - \frac{1}{\sqrt{6}} |0, 0\rangle_{1/2} + \frac{1}{\sqrt{3}} |2, 0\rangle_{3/2} - \frac{1}{\sqrt{3}} |1, 0\rangle_{3/2} \\
|\tilde{\Sigma}^- p\rangle &= |\frac{3}{2} - \frac{3}{2}\rangle |\frac{1}{2} \frac{1}{2}\rangle \\
&= \frac{1}{2} |2, -1\rangle_{3/2} - \frac{\sqrt{3}}{2} |1, -1\rangle_{3/2} \\
|\tilde{\Sigma}^+ n\rangle &= -\sqrt{\frac{2}{3}} |\frac{1}{2} \frac{1}{2}\rangle |\frac{1}{2} - \frac{1}{2}\rangle - \frac{1}{\sqrt{3}} |\frac{3}{2} \frac{1}{2}\rangle |\frac{1}{2} - \frac{1}{2}\rangle \\
&= -\frac{1}{\sqrt{3}} |1, 0\rangle_{1/2} - \frac{1}{\sqrt{3}} |0, 0\rangle_{1/2} - \frac{1}{\sqrt{6}} |2, 0\rangle_{3/2} - \frac{1}{\sqrt{6}} |1, 0\rangle_{3/2} \\
|\tilde{\Sigma}^0 n\rangle &= \frac{1}{\sqrt{3}} |\frac{1}{2} - \frac{1}{2}\rangle |\frac{1}{2} - \frac{1}{2}\rangle + \sqrt{\frac{2}{3}} |\frac{3}{2} - \frac{1}{2}\rangle |\frac{1}{2} - \frac{1}{2}\rangle \\
&= \frac{1}{\sqrt{3}} |1, -1\rangle_{1/2} + \frac{1}{\sqrt{2}} |2, -1\rangle_{3/2} + \frac{1}{\sqrt{6}} |1, -1\rangle_{3/2} \\
|\tilde{\Sigma}^- n\rangle &= |\frac{3}{2} - \frac{3}{2}\rangle |\frac{1}{2} - \frac{1}{2}\rangle \\
&= |2, -2\rangle_{3/2}
\end{aligned} \tag{C.9}$$

The final step is to express the isospin states appearing the wave function of the hypertriton in terms of the states listed above. Since the hypertriton has zero isospin, the only allowed states for the hyperon-nucleon pair are

$$\begin{aligned}
|\frac{1}{2} \frac{1}{2}\rangle_\Lambda &= |\Lambda p\rangle, \\
|\frac{1}{2} - \frac{1}{2}\rangle_\Lambda &= |\Lambda n\rangle; \\
|\frac{1}{2} \frac{1}{2}\rangle_\Sigma &= -\sqrt{\frac{2}{3}} |\Sigma^+ n\rangle - \frac{1}{\sqrt{3}} |\Sigma^0 p\rangle, \\
|\frac{1}{2} - \frac{1}{2}\rangle_\Sigma &= \frac{1}{\sqrt{3}} |\Sigma^0 n\rangle - \sqrt{\frac{2}{3}} |\Sigma^- p\rangle.
\end{aligned} \tag{C.10}$$

We now replace in the formulas above the states  $|YN\rangle$  by the  $\left|\tilde{Y}N\right\rangle$  ones, obtaining thus

$$\begin{aligned} \left| \frac{1}{2} \frac{1}{2} \right\rangle_{\tilde{\Lambda}} &= \frac{1}{3\sqrt{2}} |1, 0\rangle_{1/2} - \frac{1}{\sqrt{2}} |0, 0\rangle_{1/2}, \\ \left| \frac{1}{2} - \frac{1}{2} \right\rangle_{\tilde{\Lambda}} &= |1, -1\rangle_{1/2}, \\ \left| \frac{1}{2} \frac{1}{2} \right\rangle_{\tilde{\Sigma}} &= \frac{1}{\sqrt{2}} |1, 0\rangle_{1/2} + \frac{1}{\sqrt{2}} |0, 0\rangle_{1/2} + \frac{2}{3} |1, 0\rangle_{3/2}, \\ \left| \frac{1}{2} - \frac{1}{2} \right\rangle_{\tilde{\Sigma}} &= \frac{1}{3} |1, -1\rangle_{1/2} + \frac{2\sqrt{2}}{3} |1, -1\rangle_{3/2}. \end{aligned} \quad (\text{C.11})$$

Given an initial and a final state in the isospin basis, now one can easily calculate the matrix elements for the different operators defined in the previous sections. Tables C.1 and C.2 show these matrix elements in the cases where the initial hyperon is a  $\Lambda$  and a  $\Sigma$ , respectively. We label the isospin of the two initial baryons with  $|t'_{12}m_{t'_{12}}\rangle$ , and the isospin of the final ones with  $|t'_{12}m'_{t'_{12}}\rangle$ .

$t'_{12}$	$m_{t'_{12}}$	1	$\tau \cdot \tau$
$\frac{1}{2}$	$-\frac{1}{2}$	$\delta_{t'_{12}1}\delta_{m'_{t'_{12}}-1}$	$\delta_{t'_{12}1}\delta_{m'_{t'_{12}}-1}$
$\frac{1}{2}$	$\frac{1}{2}$	$-\frac{1}{\sqrt{2}}\delta_{t'_{12}0}\delta_{m'_{t'_{12}}0} + \frac{1}{\sqrt{2}}\delta_{t'_{12}1}\delta_{m'_{t'_{12}}0}$	$\frac{3}{\sqrt{2}}\delta_{t'_{12}0}\delta_{m'_{t'_{12}}0} + \frac{1}{\sqrt{2}}\delta_{t'_{12}1}\delta_{m'_{t'_{12}}0}$

Table C.1: Matrix elements between  $\Lambda N$  and  $NN$  states in the isospin basis and according to the  $\Delta I = \frac{1}{2}$  rule.

$t'_{12}$	$m_{t'_{12}}$	1	$\tau \cdot \tau$	$T \cdot \tau$
$\frac{1}{2}$	$-\frac{1}{2}$	$\frac{1}{3}\delta_{t'_{12}1}\delta_{m'_{t'_{12}}-1}$	$\frac{1}{3}\delta_{t'_{12}1}\delta_{m'_{t'_{12}}-1}$	$-\frac{8}{3\sqrt{3}}\delta_{t'_{12}1}\delta_{m'_{t'_{12}}-1}$
$\frac{1}{2}$	$\frac{1}{2}$	$\frac{1}{\sqrt{2}}\delta_{t'_{12}0}\delta_{m'_{t'_{12}}0} + \frac{1}{3\sqrt{2}}\delta_{t'_{12}1}\delta_{m'_{t'_{12}}0}$	$-\frac{3}{\sqrt{2}}\delta_{t'_{12}0}\delta_{m'_{t'_{12}}0} + \frac{1}{3\sqrt{2}}\delta_{t'_{12}1}\delta_{m'_{t'_{12}}0}$	$-\frac{4\sqrt{2}}{3\sqrt{3}}\delta_{t'_{12}1}\delta_{m'_{t'_{12}}0}$

Table C.2: Matrix elements between  $\Sigma N$  and  $NN$  states in the isospin basis and according to the  $\Delta I = \frac{1}{2}$  rule.

# Appendix D

## Diagrams

### D.1 Caramel diagrams

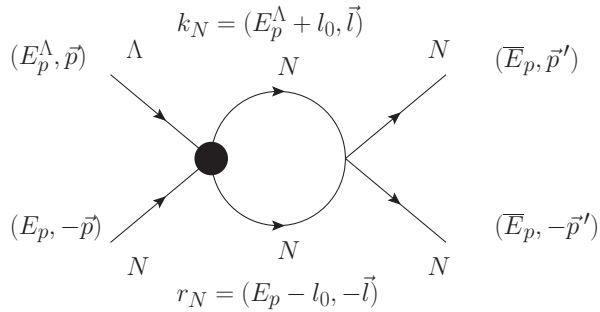


Figure D.1: First caramel-type Feynman diagram

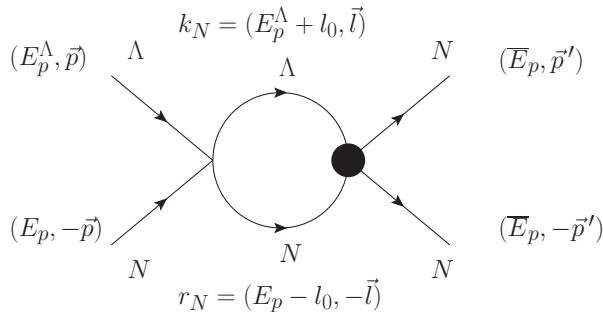


Figure D.2: Second caramel-type Feynman diagram

Using the same notation that is described in section 3.4.1 we write a general expression for the three caramel diagrams that depends on the label  $\alpha = a, b, c$ , which corresponds, respectively, to the masses and vertices of Figs. D.1, D.2, and D.3. The relativistic

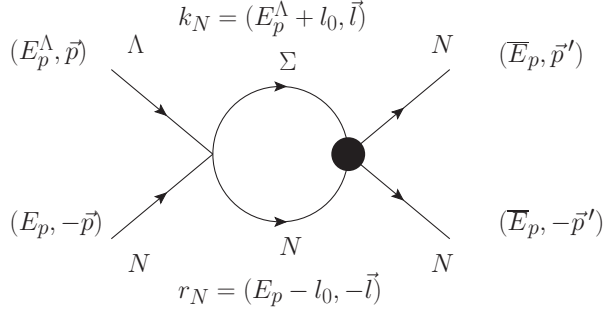


Figure D.3: Third caramel-type Feynman diagram

expression for our caramel diagrams is,

$$V_\alpha = iG_F m_\pi^2 (C_{00(s)}^\alpha + C_{01(s)}^\alpha \vec{\sigma}_1 \cdot \vec{\sigma}_2) (C_{00(w)}^\alpha + C_{01(w)}^\alpha \vec{\sigma}_1 \cdot \vec{\sigma}_2) \times \int \frac{d^4 l}{(2\pi)^4} \frac{1}{(E_p - l_0)^2 - \vec{l}^2 - M_N^2 + i\epsilon} \frac{1}{(E_p^\Lambda + l_0)^2 - \vec{l}^2 - M_\alpha^2}. \quad (\text{D.1})$$

In order to not miss the relativistic pole we must first integrate the temporal part ( $l_0$ ) before heavy-baryon expand the expression. Proceeding in this manner one obtains a purely imaginary part (the real is suppressed in the heavy baryon expansion).

$$V_\alpha = -\frac{G_F m_\pi^2}{4M_N} (C_{00(s)}^\alpha + C_{01(s)}^\alpha \vec{\sigma}_1 \cdot \vec{\sigma}_2) (C_{00(w)}^\alpha + C_{01(w)}^\alpha \vec{\sigma}_1 \cdot \vec{\sigma}_2) \times \int \frac{d^3 l}{(2\pi)^3} \frac{1}{(\Delta_b - \Delta_\alpha)(\frac{1}{2}(\Delta_b + \Delta_\alpha) + M_N) + \vec{p}^2 - \vec{l}^2} = i \frac{G_F m_\pi^2}{16\pi M_N} (C_{00(s)}^\alpha + C_{01(s)}^\alpha \vec{\sigma}_1 \cdot \vec{\sigma}_2) (C_{00(w)}^\alpha + C_{01(w)}^\alpha \vec{\sigma}_1 \cdot \vec{\sigma}_2) \times \sqrt{(\Delta_b - \Delta_\alpha)(\frac{1}{2}(\Delta_b + \Delta_\alpha) + M_N) + \vec{p}^2}. \quad (\text{D.2})$$

## D.2 Ball diagrams

In our calculation we have two different kind of ball diagrams depending on the position of the weak vertex, although only one of them actually contributes. Their contribution can be written in terms of the  $B$  integrals defined in Appendix E.

Here and in the following sections we first write the relativistic amplitude using  $V = i M$  and then the corresponding heavy baryon expression.

For the first type of ball diagram, depicted in Fig. D.4, we obtain the following contribution,

$$V_{\text{ball } 1} = \frac{G_F m_\pi^2 h_{2\pi}}{4f_\pi^4} \delta_{ab} \epsilon^{abc} \tau^c \times \int \frac{d^4 l}{(2\pi)^4} \frac{1}{l^2 - m_\pi^2 + i\epsilon} \frac{1}{(l - q)^2 - m_\pi^2 + i\epsilon} \times \bar{u}_1(\bar{E}, \vec{p}') u_1(E_p^\Lambda, \vec{p}) \times \bar{u}_2(\bar{E}_p, -\vec{p}') \gamma_\mu (q^\mu - 2l^\mu) u_2(E_p, -\vec{p}) = 0, \quad (\text{D.3})$$

which is shown to vanish due to the isospin factor,  $\delta_{ab}\epsilon^{abc}\tau^c = 0$ .

The amplitude corresponding to the diagram in Fig. D.5 reads,

$$V_a = -i \frac{G_F m_\pi^2 h_{\Lambda N}}{8 f_\pi^4} (\vec{\tau}_1 \cdot \vec{\tau}_2) \int \frac{d^4 l}{(2\pi)^4} \frac{1}{l^2 - m_\pi^2 + i\epsilon} \frac{1}{(l+q)^2 - m_\pi^2 + i\epsilon} \\ \times \frac{(2l^\mu + q^\mu)(q^\nu + 2l^\nu)}{k_N^2 - M_N^2 + i\epsilon} \bar{u}_1(\bar{E}, \vec{p}') \gamma_\mu (\mathcal{K}_N + M_N) u_1(E_p^\Lambda, \vec{p}) \bar{u}_2(\bar{E}_p, -\vec{p}') \gamma_\nu u_2(E_p, -\vec{p}). \quad (\text{D.4})$$

Using heavy baryon expansion,

$$V_a = \frac{G_F m_\pi^2 h_{\Lambda N}}{8 \Delta M f_\pi^4} (\vec{\tau}_1 \cdot \vec{\tau}_2) (4B_{20} + 4q_0 B_{10} + q_0^2 B), \quad (\text{D.5})$$

where we have used the master integrals with  $q_0 = -\frac{M_\Lambda - M_N}{2}$  and  $\vec{q} = \vec{p}' - \vec{p}$ .

### D.3 Triangle diagrams

Two up triangles and two down triangles contribute to the interaction. The final expressions are written in terms of the integrals  $I$  defined in Appendix E. The amplitude for the first up triangle, depicted in Fig. D.6, is

$$V_b = -i \frac{3}{8} \frac{G_F m_\pi^2 h_{2\pi} g_A^2}{M_N f_\pi^4} \int \frac{d^4 l}{(2\pi)^4} \frac{1}{l^2 - m_\pi^2 + i\epsilon} \frac{1}{(l+q)^2 - m_\pi^2 + i\epsilon} \frac{(l^\mu + q^\mu)l^\nu}{k_N^2 - M_N^2 + i\epsilon} \\ \times \bar{u}_1(\bar{E}_p, \vec{p}') \bar{u}_1(E_p^\Lambda, \vec{p}) \bar{u}_2(\bar{E}_p, -\vec{p}') \gamma_\mu \gamma_5 (\mathcal{K}_N + M_N) \gamma_\nu \gamma_5 u_2(E_p, -\vec{p}). \quad (\text{D.6})$$

Using heavy baryon expansion,

$$V_b = \frac{3}{4} \frac{G_F m_\pi^2 h_{2\pi} g_A^2}{f_\pi^4} [(3-\eta)I_{22} + \vec{q}^2 I_{23} + \vec{q}^2 I_{11}], \quad (\text{D.7})$$

where, we have used the master integrals with  $q_0 = \frac{M_\Lambda - M_N}{2}$ ,  $q'_0 = 0$  and  $\vec{q} = \vec{p}' - \vec{p}$ .

For the second up triangle, depicted in Fig. D.7, the relativistic amplitude is

$$V_c = -i \frac{G_F m_\pi^2 h_{\Lambda N} g_A^2}{8 f_\pi^4 (r_N^2 - M_N^2)} \vec{\tau}_1 \cdot \vec{\tau}_2 \int \frac{d^4 l}{(2\pi)^4} \frac{1}{l^2 - m_\pi^2 + i\epsilon} \frac{1}{(l+q)^2 - m_\pi^2 + i\epsilon} \frac{(2l^\rho + q^\rho)(l^\mu + q^\mu)l^\nu}{k_N^2 - M_N^2 + i\epsilon} \\ \times \bar{u}_1(\bar{E}, \vec{p}') \gamma_\rho (\mathcal{K}_N + M_N) u_1(E_p^\Lambda, \vec{p}) \bar{u}_2(\bar{E}_p, -\vec{p}') \gamma_\mu \gamma_5 (\mathcal{K}_N + M_N) \gamma_\nu \gamma_5 u_2(E_p, -\vec{p}). \quad (\text{D.8})$$

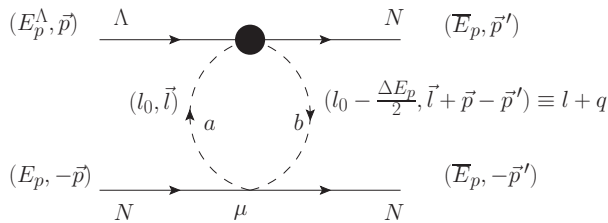


Figure D.4: Kinematical variables of the first kind of ball-diagram.

Using heavy baryon expansion,

$$V_c = \frac{G_F m_\pi^2 h_{\Lambda N} g_A^2}{8 \Delta M f_\pi^4} \vec{\tau}_1 \cdot \vec{\tau}_2 [2(3 - \eta) I_{32} + 2\vec{q}^2 I_{33} + 2\vec{q}^2 I_{21}(3 - \eta) q_0 I_{22} + q_0 \vec{q}^2 I_{23} + q_0 \vec{q}^2 I_{11}] , \quad (\text{D.9})$$

where, we have used the master integrals with  $q_0 = \frac{M_\Lambda - M_N}{2}$ ,  $q'_0 = 0$  and  $\vec{q} = \vec{p}' - \vec{p}$ .

The amplitude for the first down triangle (Fig. D.8) is

$$V_d = i \frac{G_F m_\pi^2 g_A}{4 f_\pi^3} (\vec{\tau}_1 \cdot \vec{\tau}_2) \int \frac{d^4 l}{(2\pi)^4} \frac{1}{l^2 - m_\pi^2 + i\epsilon} \frac{1}{(l+q)^2 - m_\pi^2 + i\epsilon} \frac{(l^\nu + q^\nu)(2l^\mu + q^\mu)}{k_N^2 - M_N^2 + i\epsilon} \\ \times \bar{u}_1(\bar{E}, \vec{p}') \gamma_\nu \gamma_5 (\not{k}_N + M_N) (A + B \gamma_5) u_1(E_p^\Lambda, \vec{p}) \bar{u}_2(\bar{E}_p, -\vec{p}') \gamma_\mu u_2(E_p, -\vec{p}) , \quad (\text{D.10})$$

with the heavy baryon expansion, it reduces to,

$$V_d = - \frac{G_F m_\pi^2 g_A}{8 M_N f_\pi^3} (\vec{\tau}_1 \cdot \vec{\tau}_2) \left[ B(2I_{30} + 7q_0 I_{20} + 7q_0^2 I_{10} 2q_0^3 I - 2(3 - \eta) I_{32} - (3 - \eta) q_0 I_{22}) \right. \\ - B(2I_{21} + q_0 I_{11} + 2I_{33} + q_0 I_{23}) \vec{q}^2 - B(2I_{10} + 2I_{21} + q_0 I + q_0 I_{11}) (\vec{q} \cdot \vec{p}) \\ \left. + 2A M_N (2I_{21} + q_0 I_{11} - 2I_{10} - q_0 I) \vec{\sigma}_1 \cdot \vec{q} i B(-2I_{21} - q_0 I_{11} + 2I_{10} + q_0 I) \vec{\sigma}_1 (\vec{q} \times \vec{p}) \right] . \quad (\text{D.11})$$

We have used the master integrals with  $q_0 = -\frac{M_\Lambda - M_N}{2}$ ,  $q'_0 = -M_\Lambda + M_N$  and  $\vec{q} = \vec{p}' - \vec{p}$ .

The second type of down-triangle diagram involves the intermediate exchange of the  $\Sigma$  (Fig. D.9). Its amplitude is

$$V_e = \frac{G_F m_\pi^2 D_s}{4\sqrt{3} f_\pi^3} \int \frac{d^4 l}{(2\pi)^4} \frac{1}{l^2 - m_\pi^2 + i\epsilon} \frac{1}{(l+q)^2 - m_\pi^2 + i\epsilon} \frac{(2l^\mu + q^\mu) l^\nu}{k_N^2 - M_\Sigma^2 + i\epsilon} \\ \times \bar{u}_1(\bar{E}, \vec{p}') (A_\Sigma + B_\Sigma \gamma_5) (\not{k}_N + M_\Sigma) \gamma_\nu \gamma_5 u_1(E_p^\Lambda, \vec{p}) \bar{u}_2(\bar{E}_p, -\vec{p}') \gamma_\mu u_2(E_p, -\vec{p}) . \quad (\text{D.12})$$

Using the heavy baryon expansion

$$V_e = - \frac{G_F m_\pi^2 D_s}{8\sqrt{3} M_N f_\pi^3} \left[ B_\Sigma \left( -2I_{30} + (-5q_0 - 2\Delta M_\Sigma) I_{20} + 2(3 - \eta) I_{32} + 2\vec{q}^2 I_{33} \right. \right. \\ \left. \left. + 2\vec{q}^2 I_{21} + \vec{q}^2 I_{21} q_0 (-2q_0 - \Delta M_\Sigma) I_{10} + (3 - \eta) q_0 I_{22} + q_0 \vec{q}^2 I_{23} + q_0 \vec{q}^2 I_{11} \right) \right. \\ \left. - 2A_\Sigma M_N (2I_{21} + q_0 I_{11}) (\vec{\sigma}_1 \cdot \vec{q}) \right] . \quad (\text{D.13})$$

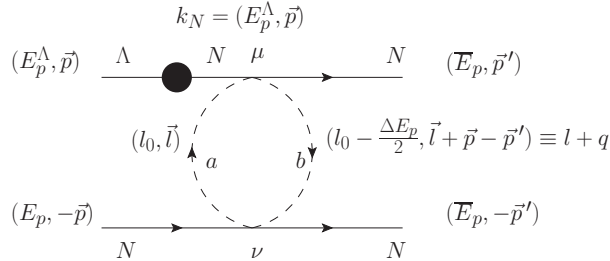


Figure D.5: Kinematical variables of the second kind of ball-diagram.

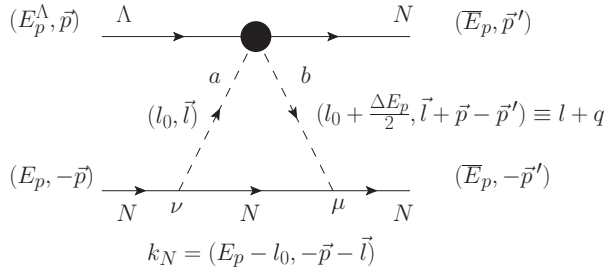


Figure D.6: Up triangle diagram contributing at NLO.

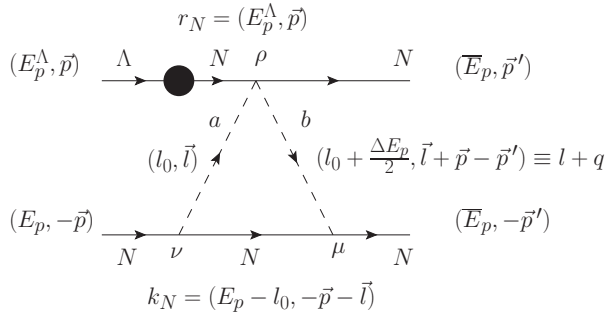


Figure D.7: Second up triangle contribution at NLO.

The isospin is taken into account by replacing every  $A_\Sigma$  and  $B_\Sigma$  by

$$\frac{2}{3} \left( \sqrt{3} A_{\Sigma \frac{1}{2}} + A_{\Sigma \frac{3}{2}} \right) \vec{\tau}_1 \cdot \vec{\tau}_2, \quad \frac{2}{3} \left( \sqrt{3} B_{\Sigma \frac{1}{2}} + B_{\Sigma \frac{3}{2}} \right) \vec{\tau}_1 \cdot \vec{\tau}_2, \quad (\text{D.14})$$

where, we have used the master integrals with  $q_0 = -\frac{M_\Lambda - M_N}{2}$ ,  $q'_0 = M_\Sigma - M_\Lambda$  and  $\vec{q} = \vec{p}' - \vec{p}$ .

## D.4 Box diagrams

We have two kind of direct box diagrams and two cross-box ones. Direct box diagrams usually present a pinch singularity. This is because the poles appearing in the baryonic propagators get infinitesimally close to one another. In our integrals the denominators appearing in the baryonic propagators also contain terms proportional to  $M_\Lambda - M_N$  and  $M_\Sigma - M_\Lambda$ , and this avoids the singularity.

The integrals entering in the expression of the amplitudes are the  $J$  and  $K$  defined in Appendix E. The amplitude for the first type of box diagram (Fig. D.10) is

$$\begin{aligned} V_f = & i \frac{G_F m_\pi^2 g_A^3}{8 f_\pi^3} (3 - 2 \vec{\tau}_1 \cdot \vec{\tau}_2) \int \frac{d^4 l}{(2\pi)^4} \frac{1}{l^2 - m_\pi^2 + i\epsilon} \frac{1}{(l + q)^2 - m_\pi^2 + i\epsilon} \frac{1}{k_N^2 - M_N^2 + i\epsilon} \\ & \times \frac{(l^\rho + q^\rho)(l^\nu + q^\nu) l^\mu}{r_N^2 - M_N^2 + i\epsilon} \bar{u}_1(\bar{E}, \vec{p}') \gamma_\rho \gamma_5 (\mathcal{K}_N + M_N) (A + B \gamma_5) u_1(E_p^\Lambda, \vec{p}) \\ & \times \bar{u}_2(\bar{E}_p, -\vec{p}') \gamma_\nu \gamma_5 (\gamma_N + M_N) \gamma_\mu \gamma_5 u_2(E_p, -\vec{p}). \end{aligned} \quad (\text{D.15})$$

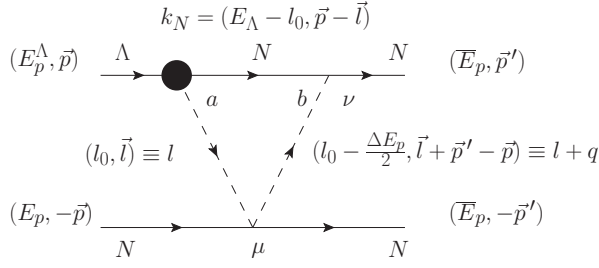
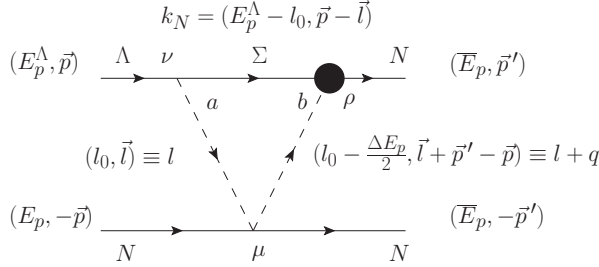


Figure D.8: “Down”-triangle contribution at NLO.

Figure D.9: Second type of down-triangle involving the intermediate exchange of a  $\Sigma$ .

Using the heavy baryon expansion,

$$\begin{aligned}
V_f = & - \frac{G_F m_\pi^2 g_A^3}{32 M_N f_\pi^3} (3 - 2 \vec{\tau}_1 \cdot \vec{\tau}_2) \left[ - 4 A M_N (4 K_{22} + K_{11} \vec{q}^2 + 2 K_{23} \vec{q}^2 + K_{35} \vec{q}^2 \right. \\
& + (5 - \eta) K_{34}) \vec{\sigma}_1 \cdot \vec{q} - 2 B K_{22} (\vec{\sigma}_1 \cdot \vec{q})(\vec{\sigma}_2 \cdot \vec{q}) + 2 B K_{22} (\vec{\sigma}_1 \cdot \vec{q})(\vec{\sigma}_2 \cdot \vec{p}) \\
& - 4 i A M_N K_{22} (\vec{\sigma}_1 \times \vec{\sigma}_2) \cdot \vec{q} - 2 B (\vec{p} \cdot \vec{q} - \vec{q}^2) K_{22} \vec{\sigma}_1 \cdot \vec{\sigma}_2 + 2 i B (K_{11} \vec{q}^2 + 2 K_{23} \vec{q}^2 + K_{35} \vec{q}^2 \\
& + (4 - \eta) K_{22} + (5 - \eta) K_{34}) \vec{\sigma}_1 \cdot (\vec{p} \times \vec{q}) + 2 i B K_{22} \vec{\sigma}_2 \cdot (\vec{p} \times \vec{q}) \\
& - 2 B (K_{11} \vec{q}^2 (\vec{p} \cdot \vec{q} + 2 q_0^2) + K_{23} (2 \vec{p} \cdot \vec{q} \vec{q}^2 + 2 q_0^2 \vec{q}^2 + \vec{q}^4) + K_{35} (\vec{p} \cdot \vec{q} \vec{q}^2 + 2 \vec{q}^4)) \\
& + K_{22} ((4 - \eta) \vec{p} \cdot \vec{q} + \vec{q}^2 + (6 - 2\eta) q_0^2) + (5 - \eta) K_{34} (\vec{p} \cdot \vec{q} + 2 \vec{q}^2) + K_{48} \vec{q}^4 + K_{21} \vec{q}^2 q_0 \\
& + K_{33} \vec{q}^2 q_0 - K_{31} \vec{q}^2 - K_{43} \vec{q}^2 + 2(5 - \eta) K_{47} \vec{q}^2 + (3 - \eta) K_{32} q_0 \\
& \left. - (3 - \eta) K_{42} + (15 - 8\eta) K_{46} \right] ,
\end{aligned}$$

where we have used the master integrals with  $q_0 = -\frac{M_\Lambda - M_N}{2}$ ,  $q'_0 = M_N - M_\Lambda$ , and  $\vec{q} = \vec{p}' - \vec{p}$ .

The second box diagram (Fig. D.11), which involves a  $\Sigma$  propagator, contributes with

$$\begin{aligned}
V_g = & - i \frac{G_F m_\pi^2 g_A^2 D_s}{4 \sqrt{3} f_\pi^3} \int \frac{d^4 l}{(2\pi)^4} \frac{1}{l^2 - m_\pi^2 + i\epsilon} \frac{1}{(l + q)^2 - m_\pi^2 + i\epsilon} \frac{1}{k_N^2 - M_\Sigma^2 + i\epsilon} \\
& \times \frac{l^\rho (l^\nu + q^\nu) l^\mu}{r_N^2 - M_N^2 + i\epsilon} \bar{u}_1(\overline{E}, \vec{p}') (A_\Sigma + B_\Sigma \gamma_5) (\mathcal{K}_N + M_N) \gamma_\rho \gamma_5 u_1(E_p^{\Lambda}, \vec{p}) \\
& \times \bar{u}_2(\overline{E}_p, -\vec{p}') \gamma_\nu \gamma_5 (\not{p}_N + M_N) \gamma_\mu \gamma_5 u_2(E_p, -\vec{p}) .
\end{aligned} \tag{D.16}$$

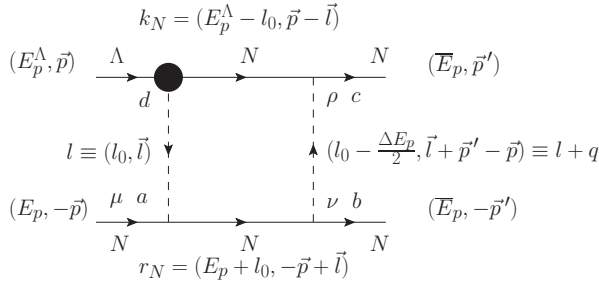


Figure D.10: Box diagram contributing at NLO.

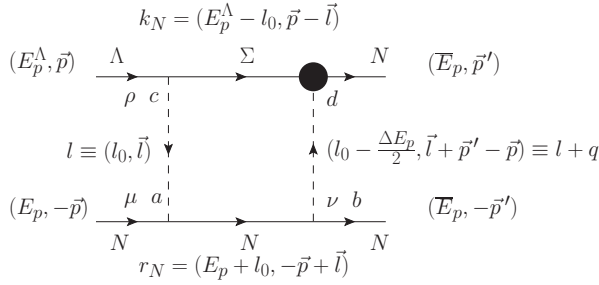


Figure D.11: Second box-type Feynman diagram.

Using the heavy baryon expansion

$$\begin{aligned}
V_g = & \frac{G_F m_\pi^2 g_A^2 D_s}{16\sqrt{3} M_N f_\pi^3} \left[ -2B_\Sigma K_{22} \vec{q}^2 \vec{\sigma}_1 \cdot \vec{\sigma}_2 - 4A_\Sigma K_{22} M_N i (\vec{\sigma}_1 \times \vec{\sigma}_2) \vec{q} \right. \\
& - 4A_\Sigma M_N (\vec{q}^2 K_{23} + 5K_{34} + \vec{q}^2 K_{35} + K_{22}) \vec{\sigma}_1 \cdot \vec{q} + 2B_\Sigma K_{22} (\vec{\sigma}_1 \cdot \vec{q})(\vec{\sigma}_2 \cdot \vec{q}) \\
& + 2B_\Sigma (\vec{q}^2 K_{22} + \vec{q}^4 K_{23} - \vec{q}^2 K_{31} + (3-\eta)(\Delta M - \Delta M_\Sigma) K_{32} + \vec{q}^2 (\Delta M - \Delta M_\Sigma) K_{33} \\
& + 2(5-\eta) \vec{q}^2 K_{34} + 2\vec{q}^4 K_{35} - (3-\eta) K_{42} - \vec{q}^2 K_{43} + (15-8\eta) K_{46} \\
& \left. + 2(5-\eta) \vec{q}^2 K_{47} + \vec{q}^4 K_{48} + \vec{q}^2 K_{21} (\Delta M - \Delta M_\Sigma) \right].
\end{aligned} \tag{D.17}$$

To take into account the isospin we must replace every  $A_\Sigma$  and  $B_\Sigma$  by

$$A \rightarrow -\sqrt{3} A_{\Sigma \frac{1}{2}} + 2 A_{\Sigma \frac{3}{2}} + \frac{2}{3} (\sqrt{3} A_{\Sigma \frac{1}{2}} + A_{\Sigma \frac{3}{2}}) \vec{\tau}_1 \cdot \vec{\tau}_2 \tag{D.18}$$

$$B \rightarrow -\sqrt{3} B_{\Sigma \frac{1}{2}} + 2 B_{\Sigma \frac{3}{2}} + \frac{2}{3} (\sqrt{3} B_{\Sigma \frac{1}{2}} + B_{\Sigma \frac{3}{2}}) \vec{\tau}_1 \cdot \vec{\tau}_2. \tag{D.19}$$

We have used the master integrals with  $q_0 = -\frac{M_\Lambda - M_N}{2}$ ,  $q'_0 = M_\Sigma - M_\Lambda$ , and  $\vec{q} = \vec{p}' - \vec{p}$ .

The second crossed box diagram (Fig. D.12) includes a  $\Sigma$ -propagator and contributes to the potential with

$$\begin{aligned}
V_h = & i \frac{G_F m_\pi^2 g_A^3}{8 f_\pi^3} (3 + 2\vec{\tau}_1 \cdot \vec{\tau}_2) \int \frac{d^4 l}{(2\pi)^4} \frac{1}{(l+q)^2 - m_\pi^2 + i\epsilon} \frac{1}{l^2 - m_\pi^2 + i\epsilon} \frac{1}{r_N^2 - M_N^2 + i\epsilon} \\
& \times \frac{(l^\rho)(l^\nu + q^\nu)(l^\mu)}{k_N^2 - M_N^2 + i\epsilon} \bar{u}_1(\bar{E}, \vec{p}') \gamma_\rho \gamma_5 (\mathcal{K}_N + M_N) (A + B \gamma_5) u_1(E_p^\Lambda, \vec{p}) \\
& \times \bar{u}_2(\bar{E}_p, -\vec{p}') \gamma_\nu \gamma_5 (\gamma_N + M_N) \gamma_\mu \gamma_5 u_2(E_p, -\vec{p}).
\end{aligned}$$

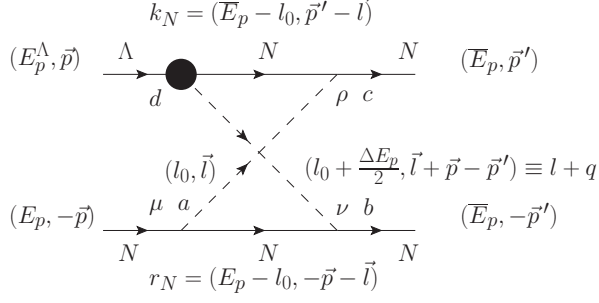


Figure D.12: Crossed-box diagram contributing at NLO.

Using heavy baryon expansion and the master integrals of Sec. E, and redefining  $\vec{q} \equiv \vec{p}' - \vec{p}$ ,

$$\begin{aligned}
V_h = & -\frac{G_F m_\pi^2 g_A^3}{32 M_N f_\pi^3} (3 + 2\vec{\tau}_1 \cdot \vec{\tau}_2) \left[ -2i B J_{22} \vec{\sigma}_2 (\vec{p} \times \vec{q}) + 2 B J_{22} (-\vec{p} \cdot \vec{q} + \vec{q}^2) \vec{\sigma}_1 \cdot \vec{\sigma}_2 \quad (\text{D.20}) \right. \\
& + 2i B (J_{22} + \vec{q}^2 J_{23} + (5 + \eta) J_{34} + \vec{q}^2 J_{35}) \vec{\sigma}_1 \cdot (\vec{p} \times \vec{q}) + 4i A J_{22} M_N (\vec{\sigma}_1 \times \vec{\sigma}_2) \vec{q} \\
& + 4 A M_N (\vec{q}^2 J_{23} + 5 J_{34} + \vec{q}^2 J_{35} + J_{22}) \vec{\sigma}_1 \cdot \vec{q} + 2 B J_{22} (\vec{\sigma}_1 \cdot \vec{q})(\vec{\sigma}_2 \cdot \vec{p}) \\
& - 2 B J_{22} (\vec{\sigma}_1 \cdot \vec{q})(\vec{\sigma}_2 \cdot \vec{q}) - 2 B (\vec{q}^2 q_0 J_{21} + (-\vec{p} \cdot \vec{q} + \vec{q}^2) J_{22} + (-\vec{p} \cdot \vec{q} \vec{q}^2 + \vec{q}^4) J_{23} \\
& - \vec{q}^2 J_{31} + (3 - \eta) q_0 J_{32} + \vec{q}^2 q_0 J_{33} + (5 - \eta) (-\vec{p} \cdot \vec{q} + 2\vec{q}^2) J_{34} + (-\vec{p} \cdot \vec{q} \vec{q}^2 + 2\vec{q}^4) J_{35} \\
& \left. - (3 - \eta) J_{42} - \vec{q}^2 J_{43} + (15 - 8\eta) J_{46} + 2(5 - \eta) \vec{q}^2 J_{47} + \vec{q}^4 J_{48}) \right].
\end{aligned}$$

We have used the master integrals with  $q_0 = \frac{M_\Lambda - M_N}{2}$ ,  $q'_0 = -\frac{M_\Lambda - M_N}{2}$ , and  $\vec{q} = \vec{p}' - \vec{p}$ .

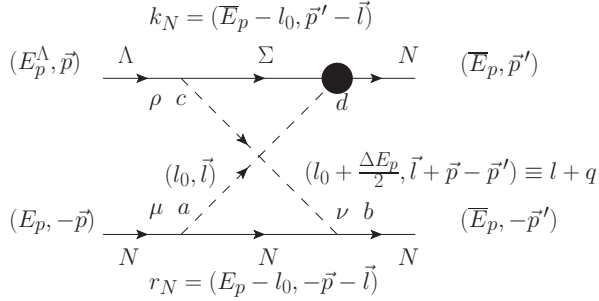


Figure D.13: Second crossed-box-type Feynman diagram

The amplitude for the crossed-box diagram with a  $\Sigma$  propagator is

$$\begin{aligned}
V_i = & -i \frac{G_F m_\pi^2 g_A^2 D_s}{16\sqrt{3} M_N^2 f_\pi^3} \int \frac{d^4 l}{(2\pi)^4} \frac{1}{(l + q)^2 - m_\pi^2 + i\epsilon} \frac{1}{l^2 - m_\pi^2 + i\epsilon} \frac{1}{r_N^2 - M_N^2 + i\epsilon} \quad (\text{D.21}) \\
& \times \frac{(l^\rho + \vec{q}^\rho)(l^\nu + q^\nu)(l^\mu)}{k_N^2 - M_\Sigma^2 + i\epsilon} \bar{u}_1(\bar{E}, \vec{p}') (A_\Sigma + B_\Sigma \gamma_5) (\mathcal{K}_N + M_N) \gamma_\rho \gamma_5 u_1(E_p^\Lambda, \vec{p}) \\
& \times \bar{u}_2(\bar{E}_p, -\vec{p}') \gamma_\nu \gamma_5 (\gamma_N + M_N) \gamma_\mu \gamma_5 u_2(E_p, -\vec{p}).
\end{aligned}$$

Using heavy baryon expansion and the master integrals of Sec. E, and redefining  $\vec{q} \equiv \vec{p}' - \vec{p}$ ,

$$V_i = \frac{G_F m_\pi^2 g_A^2 D_s}{16\sqrt{3} M_N f_\pi^3} \left[ 2B_\Sigma J_{22} \vec{q}^2 \vec{\sigma}_1 \cdot \vec{\sigma}_2 - 2i A_\Sigma J_{22} M_N (\vec{\sigma}_1 \times \vec{\sigma}_2) \cdot \vec{q} \right. \\ - A_\Sigma M_N (\vec{q}^2 J_{11} + 2\vec{q}^2 J_{23} + 5J_{34} + \vec{q}^2 J_{35} + 4J_{22}) \vec{\sigma}_1 \cdot \vec{q} - 2B_\Sigma J_{22} (\vec{\sigma}_1 \cdot \vec{q})(\vec{\sigma}_2 \cdot \vec{q}) \\ + 2B_\Sigma ((\vec{q}^2 - (3-\eta)q_0(q_0 + \Delta M_\Sigma)) J_{22} (\vec{q}^4 - \vec{q}^2 q_0^2 - \vec{q}^2 q_0 \Delta M_\Sigma) J_{23} - \vec{q}^2 J_{31} \\ - (3-\eta)(2q_0 + \Delta M_\Sigma) J_{32} - (2\vec{q}^2 q_0 + \vec{q}^2 \Delta M_\Sigma) J_{33} 2(5-\eta) \vec{q}^2 J_{34} + 2\vec{q}^4 J_{35} \\ - (3-\eta) J_{42} - \vec{q}^2 J_{43} + (15-8\eta) J_{46} + 2(5-\eta) \vec{q}^2 J_{47} + \vec{q}^4 J_{48} \\ \left. - \vec{q}^2 q_0 J_{11} (q_0 + \Delta M_\Sigma) - \vec{q}^2 J_{21} (2q_0 + \Delta M_\Sigma) \right]. \quad (\text{D.22})$$

To take into account the isospin we must replace every  $A_\Sigma$  and  $B_\Sigma$  by

$$A_\Sigma \rightarrow -\sqrt{3} A_{\Sigma \frac{1}{2}} + 2A_{\Sigma \frac{3}{2}} - \frac{2}{3}(\sqrt{3} A_{\Sigma \frac{1}{2}} + 2A_{\Sigma \frac{3}{2}}) \vec{\tau}_1 \cdot \vec{\tau}_2 \quad (\text{D.23})$$

$$B_\Sigma \rightarrow -\sqrt{3} B_{\Sigma \frac{1}{2}} + 2B_{\Sigma \frac{3}{2}} - \frac{2}{3}(\sqrt{3} B_{\Sigma \frac{1}{2}} + 2B_{\Sigma \frac{3}{2}}) \vec{\tau}_1 \cdot \vec{\tau}_2. \quad (\text{D.24})$$

We have used the master integrals with  $q_0 = \frac{M_\Lambda - M_N}{2}$ ,  $q'_0 = M_\Sigma - M_\Lambda + \frac{M_\Lambda - M_N}{2}$ , and  $\vec{q} = \vec{p}' - \vec{p}$ .



# Appendix E

## Master integrals

### E.1 Definitions

We need the following integrals in order to calculate the Feynman diagrams. The  $B$ 's,  $I$ 's,  $J$ 's and  $K$ 's appear, respectively, in the ball, triangle, box and crossed box diagrams:

$$B_{;\mu;\mu\nu} \equiv \frac{1}{i} \int \frac{d^4l}{(2\pi)^4} \frac{1}{l^2 - m^2 + i\epsilon} \frac{(1; l_\mu; l_\mu l_\nu)}{(l+q)^2 - m^2 + i\epsilon}, \quad (\text{E.1})$$

$$I_{;\mu;\mu\nu;\mu\nu\rho} \equiv \frac{1}{i} \int \frac{d^4l}{(2\pi)^4} \frac{1}{l^2 - m^2 + i\epsilon} \frac{1}{(l+q)^2 - m^2 + i\epsilon} \frac{1}{-l_0 - q'_0 + i\epsilon} (1; l_\mu; l_\mu l_\nu; l_\mu l_\nu l_\rho), \quad (\text{E.2})$$

$$J_{;\mu;\mu\nu;\mu\nu\rho} \equiv \frac{1}{i} \int \frac{d^4l}{(2\pi)^4} \frac{1}{l^2 - m^2 + i\epsilon} \frac{1}{(l+q)^2 - m^2 + i\epsilon} \frac{1}{-l_0 - q'_0 + i\epsilon} \frac{(1; l_\mu; l_\mu l_\nu; l_\mu l_\nu l_\rho)}{-l_0 + i\epsilon}, \quad (\text{E.3})$$

$$K_{;\mu;\mu\nu;\mu\nu\rho} \equiv \frac{1}{i} \int \frac{d^4l}{(2\pi)^4} \frac{1}{l^2 - m^2 + i\epsilon} \frac{1}{(l+q)^2 - m^2 + i\epsilon} \frac{1}{-l_0 - q'_0 + i\epsilon} \frac{(1; l_\mu; l_\mu l_\nu; l_\mu l_\nu l_\rho)}{l_0 + i\epsilon}. \quad (\text{E.4})$$

The strategy is to calculate explicitly the integrals with no subindex (no integrated momenta in the numerators), and then relate the others to simpler integrals. To do so we also need to explicitly calculate the following integrals:

$$A(m) \equiv \frac{1}{i} \int \frac{d^4l}{(2\pi)^4} \frac{1}{l^2 - m^2 + i\epsilon},$$

$$A_{;\mu;\mu\nu}(q, q') \equiv \frac{1}{i} \int \frac{d^4l}{(2\pi)^4} \frac{1}{(l+q)^2 - m^2 + i\epsilon} \frac{1}{-l_0 - q'_0 + i\epsilon} (1; l_\mu; l_\mu l_\nu), \quad (\text{E.5})$$

$$C_{;\mu;\mu\nu;\mu\nu\rho}(q_0, q'_0) \equiv \frac{1}{i} \int \frac{d^4 l}{(2\pi)^4} \frac{1}{(l+q)^2 - m^2 + i\epsilon} \frac{1}{-l_0 - q'_0 + i\epsilon} \frac{(1; l_\mu; l_\mu l_\nu; l_\mu l_\nu l_\rho)}{-l_0 + i\epsilon}, \quad (\text{E.6})$$

$$D_{;\mu;\mu\nu;\mu\nu\rho}(q_0, q'_0) \equiv \frac{1}{i} \int \frac{d^4 l}{(2\pi)^4} \frac{1}{(l+q)^2 - m^2 + i\epsilon} \frac{1}{-l_0 - q'_0 + i\epsilon} \frac{(1; l_\mu; l_\mu l_\nu; l_\mu l_\nu l_\rho)}{l_0 + i\epsilon}. \quad (\text{E.7})$$

The integrals can be divided depending on their subindexes being temporal or spatial. We show explicitly all the cases for the integrals  $J$ . The same definitions are used for all the other integrals. Therefore, to know any other integral one needs to replace in Eq. (E.8)  $J$  by  $A$ ,  $B$ ,  $I$ , etc.

$$J_\mu \equiv \delta_{\mu 0} J_{10} + \delta_{\mu i} J_{11} \vec{q}_i, \quad (\text{E.8})$$

$$J_{\mu\nu} \equiv \delta_{\mu 0} \delta_{\nu 0} J_{20} + (\delta_{\mu 0} \delta_{\nu i} + \delta_{\mu i} \delta_{\nu 0}) J_{21} \vec{q}_i + \delta_{\mu i} \delta_{\nu j} (J_{22} \delta_{ij} + J_{23} \vec{q}_i \vec{q}_j), \quad (\text{E.9})$$

$$\begin{aligned} J_{\mu\nu\rho} \equiv & \delta_{\mu 0} \delta_{\nu 0} \delta_{\rho 0} J_{30} + \delta \delta \delta_{\{\mu\nu\rho 00i\}} \vec{q}_i J_{31} + \delta \delta \delta_{\{\mu\nu\rho 0ij\}} (\delta_{ij} J_{32} + \vec{q}_i \vec{q}_j J_{33}) \\ & + \delta_{\mu i} \delta_{\nu j} \delta_{\rho k} (\delta \vec{q}_{\{ijk\}} J_{34} + \vec{q}_i \vec{q}_j \vec{q}_k J_{35}), \end{aligned} \quad (\text{E.10})$$

$$\begin{aligned} J_{\mu\nu\rho\sigma} \equiv & \delta_{\mu 0} \delta_{\nu 0} \delta_{\rho 0} \delta_{\sigma 0} J_{40} + \delta \delta \delta \delta_{\{\mu\nu\rho\sigma 000i\}} \vec{q}_i J_{41} + \delta \delta \delta \delta_{\{\mu\nu\rho\sigma 00ij\}} (\delta_{ij} J_{42} + \vec{q}_i \vec{q}_j J_{43}) \\ & + \delta \delta \delta \delta_{\{\mu\nu\rho\sigma 0ijk\}} (\delta \vec{q}_{\{ijk\}} J_{44} + \vec{q}_i \vec{q}_j \vec{q}_k J_{45}) \\ & + \delta_{\mu i} \delta_{\nu j} \delta_{\rho k} \delta_{\sigma l} (\delta \delta_{\{ijkl\}} J_{46} + \delta \vec{q}_{\{ijkl\}} J_{47} + \vec{q}_i \vec{q}_j \vec{q}_k \vec{q}_l J_{48}). \end{aligned} \quad (\text{E.11})$$

All coefficients  $J_{10}$ ,  $J_{11}$ , etc. have been written explicitly as functions of  $I$ ,  $J$ ,  $K$ , which can be integrated numerically, and the other simpler functions. The following definitions have been employed:

$$\delta \vec{q}_{\{ijk\}} = \delta_{ij} \vec{q}_k + \delta_{ik} \vec{q}_j + \delta_{jk} \vec{q}_i, \quad (\text{E.12})$$

$$\delta \vec{q} \vec{q}_{\{ijkl\}} = \delta_{ij} \vec{q}_k \vec{q}_l + \delta_{ik} \vec{q}_j \vec{q}_l + \delta_{il} \vec{q}_j \vec{q}_k + \delta_{jk} \vec{q}_i \vec{q}_l + \delta_{jl} \vec{q}_i \vec{q}_k + \delta_{kl} \vec{q}_i \vec{q}_j, \quad (\text{E.13})$$

$$\delta \delta_{\{ijkl\}} = \delta_{ij} \delta_{kl} + \delta_{ik} \delta_{jl} + \delta_{il} \delta_{jk}. \quad (\text{E.14})$$

The other quantities,  $\delta \delta \delta_{\{\mu\nu\rho 00i\}}$ ,  $\delta \delta \delta_{\{\mu\nu\rho 0ij\}}$ , etc, are not meant to be contracted with the indexes  $i$ ,  $j$ , and  $k$  appearing in the rest of the expressions. They only indicate how many of the indexes  $\mu$ ,  $\nu$ ,  $\rho$ , and  $\sigma$  must be temporal and how many spatial. It does not matter the order in which 0,  $i$ ,  $j$ , and  $k$  are assigned to  $\mu$ ,  $\nu$ ,  $\rho$ , and  $\sigma$ , since all the integrals  $J_{\mu\nu}$ ,  $J_{\mu\nu\rho}$ , etc, are symmetric with respect to these indexes. For example

$$J_{00i} = J_{0i0} = J_{i00} = \vec{q}_i J_{31}. \quad (\text{E.15})$$

## E.2 Results for the master integrals

We have regularized the master integrals via dimensional regularization, where the integrals depend on the momentum dimension  $D_\eta$ , or more specifically, on the parameter  $\eta$ ,

defined through  $D_\eta = 4 - \eta$ , and on the renormalization scale  $\mu$ , for which we have taken  $\mu = m_\pi$ . In the following we use,

$$R = -\frac{2}{\eta} - 1 + \gamma - \ln(4\pi), \quad (\text{E.16})$$

$$q_0'' = q_0' - q_0. \quad (\text{E.17})$$

The integrals  $A(m)$ ,  $A(q_0, q_0')$  and  $B(q_0, |\vec{q}|)$  appear, for example, in [117]. We have checked that both results coincide. It is important to maintain the  $-ie$  prescription, otherwise the integrals may give a wrong result. We take it into account by replacing  $q_0' \rightarrow q_0' - ie$  when evaluating the integrals.

### E.2.1 $A(m)$ , $A(q_0, q_0')$ and $B(q_0, \vec{q})$

We have,

$$A(m) = -\frac{1}{8\pi^2}m^2 \left( \frac{1}{2}R + \log\left(\frac{m}{\mu}\right) \right), \quad (\text{E.18})$$

$$\begin{aligned} A(q_0, q_0') = & -\frac{q_0''}{8\pi^2} \left[ \pi \frac{\sqrt{m^2 - q_0''^2}}{q_0''} + 1 - R - 2 \log\left(\frac{m}{\mu}\right) \right. \\ & \left. - \frac{2}{q_0''} \sqrt{(m^2 - q_0''^2)} \arctan\left(\frac{q_0''}{\sqrt{m^2 - q_0''^2}}\right) \right], \end{aligned} \quad (\text{E.19})$$

$$B(q_0, \vec{q}) = -\frac{1}{16\pi^2} \left[ -1 + R + 2 \log\left(\frac{m}{\mu}\right) + 2L(|q|) \right], \quad (\text{E.20})$$

with

$$L(|q|) \equiv \frac{w}{|q|} \log\left(\frac{w + |q|}{2m}\right), \quad (\text{E.21})$$

$w \equiv \sqrt{4m^2 + |q|^2}$ ,  $|q| \equiv \sqrt{\vec{q}^2 - q_0^2}$ , and  $q^2 \equiv q_0^2 - \vec{q}^2 \leq 0$ .

### E.2.2 $C(q_0, q_0')$ and $D(q_0, q_0')$

$$C(q_0, q_0') = \frac{1}{8\pi^2 q_0'} \left[ \pi(v - v'') + q_0'(-1 + R) + 2v \arctan\left(\frac{q_0}{v}\right) - 2v'' \arctan\left(\frac{q_0''}{v''}\right) \right], \quad (\text{E.22})$$

with  $v \equiv \sqrt{m^2 - q_0^2}$  and  $v'' \equiv \sqrt{m^2 - q_0''^2}$ .

$$D(q_0, q_0') = -C(q_0, q_0') + \frac{1}{q_0'} \frac{1}{4\pi} \sqrt{m^2 - q_0^2}. \quad (\text{E.23})$$

**E.2.3**  $I(q_0, |\vec{q}|, q'_0)$ 

$$I(q_0, q, q'_0) = -\frac{1}{8\pi^2} \int_0^1 dx \int_0^1 dy \left[ \frac{\pi}{2} \frac{1}{\sqrt{s_x}} - \frac{3}{4} y^{-\frac{1}{2}} (1-y) C'_q \frac{1}{s_{xy}} + \frac{1}{2} y^{\frac{1}{2}} (1-y) C'^3_q \frac{1}{s_{xy}^2} \right], \quad (\text{E.24})$$

with  $C'_q = -q_0(1-x) + q'_0$ ,  $s_x \equiv -q^2 x (1-x) - (q'_0 - q_0 + q_0 x)^2 + m_\pi^2$ , and  $s_{xy} \equiv -q^2 x (1-x) - (q'_0 - q_0 + q_0 x)^2 (1-y) + m_\pi^2$ .

**E.2.4**  $J(q_0, |\vec{q}|, q'_0)$  and  $K(q_0, |\vec{q}|, q'_0)$ 

$$\begin{aligned} J = & -\frac{1}{8\pi^2} \int_0^1 dx \int_0^1 dy y(1-y) \left\{ \left( -C'^3_q - C'^2_q C_q - C'_q C_q^2 - C_q^3 + 2s_x(C'_q + C_q) \right) \frac{3\pi}{8s_{xy}^{\frac{5}{2}}} \right. \\ & + (C'_q + C_q) \frac{\pi}{8s_{xy}^{\frac{3}{2}}} + \frac{105}{16} \int_0^1 dz z^3 \sqrt{1-z} \left[ -\frac{3}{s_{xyz}} + (C'^2_q - 5C'_q C_q + C_q^2 - 9s_x) \frac{2}{7s_{xyz}^2} \right. \\ & + (-9s_x^2 + 2s_x(C'^2_q - 5C'_q C_q + C_q^2)) + 3C'^3_q C_q + C'^2_q C_q^2 + 3C'_q C_q^3 \frac{8}{35s_{xyz}^3} \\ & + (-3s_x^3 + s_x^2(C'^2_q - 5C'_q C_q + C_q^2)) \\ & \left. \left. + s_x (3C'^3_q C_q + C'^2_q C_q^2 + 3C'_q C_q^3) - C'^3_q C_q^3 \frac{16}{35s_{xyz}^4} \right] \right\}, \end{aligned} \quad (\text{E.25})$$

with  $C_q \equiv -q_0(1-x)$ ,  $C'_q \equiv -q_0(1-x) + q'_0$ ,  $s_x \equiv -q^2 x (1-x) + m_\pi^2$ ,  $s_{xy} \equiv s_x - C_q^2 + y(C_q^2 - C'^2_q)$ , and  $s_{xyz} \equiv s_x + z \cdot y(C_q^2 - C'^2_q) - zC_q^2$ .

$$K = -J + \frac{1}{8\pi q'_0} \int_0^1 dx \frac{1}{\sqrt{m^2 + (1-x)(\vec{q}^2 x - q_0^2)}}. \quad (\text{E.26})$$

**E.3 Results for the master integrals with  $q_0 = q'_0 = 0$** 

$$A(m) = -\frac{1}{8\pi^2} m^2 \left( \frac{1}{2} R + \log \left( \frac{m}{\mu} \right) \right), \quad (\text{E.27})$$

$$A(0, 0) = -\frac{m}{8\pi}, \quad (\text{E.28})$$

$$B(0, \vec{q}) = -\frac{1}{16\pi^2} \left[ -1 + R + 2 \log \left( \frac{m}{\mu} \right) + 2L(q) \right], \quad (\text{E.29})$$

$$C(0, 0) = -\frac{1}{4\pi^2} \left( -\frac{R}{2} - \frac{1}{2} - \log \left( \frac{m}{\mu} \right) \right), \quad (\text{E.30})$$

$$I(0, \vec{q}, 0) = -\frac{1}{4\pi} At(q), \quad (\text{E.31})$$

$$J(0, \vec{q}, 0) = \frac{1}{2\pi^2 \vec{q}^2} L(q), \quad (\text{E.32})$$

where  $L(q)$  and  $At(q)$  are defined with

$$At(q) \equiv \frac{1}{2q} \arctan \left( \frac{q}{2m_\pi} \right), \quad (\text{E.33})$$

$$L(q) \equiv \frac{\sqrt{4m_\pi^2 + q^2}}{q} \log \left( \frac{\sqrt{4m_\pi^2 + q^2} + q}{2m_\pi} \right). \quad (\text{E.34})$$

## E.4 Relations between master integrals

### E.4.1 $A_\mu(q_0, q'_0)$

$$A_{10} = -A(m) - q'_0 A, \quad (\text{E.35})$$

$$A_{11} = -A. \quad (\text{E.36})$$

### E.5 $A_{\mu\nu}(q, q')$

$$A_{20} = \left[ (q_0 + q'_0)A(m) + q'^2 A \right], \quad (\text{E.37})$$

$$A_{21} = A(m) + q'_0 A, \quad (\text{E.38})$$

$$A_{22} = \frac{1}{D_\eta - 1} \left[ q''_0 A(m) + (q''^2 - m^2) A \right], \quad (\text{E.39})$$

$$A_{23} = A. \quad (\text{E.40})$$

### E.5.1 $B_\mu(q)$

$$B_{10} = -\frac{q_0}{2} B, \quad (\text{E.41})$$

$$B_{11} = -\frac{1}{2} B. \quad (\text{E.42})$$

**E.5.2**  $B_{\mu\nu}(q)$ 

$$B_{20} = \frac{1}{2(D_\eta - 1)q^2} \left[ (q^2 + q_0^2(D_\eta - 2))A(m) - \left( 2\bar{q}^2m^2 + \frac{1}{2}q^2(q^2 - D_\eta q_0^2) \right) B \right], \quad (\text{E.43})$$

(E.44)

$$B_{21} = \frac{q_0}{2(D_\eta - 1)q^2} \left[ (D_\eta - 2)A(m) + \left( \frac{D_\eta}{2}q^2 - 2m^2 \right) B \right], \quad (\text{E.45})$$

(E.46)

$$B_{22} = -\frac{1}{2(D_\eta - 1)} \left[ A(m) + \left( 2m^2 - \frac{q^2}{2} \right) B \right], \quad (\text{E.47})$$

(E.48)

$$B_{23} = \frac{1}{2(D_\eta - 1)q^2} \left[ (D_\eta - 2)A(m) + \left( \frac{D_\eta}{2}q^2 - 2m^2 \right) B \right]. \quad (\text{E.49})$$

**E.5.3**  $C_\mu(q_0, q'_0)$ 

$$C_{10} = -A, \quad (\text{E.50})$$

$$C_{11} = -C. \quad (\text{E.51})$$

**E.5.4**  $C_{\mu\nu}(q_0, q'_0)$ 

$$C_{20} = -A_{10}, \quad (\text{E.52})$$

$$C_{21} \equiv -A_{11}, \quad (\text{E.53})$$

$$C_{22} = \frac{1}{D_\eta - 1} (C_{20} + 2q_0 C_{10} + (q_0^2 - m^2)C), \quad (\text{E.54})$$

$$C_{23} = C. \quad (\text{E.55})$$

**E.5.5**  $C_{\mu\nu\rho}(q_0, q'_0)$ 

$$C_{30} = -A_{20}, \quad (\text{E.56})$$

$$C_{31} = -A_{21}, \quad (\text{E.57})$$

$$C_{32} = -A_{22}, \quad (\text{E.58})$$

$$C_{33} = -A_{23}, \quad (\text{E.59})$$

$$C_{34} \equiv -C_{22}, \quad (\text{E.60})$$

$$C_{35} = -6C_{11} - 3C_{23} - 4C. \quad (\text{E.61})$$

**E.5.6**  $D_\mu(q_0, q'_0)$ 

$$D_{10} = A, \quad (\text{E.62})$$

$$D_{11} = -D. \quad (\text{E.63})$$

**E.5.7**  $D_{\mu\nu}(q_0, q'_0)$ 

$$D_{20} \equiv A_{10}, \quad (\text{E.64})$$

$$D_{21} \equiv A_{11}, \quad (\text{E.65})$$

$$D_{22} = \frac{1}{D_\eta - 1} (D_{20} + 2q_0 D_{10} + (q_0^2 - m^2) D), \quad (\text{E.66})$$

$$D_{23} = D. \quad (\text{E.67})$$

**E.5.8**  $D_{\mu\nu\rho}(q_0, q'_0)$ 

$$D_{30} \equiv A_{20}, \quad (\text{E.68})$$

$$D_{31} \equiv A_{21}, \quad (\text{E.69})$$

$$D_{32} \equiv A_{20}, \quad (\text{E.70})$$

$$D_{33} \equiv A_{21}, \quad (\text{E.71})$$

$$D_{34} \equiv -D_{22}, \quad (\text{E.72})$$

$$D_{35} \equiv -6D_{11} - 3D_{23} - 4D. \quad (\text{E.73})$$

**E.5.9**  $I_\mu$ 

$$I_{10} = -B - q'_0 I, \quad (\text{E.74})$$

$$I_{11} = \frac{1}{2\vec{q}^2} [-A(0, q'_0, r_0) + A - 2q_0 B + (q_0^2 - \vec{q}^2 - 2q_0 q'_0) I]. \quad (\text{E.75})$$

**E.5.10**  $I_{\mu\nu}$ 

$$I_{20} = -B_{10} - q'_0 I_{10}, \quad (\text{E.76})$$

$$I_{21} = -B_{11} - q'_0 I_{11}, \quad (\text{E.77})$$

$$I_{22} = \frac{1}{(D_\eta - 2)\vec{q}^2} \left[ -I_{(\vec{l}\cdot\vec{q})^2} + \vec{q}^2 I_{(\vec{l}^2)} \right], \quad (\text{E.78})$$

$$I_{23} = \frac{1}{(D_\eta - 2)\vec{q}^4} \left[ (D_\eta - 1) I_{(\vec{l}\cdot\vec{q})^2} - \vec{q}^2 I_{(\vec{l}^2)} \right]. \quad (\text{E.79})$$

$$I_{(\vec{l}^2)} = -A(q, q') - m^2 I_0 - B_{10} - q'_0 I_{10}, \quad (\text{E.80})$$

$$I_{(\vec{l}\cdot\vec{q})^2} = \frac{1}{2} \vec{q}^2 [A_{11}(q, q') - 2q_0 B_{11} + (q^2 - 2q_0 q'_0) I_{11}]. \quad (\text{E.81})$$

**E.5.11**  $I_{\mu\nu\rho}$ 

$$I_{30} = -B_{20} - q'_0 I_{20}, \quad (\text{E.82})$$

$$I_{31} = -B_{21} - q'_0 I_{21}, \quad (\text{E.83})$$

$$I_{32} = -B_{22} - q'_0 I_{22}, \quad (\text{E.84})$$

$$I_{33} = -B_{23} - q'_0 I_{23}, \quad (\text{E.85})$$

$$I_{34} = \frac{-I_{(\vec{l}\cdot\vec{q})^3} + \vec{q}^2 I_{(\vec{l}\cdot\vec{q})\vec{l}^2}}{\vec{q}^4(D_\eta - 2)}, \quad (\text{E.86})$$

$$I_{35} = \frac{(D_\eta + 1)I_{(\vec{l}\cdot\vec{q})^3} - 3\vec{q}^2 I_{(\vec{l}\cdot\vec{q})\vec{l}^2}}{\vec{q}^6(D_\eta - 2)}. \quad (\text{E.87})$$

$$\begin{aligned} I_{(\vec{l}\cdot\vec{q})^3} = & \frac{1}{2}\vec{q}^2 \left[ -A_{22}(0, q'_0) - \vec{q}^2 A_{23}(0, q'_0) - \vec{q}^2 A(0, q'_0) - 2\vec{q}^2 A_{11}(0, q'_0) A_{22} + \vec{q}^2 A_{23}, \right. \\ & \left. + q^2 I_{22} + q^2 \vec{q}^2 I_{23} - 2q_0 B_{22} - 2q_0 \vec{q}^2 B_{23} - 2q_0 q'_0 I_{22} - 2q_0 q'_0 \vec{q}^2 I_{23} \right], \end{aligned} \quad (\text{E.88})$$

$$I_{(\vec{l}\cdot\vec{q})\vec{l}^2} = \vec{q}^2 (-A_{11} - m^2 I_{11} - B_{21} - q'_0 I_{21}). \quad (\text{E.89})$$

**E.5.12**  $J_\mu$ 

$$J_{10} \equiv -I, \quad (\text{E.90})$$

$$J_{11} \equiv \frac{1}{2\vec{q}^2} \left[ -C(0, q'_0) + C - 2q_0 I + q^2 J \right]. \quad (\text{E.91})$$

**E.5.13**  $J_{\mu\nu}$ 

$$J_{20} \equiv -I_{10}, \quad (\text{E.92})$$

$$J_{21} \equiv -I_{11}, \quad (\text{E.93})$$

$$J_{22} \equiv \frac{1}{(D_\eta - 2)\vec{q}^2} \left[ -J_{(\vec{l}\cdot\vec{q})^2} + \vec{q}^2 J_{(\vec{l}^2)} \right], \quad (\text{E.94})$$

$$J_{23} \equiv \frac{1}{(D_\eta - 2)\vec{q}^4} \left[ (D_\eta - 1)J_{(\vec{l}\cdot\vec{q})^2} - \vec{q}^2 J_{(\vec{l}^2)} \right]. \quad (\text{E.95})$$

$$J_{(\vec{l}^2)} = -C - m^2 J - I_{10}, \quad (\text{E.96})$$

$$J_{(\vec{l}\cdot\vec{q})^2} = \frac{1}{2} [C_{11} + q^2 J_{11} - 2q_0 I_{11}] \vec{q}^2. \quad (\text{E.97})$$

**E.5.14**  $J_{\mu\nu\rho}$ 

$$J_{30} \equiv -I_{20}, \quad (\text{E.98})$$

$$J_{31} \equiv -I_{21}, \quad (\text{E.99})$$

$$J_{32} \equiv -I_{22}, \quad (\text{E.100})$$

$$J_{33} \equiv -I_{23}, \quad (\text{E.101})$$

$$J_{34} \equiv \frac{-J_{(\vec{l}\cdot\vec{q})^3} + \vec{q}^2 J_{(\vec{l}\cdot\vec{q})\vec{l}^2}}{\vec{q}^4(D_\eta - 2)}, \quad (\text{E.102})$$

$$J_{35} \equiv \frac{(D_\eta + 1)J_{(\vec{l}\cdot\vec{q})^3} - 3\vec{q}^2 J_{(\vec{l}\cdot\vec{q})\vec{l}^2}}{\vec{q}^6(D_\eta - 2)}. \quad (\text{E.103})$$

$$J_{(\vec{l}\cdot\vec{q})^3} = \frac{\vec{q}^2}{2} [-C_{20}(0, q'_0) - \vec{q}^2 C_{21}(0, q'_0) - \vec{q}^2 C(0, q'_0) - 2\vec{q}^2 C_{11}(0, q'_0)] \quad (\text{E.104})$$

$$+ C_{20} + C_{21}\vec{q}^2 + q^2(J_{22} + J_{23}\vec{q}^2) - 2q_0(I_{22} + I_{23}\vec{q}^2)],$$

$$J_{(\vec{l}\cdot\vec{q})\vec{l}^2} = -\vec{q}^2 [C_{11} + m^2 J_{11} + I_{21}]. \quad (\text{E.105})$$

**E.5.15**  $J_{\mu\nu\rho\sigma}$ 

$$J_{40} \equiv -I_{30}, \quad (\text{E.106})$$

$$J_{41} \equiv -I_{31}, \quad (\text{E.107})$$

$$J_{42} \equiv -I_{32}, \quad (\text{E.108})$$

$$J_{43} \equiv -I_{33}, \quad (\text{E.109})$$

$$J_{44} \equiv -I_{34}, \quad (\text{E.110})$$

$$J_{45} \equiv -I_{35}, \quad (\text{E.111})$$

$$J_{46} = 2 \frac{-J_{\vec{l}^2(\vec{l}\cdot\vec{q})^2} + \vec{q}^2 J_{\vec{l}^4}}{\vec{q}^2(D - 2)(2D + 3)}, \quad (\text{E.112})$$

$$J_{47} = \frac{-(2D + 3)J_{(\vec{l}\cdot\vec{q})^4} + 2(2 + D)\vec{q}^2 J_{\vec{l}^2(\vec{l}\cdot\vec{q})^2} - \vec{q}^4 J_{\vec{l}^4}}{\vec{q}^6(D - 2)(2D + 3)}, \quad (\text{E.113})$$

$$J_{48} = \frac{(D + 4)J_{(\vec{l}\cdot\vec{q})^4} - 6\vec{q}^2 J_{\vec{l}^2(\vec{l}\cdot\vec{q})^2}}{\vec{q}^8(D - 2)}. \quad (\text{E.114})$$

$$J_{(\vec{l} \cdot \vec{q})^4} = \frac{\vec{q}^4}{2} [3C_{34} + \vec{q}^2 C_{35} + q^2(3J_{34} + \vec{q}^2 J_{35}) - 2q_0(3I_{34} + \vec{q}^2 I_{35})] , \quad (\text{E.115})$$

$$J_{\vec{l}^2(\vec{l} \cdot \vec{q})^2} = -\vec{q}^2 [C_{22} + \vec{q}^2 C_{23} + m^2(J_{22} + J_{23}\vec{q}^2) + I_{32} + \vec{q}^2 I_{33}] , \quad (\text{E.116})$$

$$\begin{aligned} J_{\vec{l}^4} = & -(C_{22}(D_\eta - 1) + C_{23}\vec{q}^2) - m^2(J_{22}(D_\eta - 1) + J_{23}\vec{q}^2) \\ & - (I_{32}(D_\eta - 1) + I_{33}\vec{q}^2) . \end{aligned} \quad (\text{E.117})$$

### E.5.16 $K_\mu$

$$K_{10} = I , \quad (\text{E.118})$$

$$K_{11} \equiv \frac{1}{2\vec{q}^2} [-D(0, q'_0) + D + q^2 K + 2q_0 I] . \quad (\text{E.119})$$

### E.5.17 $K_{\mu\nu}$

For the first two cases we apply the following tricks,

$$K_{20} \equiv I_{10} , \quad (\text{E.120})$$

$$K_{21} \equiv I_{11} , \quad (\text{E.121})$$

$$K_{22} \equiv \frac{1}{(D_\eta - 2)\vec{q}^2} [-K_{(\vec{l} \cdot \vec{q})^2} + \vec{q}^2 K_{(\vec{l}^2)}] , \quad (\text{E.122})$$

$$K_{23} \equiv \frac{1}{(D_\eta - 2)\vec{q}^4} [(D_\eta - 1)K_{(\vec{l} \cdot \vec{q})^2} - \vec{q}^2 K_{(\vec{l}^2)}] . \quad (\text{E.123})$$

Giving the following results,

$$K_{(\vec{l}^2)} = -D - m^2 K + I_{10} - r_0 K_{10} , \quad (\text{E.124})$$

$$K_{(\vec{l} \cdot \vec{q})^2} = \frac{1}{2} [D_{11} + q^2 K_{11} + 2q_0 I_{11}] \vec{q}^2 . \quad (\text{E.125})$$

### E.5.18 $K_{\mu\nu\rho}$

$$K_{30} \equiv I_{20} , \quad (\text{E.126})$$

$$K_{31} \equiv I_{21} , \quad (\text{E.127})$$

$$K_{32} \equiv I_{22} , \quad (\text{E.128})$$

$$K_{33} \equiv I_{23} , \quad (\text{E.129})$$

$$K_{34} = \frac{-K_{(\vec{l} \cdot \vec{q})^3} + \vec{q}^2 K_{(\vec{l} \cdot \vec{q})\vec{l}^2}}{\vec{q}^4(D_\eta - 2)} , \quad (\text{E.130})$$

$$K_{35} \equiv \frac{(D_\eta + 1)K_{(\vec{l} \cdot \vec{q})^3} - 3\vec{q}^2 K_{(\vec{l} \cdot \vec{q})\vec{l}^2}}{\vec{q}^6(D_\eta - 2)} . \quad (\text{E.131})$$

$$K_{(\vec{l}\cdot\vec{q})^3} = \frac{\vec{q}^2}{2} \left[ -D_{22}(0, q'_0) - \vec{q}^2 D_{23}(0, q'_0) - \vec{q}^2 D(0, q'_0) - 2\vec{q}^2 D_{11}(0, q'_0) + D_{22} + \vec{q}^2 D_{23} + q^2(K_{22} + K_{23}\vec{q}^2) + 2q_0(I_{22} + I_{23}\vec{q}^2) \right], \quad (\text{E.132})$$

$$K_{(\vec{l}\cdot\vec{q})\vec{l}^2} = -\vec{q}^2 [D_{11} + m^2 K_{11} - I_{21} + r_0 K_{21}]. \quad (\text{E.133})$$

### E.5.19 $K_{\mu\nu\rho\sigma}$

$$K_{40} \equiv I_{30}, \quad (\text{E.134})$$

$$K_{41} \equiv I_{31}, \quad (\text{E.135})$$

$$K_{42} \equiv I_{32}, \quad (\text{E.136})$$

$$K_{43} \equiv I_{33}, \quad (\text{E.137})$$

$$K_{44} \equiv I_{34}, \quad (\text{E.138})$$

$$K_{45} \equiv I_{35}, \quad (\text{E.139})$$

$$K_{46} = 2 \frac{-K_{\vec{l}^2(\vec{l}\cdot\vec{q})^2} + \vec{q}^2 K_{\vec{l}^4}}{\vec{q}^2(D-2)(2D+3)}, \quad (\text{E.140})$$

$$K_{47} = \frac{-(2D+3)K_{(\vec{l}\cdot\vec{q})^4} + 2(2+D)\vec{q}^2 K_{\vec{l}^2(\vec{l}\cdot\vec{q})^2} - \vec{q}^4 K_{\vec{l}^4}}{\vec{q}^6(D-2)(2D+3)}, \quad (\text{E.141})$$

$$K_{48} = \frac{(D+4)K_{(\vec{l}\cdot\vec{q})^4} - 6\vec{q}^2 K_{\vec{l}^2(\vec{l}\cdot\vec{q})^2}}{\vec{q}^8(D-2)}. \quad (\text{E.142})$$

$$K_{(\vec{l}\cdot\vec{q})^4} = \frac{1}{2} [2D_{10}\vec{q}^4 + \vec{q}^4 D + q^2(K_{22}\vec{q}^2 + K_{23}\vec{q}^4) + 2q_0(I_{22}\vec{q}^2 + I_{23}\vec{q}^4)], \quad (\text{E.143})$$

$$K_{\vec{l}^2(\vec{l}\cdot\vec{q})^2} = -[D_{22} + D_{23}\vec{q}^2 + m^2(K_{22} + K_{23}\vec{q}^2) - I_{32} - I_{33}\vec{q}^2]\vec{q}^2, \quad (\text{E.144})$$

$$K_{\vec{l}^4} = -(D_{22}(D_\eta - 1) + D_{23}\vec{q}^2) - m^2(K_{22}(D_\eta - 1) + K_{23}\vec{q}^2) + (I_{32}(D_\eta - 1) + I_{33}\vec{q}^2). \quad (\text{E.145})$$



## Appendix F

# Lagrangians for the one-meson-exchange potentials

The weak and strong vertices entering the one-pion-exchange (OPE) amplitude are:

$$\mathcal{L}_{\Lambda N \pi}^W = -i G_F m_\pi^2 \bar{\psi}_N (A_\pi + B_\pi \gamma_5) \vec{\tau} \vec{\phi}^\pi \psi_\Lambda \begin{pmatrix} 0 \\ 1 \end{pmatrix}, \quad (\text{F.1})$$

$$\mathcal{L}_{NN\pi}^S = -i g_{NN\pi} \bar{\psi}_N \gamma_5 \vec{\tau} \vec{\phi}^\pi \psi_N, \quad (\text{F.2})$$

where  $G_F m_\pi^2 = 2.21 \times 10^{-7}$  is the weak coupling constant, and  $A_\pi$  and  $B_\pi$ , empirical constants adjusted to the observables of the free  $\Lambda$  decay, which determine the strength of the parity-violating and parity-conserving amplitudes, respectively. The nucleon,  $\Lambda$ , and pion fields are given by  $\psi_N$ ,  $\psi_\Lambda$ , and  $\vec{\phi}^\pi$ , respectively, while the isospin spurion  $\begin{pmatrix} 0 \\ 1 \end{pmatrix}$  is included to enforce the empirical  $\Delta T = 1/2$  rule observed in the decay of a free  $\Lambda$ . The Bjorken and Drell convention for the definition of  $\gamma_5$  [118] is taken.

For the exchange of the pseudoscalar  $\eta$  and  $K$  mesons, the strong and weak vertices are (weak constants are given in units of  $G_F m_\pi^2$ ) :

$$\mathcal{L}_{NN\eta}^S = -i g_{NN\eta} \bar{\psi}_N \gamma_5 \phi^\eta \psi_N \quad (\text{F.3})$$

$$\mathcal{L}_{\Lambda N \eta}^W = -i \bar{\psi}_N (A_\eta + B_\eta \gamma_5) \phi^\eta \psi_\Lambda \begin{pmatrix} 0 \\ 1 \end{pmatrix}, \quad (\text{F.4})$$

$$\mathcal{L}_{\Lambda N K}^S = -i g_{\Lambda N K} \bar{\psi}_N \gamma_5 \phi^K \psi_\Lambda, \quad (\text{F.5})$$

$$\mathcal{L}_{NNK}^W = -i [\bar{\psi}_N \begin{pmatrix} 0 \\ 1 \end{pmatrix} (C_K^{PV} + C_K^{PC} \gamma_5) (\phi^K)^\dagger \psi_N + \bar{\psi}_N \psi_N (D_K^{PV} + D_K^{PC} \gamma_5) (\phi^K)^\dagger \begin{pmatrix} 0 \\ 1 \end{pmatrix}], \quad (\text{F.6})$$

where the weak coupling constants cannot be taken directly from experiment.

The weak  $\Lambda N \rho$ ,  $\Lambda N \omega$ ,  $NNK^*$ , and strong  $NN\rho$ ,  $NN\omega$ ,  $\Lambda N K^*$  vertices are given by [119]:

$$\mathcal{L}_{\Lambda N \rho}^W = -\bar{\psi}_N \left( \alpha_\rho \gamma^\mu - \beta_\rho i \frac{\sigma^{\mu\nu} q_\nu}{2M} + \varepsilon_\rho \gamma^\mu \gamma_5 \right) \vec{\tau} \vec{\rho}_\mu \psi_\Lambda \begin{pmatrix} 0 \\ 1 \end{pmatrix}, \quad (\text{F.7})$$

$$\mathcal{L}_{NN\rho}^S = -\bar{\psi}_N \left( g_{NN}^V \rho \gamma^\mu + i \frac{g_{NN}^T \rho}{2M} \sigma^{\mu\nu} q_\nu \right) \vec{\tau} \vec{\rho}_\mu \psi_N, \quad (\text{F.8})$$

$$\mathcal{L}_{NN\omega}^S = -\bar{\psi}_N \left( g_{NN\omega}^V \gamma^\mu + i \frac{g_{NN\omega}^T}{2M} \sigma^{\mu\nu} q_\nu \right) \phi_\mu^\omega \psi_N , \quad (\text{F.9})$$

$$\mathcal{L}_{\Lambda N\omega}^W = -\bar{\psi}_N \left( \alpha_\omega \gamma^\mu - \beta_\omega i \frac{\sigma^{\mu\nu} q_\nu}{2M} + \varepsilon_\omega \gamma^\mu \gamma_5 \right) \phi_\mu^\omega \psi_\Lambda \begin{pmatrix} 0 \\ 1 \end{pmatrix} , \quad (\text{F.10})$$

$$\mathcal{L}_{\Lambda NK^*}^S = -\bar{\psi}_N \left( g_{\Lambda NK^*}^V \gamma^\mu + i \frac{g_{\Lambda NK^*}^T}{2M} \sigma^{\mu\nu} q_\nu \right) \phi_\mu^{K^*} \psi_\Lambda , \quad (\text{F.11})$$

$$\begin{aligned} \mathcal{L}_{NNK^*}^W = & - \left( C_{K^*}^{PC,V} \bar{\psi}_N \begin{pmatrix} 0 \\ 1 \end{pmatrix} (\phi_\mu^{K^*})^\dagger \gamma^\mu \psi_N + D_{K^*}^{PC,V} \bar{\psi}_N \gamma^\mu \psi_N (\phi_\mu^{K^*})^\dagger \begin{pmatrix} 0 \\ 1 \end{pmatrix} \right. \\ & + C_{K^*}^{PC,T} \bar{\psi}_N \begin{pmatrix} 0 \\ 1 \end{pmatrix} (\phi_\mu^{K^*})^\dagger (-i) \frac{\sigma^{\mu\nu} q_\nu}{2M} \psi_N + D_{K^*}^{PC,T} \bar{\psi}_N (-i) \frac{\sigma^{\mu\nu} q_\nu}{2M} \psi_N (\phi_\mu^{K^*})^\dagger \begin{pmatrix} 0 \\ 1 \end{pmatrix} \\ & \left. + C_{K^*}^{PV} \bar{\psi}_N \begin{pmatrix} 0 \\ 1 \end{pmatrix} (\phi_\mu^{K^*})^\dagger \gamma^\mu \gamma_5 \psi_N + D_{K^*}^{PV} \bar{\psi}_N \gamma^\mu \gamma_5 \psi_N (\phi_\mu^{K^*})^\dagger \begin{pmatrix} 0 \\ 1 \end{pmatrix} \right) . \end{aligned} \quad (\text{F.12})$$

# Appendix G

## One-meson-exchange parameters

In this appendix we list the strong and weak couplings as well as the form factors needed in the one-meson exchange potentials. The values for the Nijmegen Soft-Core 97f strong model are listed in Table G.1, and the ones for the Jülich strong model are listed in Table G.2.

M	Strong c.c.	Weak c.c.		$\Lambda_i$ (GeV)
		PC	PV	
$\pi$	$g_{NN\pi} = 13.16$	$B_\pi = -7.15$	$A_\pi = 1.05$	1.750
$\eta$	$g_{NN\eta} = 6.42$	$B_\eta = -11.9$	$A_\eta = 1.80$	1.750
K	$g_{\Lambda NK} = -17.66$	$C_K^{\text{PC}} = -23.70$	$C_K^{\text{PV}} = 0.76$	1.789
	$g_{N\Sigma K} = 5.38$	$D_K^{\text{PC}} = 8.33$	$D_K^{\text{PV}} = 2.09$	
$\rho$	$g_{NN\rho}^V = 2.97$	$\alpha_\rho = -3.29$	$\epsilon_\rho = 1.09$	1.232
	$g_{NN\rho}^T = 12.52$	$\beta_\rho = -6.74$		
$\omega$	$g_{NN\omega}^V = 10.36$	$\alpha_\omega = -0.17$	$\epsilon_\omega = -1.33$	1.310
	$g_{NN\omega}^T = 4.195$	$\beta_\omega = -7.43$		
K*	$g_{\Lambda NK^*}^V = -6.105$	$C_{K^*}^{\text{PC},V} = -4.02$	$C_{K^*}^{\text{PV}} = -4.48$	1.649
	$g_{\Lambda NK^*}^T = -14.85$	$C_{K^*}^{\text{PC},T} = -19.54$		
		$D_{K^*}^{\text{PC},V} = -5.46$	$D_{K^*}^{\text{PV}} = 0.60$	
		$D_{K^*}^{\text{PC},T} = 6.23$		

Table G.1: Nijmegen (NSC97f) meson exchange parameters used in the present work. The weak couplings are in units of  $G_F m_\pi^2 = 2.21 \times 10^{-7}$ .

M	Strong c.c.	Weak c.c.		$\Lambda_i$ (GeV)
		PC	PV	
$\pi$	$g_{NN\pi} = 13.45$	$B_\pi = -7.15$	$A_\pi = 1.05$	1.300
$\eta$	$g_{NN\eta} = 0$	$B_\eta = 0$	$A_\eta = 1.80$	1.300
K	$g_{\Lambda NK} = -13.48$	$C_K^{\text{PC}} = -17.67$	$C_K^{\text{PV}} = 0.76$	1.200
	$g_{N\Sigma K} = 3.55$	$D_K^{\text{PC}} = 5.50$	$D_K^{\text{PV}} = 2.09$	
$\rho$	$g_{NN\rho}^V = 3.25$	$\alpha_\rho = -3.60$	$\epsilon_\rho = 1.09$	1.400
	$g_{NN\rho}^T = 19.82$	$\beta_\rho = -9.55$		
$\omega$	$g_{NN\omega}^V = 15.85$	$\alpha_\omega = -5.85$	$\epsilon_\omega = -1.33$	1.500
	$g_{NN\omega}^T = 0$	$\beta_\omega = -10.96$		
K*	$g_{\Lambda NK^*}^V = -5.63$	$C_{K^*}^{\text{PC},V} = -3.71$	$C_{K^*}^{\text{PV}} = -4.48$	2.200
	$g_{\Lambda NK^*}^T = -18.34$	$C_{K^*}^{\text{PC},T} = -26.38$		
		$D_{K^*}^{\text{PC},V} = -5.03$	$D_{K^*}^{\text{PV}} = 0.60$	
		$D_{K^*}^{\text{PC},T} = 12.18$		

Table G.2: Same as Table G.1 but for the Jülich B model.

## Appendix H

### Low energy coefficients in terms of meson-exchange parameters

The expressions for the low energy constants appearing in the effective potential in terms of the one meson exchange parameters are the following:

$$C_{00}^{sc} = \left[ \frac{g_{\Lambda NK^*}^V}{m_{K^*}^2} \left( \frac{C_{K^*}^{PC,V}}{2} + D_{K^*}^{PC,V} \right) + \frac{g_{NN\omega}^V \alpha_\omega}{m_\omega^2} \right] m_\pi^2 , \quad (\text{H.1})$$

$$C_{00}^{vec} = \left( \frac{g_{\Lambda NK^*}^V C_{K^*}^{PC,V}}{2m_{K^*}^2} + \frac{g_{NN\rho}^V \alpha_\rho}{m_\rho^2} \right) m_\pi^2 , \quad (\text{H.2})$$

$$C_{01}^{sc} = 0 , \quad (\text{H.3})$$

$$C_{01}^{vec} = 0 , \quad (\text{H.4})$$

$$C_{10}^{sc} = 0 , \quad (\text{H.5})$$

$$C_{10}^{vec} = 0 , \quad (\text{H.6})$$

$$C_{11}^{sc} = \frac{-m_\pi^2}{2M} \frac{A_\eta g_{NN\eta}}{m_\eta^2} , \quad (\text{H.7})$$

$$C_{11}^{vec} = 0 , \quad (\text{H.8})$$

$$C_{12}^{sc} = - \frac{m_\pi^2}{2M} \left[ \frac{i(g_{\Lambda NK^*}^V + g_{\Lambda NK^*}^T) \left( \frac{C_{K^*}^{PV}}{2} + D_{K^*}^{PV} \right) m_\pi^2}{m_{K^*}^2} + \frac{i(g_{NN\omega}^V + g_{NN\omega}^T) \epsilon_\omega m_\pi^2}{m_\omega^2} \right] , \quad (\text{H.9})$$

$$C_{12}^{vec} = \frac{m_\pi^2}{2M} \left[ \frac{i(g_{\Lambda NK^*}^V + g_{\Lambda NK^*}^T) C_{K^*}^{PV} m_\pi^2}{2m_{K^*}^2} + \frac{i(g_{NN\rho}^V + g_{NN\rho}^T) \epsilon_\rho m_\pi^2}{m_\rho^2} \right], \quad (\text{H.10})$$

$$\begin{aligned} C_{20}^{sc} = & \frac{m_\pi^2}{4M\bar{M}} \left[ \left( \frac{C_{K^*}^{PC,V}}{2} + D_{K^*}^{PC,V} + \frac{C_{K^*}^{PC,T}}{2} + D_{K^*}^{PC,T} \right) \frac{g_{\Lambda NK^*}^V + g_{\Lambda NK^*}^T}{m_{K^*}^2} \right. \\ & \left. + \frac{(\alpha_\omega + \beta_\omega)(g_{NN\omega}^V + g_{NN\omega}^T)}{m_\omega^2} - \frac{B_\eta g_{NN\eta}}{m_\eta^2} \right], \end{aligned} \quad (\text{H.11})$$

$$C_{20}^{vec} = \frac{m_\pi^2}{4M\bar{M}} \left[ \frac{(C_{K^*}^{PC,V} + C_{K^*}^{PC,T})(g_{\Lambda NK^*}^V + g_{\Lambda NK^*}^T)}{2m_{K^*}^2} + \frac{(\alpha_\rho + \beta_\rho)(g_{NN\rho}^V + g_{NN\rho}^T)}{m_\rho^2} \right], \quad (\text{H.12})$$

$$\begin{aligned} C_{21}^{sc} = & -\frac{m_\pi^2}{4M\bar{M}} \left[ \left( \frac{C_{K^*}^{PC,V}}{2} + D_{K^*}^{PC,V} + \frac{C_{K^*}^{PC,T}}{2} + D_{K^*}^{PC,T} \right) \frac{g_{\Lambda NK^*}^V + g_{\Lambda NK^*}^T}{m_{K^*}^2} \right. \\ & \left. + \frac{(\alpha_\omega + \beta_\omega)(g_{NN\omega}^V + g_{NN\omega}^T)}{m_\omega^2} \right], \end{aligned} \quad (\text{H.13})$$

$$C_{21}^{vec} = -\frac{m_\pi^2}{4M\bar{M}} \left[ \frac{(C_{K^*}^{PC,V} + C_{K^*}^{PC,T})(g_{\Lambda NK^*}^V + g_{\Lambda NK^*}^T)}{2m_{K^*}^2} + \frac{(\alpha_\rho + \beta_\rho)(g_{NN\rho}^V + g_{NN\rho}^T)}{m_\rho^2} \right], \quad (\text{H.14})$$

$$C_{22}^{sc} = -2m_\pi^2 \left[ \frac{g_{\Lambda NK^*}^V (\Lambda^2 + m_{K^*}^2) \left( \frac{C_{K^*}^{PC,V}}{2} + D_{K^*}^{PC,V} \right)}{m_{K^*}^4 \Lambda^2} + \frac{g_{NN\omega}^V \alpha_\omega (\Lambda^2 + m_\omega^2)}{m_\omega^4 \Lambda^4} \right], \quad (\text{H.15})$$

$$C_{22}^{vec} = -2m_\pi^2 \left[ \frac{g_{\Lambda NK^*}^V (\Lambda^2 + m_{K^*}^2) C_{K^*}^{PV}}{2m_{K^*}^4 \Lambda^2} + \frac{g_{NN\rho}^V \alpha_\rho (\Lambda^2 + m_\rho^2)}{m_\rho^4 \Lambda^4} \right]. \quad (\text{H.16})$$

# Bibliography

- [1] M. Danysz and J. Pniewski, “Delayed disintegration of a heavy nuclear fragment,” *Phil. Mag.*, vol. 44, p. 348, 1953.
- [2] O. Hashimoto and H. Tamura, “Spectroscopy of  $\Lambda$  hypernuclei,” *Prog. Part. Nucl. Phys.*, vol. 57, pp. 564–653, 2006.
- [3] <http://www.lnf.infn.it/esperimenti/finuda/publications.html>.
- [4] <http://www.j-parc.jp>.
- [5] <http://www.fair-center.eu>.
- [6] J. Haidenbauer, K. Holinde, K. Kilian, T. Sefzick, and A. W. Thomas, “Weak strangeness production in nucleon-nucleon scattering,” *Phys. Rev. C*, vol. 52, p. 3496, 1995.
- [7] A. Parreño, A. Ramos, N. G. Kelkar, and C. Bennhold, “Weak strangeness production in  $pn \rightarrow p\Lambda$  in a one-boson-exchange model,” *Phys. Rev. C*, vol. 59, p. 2122, 1999.
- [8] T. Inoue, K. Sasaki, and M. Oka, “Study of the  $pn \rightarrow p\Lambda$  weak scattering in a quark model,” *Nucl. Phys. A*, vol. 684, pp. 478–480, 2001.
- [9] T. Kishimoto et al., “Study of weak hyperon nucleon interaction by the  $pn \rightarrow p\Lambda$  reaction,” *Nucl. Phys. A*, vol. 663-664, pp. 509c–512c, 2000.
- [10] S. Ajimura et al., “Weak production of  $\Lambda$  hyperon by the  $pn \rightarrow p\Lambda$  reaction,” *Nucl. Phys. A*, vol. 691, pp. 312–317, 2001.
- [11] W. B. Alberico and G. Garbarino, “Weak decay of  $\Lambda$ -hypernuclei,” *Phys. Rep.*, vol. 369, pp. 1–109, 2002.
- [12] H. Outa et al., “Hypernuclear weak decay experiments at KEK: n-n and n-p coincidence measurement,” *Nucl. Phys. A*, vol. 754, pp. 157–167, 2005.
- [13] Y. Sato et al., “Mesonic and nonmesonic weak decay widths of medium-heavy  $\Lambda$  hypernuclei,” *Phys. Rev. C*, vol. 71, p. 025203, 2005.
- [14] S. Bufalino, “Weak decay of  $\Lambda$  hypernuclei: Experimental status,” *Nucl. Phys. A*, vol. 914, pp. 160–169, 2013.

- [15] H. Bando, T. Motoba, and J. Zofka, “Production, structure and decay of hypernuclei,” *Phys. Rev. C*, 1990.
- [16] J. F. Dubach, G. B. Feldman, B. R. Holstein, and L. Torre, “Theory of weak hypernuclear decay,” *Annals Phys.*, vol. 249, pp. 146–179, 1996.
- [17] A. Parreño, A. Ramos, and C. Bennhold, “Weak decay of hypernuclei,” *Phys. Rev. C*, vol. 56, pp. 339–364, 1997.
- [18] D. Jido, E. Oset, and J. E. Palomar, “Meson exchange in the weak decay of  $\Lambda$  hypernuclei and the  $\Gamma_n/\Gamma_p$  ratio,” *Nucl. Phys. A*, vol. 694, pp. 525–555, 2001.
- [19] A. Parreño, A. Ramos, and A. Bennhold, “Novel weak decays in doubly strange systems,” *Phys. Rev. C*, vol. 65, p. 015205, 2002.
- [20] K. Itonaga, T. Ueda, and T. Motoba, “Nonmesonic decays and lifetimes of hypernuclei,” *Phys. Rev. C*, vol. 65, p. 034617, 2002.
- [21] A. Parreño, A. Ramos, C. Bennhold, and K. Maltman, “Violation of the  $\Delta I = 1/2$  rule in the nonmesonic weak decay of hypernuclei,” *Phys. Lett. B*, vol. 435, pp. 1–8, 1998.
- [22] W. M. Alberico and G. Garbarino, “The  $\Delta I = 1/2$  rule in non-mesonic weak decay of  $\Lambda$ -hypernuclei,” *Phys. Lett. B*, vol. 486, pp. 362–368, 2000.
- [23] W. M. Alberico, A. De Pace, M. Ericson, and A. Molinari, “Two-nucleon induced  $\lambda$  decay in nuclei,” *Phys. Lett. B*, vol. 256, pp. 134–140, 1991.
- [24] A. Ramos, E. Oset, and L. L. Salcedo, “Two nucleon induced  $\Lambda$  decay and the neutron to proton induced ratio,” *Phys. Rev. C*, vol. 50, pp. 2314–2322, 1994.
- [25] W. M. Alberico, A. De Pace, G. Garbarino, and A. Ramos, “Weak decays of medium and heavy  $\Lambda$  hypernuclei,” *Phys. Rev. C*, vol. 61, p. 044314, 2000.
- [26] W. M. Alberico, A. De Pace, G. Garbarino, and R. Cenni, “Functional approach to the non-mesonic decay of  $\Lambda$ -hypernuclei,” *Nucl. Phys. A*, vol. 668, pp. 113–133, 2000.
- [27] K. Sasaki, T. Inoue, and M. Oka, “Weak decay of  $\Lambda$  in nuclei: quarks versus mesons,” *Nucl. Phys. A*, vol. 669, pp. 331–350, 2000.
- [28] K. Sasaki, T. Inoue, and M. Oka, “Nonmesonic weak decay of light hypernuclei with coherent  $\Sigma$  mixing,” *Nucl. Phys. A*, vol. 707, pp. 477–490, 2002.
- [29] A. Parreño and A. Ramos, “Final state interactions in hypernuclear decay,” *Phys. Rev. C*, vol. 65, p. 015204, 2002.
- [30] S. Okada et al., “Neutron and proton energy spectra from the non-mesonic weak decays of  ${}^5_{\Lambda}He$  and  ${}^{12}_{\Lambda}C$ ,” *Phys. Lett. B*, vol. 597, pp. 249–256, 2004.

- [31] B. H. Kang et al., “Exclusive measurement of the nonmesonic weak decay of  ${}^5\Lambda He$  hypernucleus,” *Phys. Rev. Lett.*, vol. 96, p. 062301, 2006.
- [32] M. J. Kim et al., “Coincidence measurement of the nonmesonic weak decay of  ${}^{12}\Lambda C$ ,” *Phys. Lett. B*, vol. 641, pp. 28–33, 2006.
- [33] G. Garbarino, A. Parreño, and A. Ramos, “Towards the solution of the  $\Gamma_n/\Gamma_p$  puzzle in the nonmesonic weak decay of the  $\Lambda$  hypernuclei,” *Phys. Lett. B*, vol. 641, p. 054603, 2004.
- [34] G. Garbarino, A. Parreño, and A. Ramos, “Nucleon-nucleon coincidence spectra in the nonmesonic weak decay of  $\Lambda$  hypernuclei and the  $\Gamma_n/\Gamma_p$  puzzle,” *Phys. Rev. Lett.*, vol. 91, p. 112501, 2003.
- [35] E. Bauer, G. Garbarino, A. Parreño, and A. Ramos, “Single and double coincidence nucleon spectra in the weak decay of  $\Lambda$  hypernuclei,” *Nucl. Phys. A*, vol. 836, pp. 199–224, 2010.
- [36] D. R. Entem and R. Machleidt, “Chiral effective field theory and nuclear forces,” *Phys. Rep.*, vol. 503, pp. 1–76, 2011.
- [37] C. Gattringer and C. B. Lang, “Quantum chromodynamics on the lattice: an introductory presentation,” *Lect. Not. Phys.*, vol. 788, pp. 1–343, 2010.
- [38] S. R. Beane et al., “Hyperon-nucleon scattering from fully-dynamical lattice QCD,” *Nucl. Phys. A*, vol. 794, pp. 62–72, 2007.
- [39] S. R. Beane et al., “High statistics analysis using anisotropic clover lattices: III. baryon-baryon interactions,” *Phys. Rev. D*, vol. 81, p. 054505, 2010.
- [40] H. Nemura, N. Ishii, S. Aoki, and T. Hatsuda, “Hyperon–nucleon force from lattice QCD,” *Phys. Lett. B*, vol. 673, pp. 136–141, 2009.
- [41] H. Nemura, N. Ishii, S. Aoki, and T. Hatsuda, “Baryon-baryon interactions in the flavor SU(3) limit from full QCD simulations on the lattice,” *Prog. Theor. Phys.*, vol. 124, pp. 591–603, 2010.
- [42] J. Wasem, “Lattice QCD calculation of nuclear parity violation,” *Phys. Rev. C*, vol. 85, p. 022501, 1012.
- [43] S. Weinberg, “Nuclear forces from chiral lagrangians,” *Phys. Lett. B*, vol. 251, pp. 288–292, 1990.
- [44] S. Weinberg, “Nuclear forces from chiral lagrangians,” *Nucl. Phys. B*, vol. 363, pp. 3–18, 1991.
- [45] C. Ordoñez, L. Ray, and U. van Kolck, “Nucleon-nucleon potential from an effective chiral lagrangian,” *Phys. Rev. Lett.*, vol. 71, pp. 1982–1985, 1994.

- [46] D. R. Entem and R. Machleidt, “Accurate charge-dependent nucleon-nucleon potential at fourth order of chiral perturbation theory,” *Phys. Rev. C*, vol. 68, p. 041001, 2003.
- [47] E. Epelbaum, W. Glöckle, and U. Meiñner, “The two-nucleon system at next-to-next-to-next-to-leading order,” *Nucl. Phys. A*, vol. 747, pp. 362–424, 2005.
- [48] E. Epelbaum and U. G. Meiñner, “Chiral dynamics of few- and many-nucleon systems,” *Ann. Rev. Nucl. Part. Sci.*, vol. 62, pp. 159–185, 2012.
- [49] S.-L. Zhu, C. M. Maekawa, B. Holstein, M. Ramsey-Musolf, and U. van Kolck, “Nuclear parity violation in effective field theory,” *Nucl. Phys. A*, vol. 748, pp. 435–498, 2005.
- [50] M. J. Savage and M. B. Wise, “Hyperon masses in nuclear matter,” *Phys. Rev. D*, vol. 53, pp. 349–354, 1996.
- [51] C. L. Korpa, A. E. L. Dieperink, and R. G. E. Timmermans, “Hyperon-nucleon scattering and hyperon masses in the nuclear medium,” *Phys. Rev. C*, vol. 65, p. 015208, 2001.
- [52] H. W. Hammer, “The hypertriton in effective field theory,” *Nucl. Phys. A*, vol. 705, pp. 173–189, 2002.
- [53] S. R. Beane, P. F. Bedaque, A. Parreñó, and M. J. Savage, “A framework for exploring the interactions and decays of hyperons with lattice QCD,” *Nucl. Phys. A*, vol. 747, pp. 55–74, 2005.
- [54] H. Polinder, J. Haidenbauer, and U. G. Meiñner, “Hyperon–nucleon interactions—a chiral effective field theory approach,” *Nucl. Phys. A*, vol. 779, pp. 244–266, 2006.
- [55] J. Haidenbauer, S. Petschauer, N. Kaiser, U. G. Meiñner, A. Nogga, and W. Weise, “Hyperon-nucleon interaction at next-to-leading order in chiral effective field theory,” *Nucl. Phys. A*, vol. 915, pp. 24–58, 2013.
- [56] J.-H. Jun, “Four baryon point  $\Lambda N \rightarrow NN$  interaction for the nonmesonic weak decay of hypernuclei  $^4_\Lambda H$ ,  $^4_\Lambda He$ ,  $^5_\Lambda He$  and  $^{12}_\Lambda C$ ,” *Phys. Rev. Lett.*, vol. 63, p. 044012, 2001.
- [57] A. Parreñó, C. Bennhold, and B. R. Holstein, “ $\Lambda N \rightarrow NN$  weak interaction in effective-field theory,” *Phys. Rev. C*, vol. 70, p. 051601, 2004.
- [58] A. Parreñó, C. Bennhold, and B. R. Holstein, “An EFT for the weak  $\Lambda N$  interaction,” *Nucl. Phys. A*, vol. 754, pp. 127–136, 2005.
- [59] H. Kamada and W. Glöckle, “Solutions of the yakubovsky equations for four-body model systems,” *Nucl. Phys. A*, vol. 548, pp. 205–226, 1992.
- [60] U. G. Meiñner, “Nuclear lattice simulations: status and perspectives,” *arxiv:1307.7923*, 2013.

- [61] K. Miyagawa, H. Kamada, W. Glöckle, and V. Stoks, “Properties of the bound  $\Lambda(\Sigma)NN$  system and hyperon-nucleon interactions,” *Phys. Rev. C*, vol. 51, pp. 2905–2913, 1995.
- [62] A. Nogga, H. Kamada, and W. Glöckle, “The hypernuclei  $^4_\Lambda He$  and  $^4_\Lambda H$ : Challenges for modern hyperon-nucleon forces,” *Phys. Rev. Lett.*, vol. 88, p. 127501, 2002.
- [63] S. Cohen and D. Kurath, “Spectroscopic factors for the 1p shell,” *Nucl. Phys. A*, vol. 101, pp. 1–16, 1967.
- [64] P. J. Brussaard and P. W. M. Glaudemans, *Shell model applications in nuclear spectroscopy*. North-Holland, 1977.
- [65] M. Moshinsky, “Transformation brackets for harmonic oscillator wave functions,” *Nucl. Phys.*, vol. 13, pp. 104–116, 1959.
- [66] D. Halderson, “G-matrix calculations in finite hypernuclei,” *Phys. Rev. C*, vol. 52, pp. 481–587, 1995.
- [67] M. N. Nagels, T. A. Rijken, and J. J. de Swart, “Baryon-baryon scattering in a one-boson-exchange-potential approach. II. Hyperon-nucleon scattering,” *Phys. Rev. D*, vol. 15, pp. 2547–2564, 1977.
- [68] P. M. M. Maessen, T. Rijken, and J. J. de Swart, “Soft-core baryon-baryon one-boson-exchange models. II. Hyperon-nucleon potential,” *Phys. Rev. C*, vol. 40, pp. 2226–2245, 1989.
- [69] B. Holzenkamp, K. Holinde, and J. Speth, “A meson exchange model for the hyperon-nucleon interaction,” *Nucl. Phys. A*, vol. 500, pp. 485–528, 1989.
- [70] J. J. Szymanski et al., “Nonleptonic weak decay of  $^5_\Lambda He$  and  $^{12}_\Lambda C$ ,” *Phys. Rev. C*, vol. 43, pp. 849–862, 1991.
- [71] S. Ajimura et al., “Polarization and weak decays of  $\Lambda$  hypernuclei produced by the  $(\pi^+, K^+)$  reaction on  $^{12}C$ ,” *Phys. Lett. B*, vol. 282, pp. 293–298, 1992.
- [72] A. Ramos, E. van Meijgaard, C. Bennhold, and B. K. Jennings, “Asymmetries in the weak decay of polarized hypernuclei,” *Nucl. Phys. A*, vol. 544, pp. 703–730, 1992.
- [73] C. Chumillas, G. Garbarino, A. Parreño, and A. Ramos, “Two-pion-exchange in the non-mesonic weak decay of  $\Lambda$ -hypernuclei,” *Phys. Lett. B*, vol. 657, pp. 180–186, 2007.
- [74] C. Barbero and A. Mariano, “ $\sigma$  meson exchange effect on non-mesonic hypernuclear weak decay observables,” *Phys. Rev. C*, vol. 73, p. 024309, 2006.
- [75] M. H. Partovi and E. L. Lomon, “Field-theoretical nucleon-nucleon potential,” *Phys. Rev. D*, vol. 2, pp. 1999–2032, 1970.

- [76] M. H. Partovi and E. L. Lomon, “ $\sigma$ -exchange potential for nucleon-nucleon scattering,” *Phys. Rev. D*, vol. 5, pp. 1192–1205, 1972.
- [77] A. D. Jackson, D. O. Riska, and B. Verwest, “Meson exchange model for the nucleon-nucleon interaction,” *Nucl. Phys. A*, vol. 249, pp. 397–444, 1975.
- [78] G. E. Brown and A. D. Jackson, *The nucleon-nucleon interaction*. North-Holland, 1976.
- [79] R. V. Mau, *Mesons in Nuclei, Vol I*. North-Holland, 1979.
- [80] M. Lacobme et al., “Parametrization of the paris n-n potential,” *Phys. Rev. C*, vol. 21, pp. 861–873, 1980.
- [81] R. Machleidt, “The meson theory of nuclear forces and nuclear structure,” *Adv. Nucl. Phys.*, vol. 19, pp. 189–376, 1989.
- [82] R. Machleidt, K. Holinde, and C. Elster, “The bonn meson-exchange model for the nucleon—nucleon interaction,” *Phys. Rep.*, vol. 149, pp. 1–89, 1987.
- [83] S. Weinberg, “Nonlinear realizations of chiral symmetry,” *Phys. Rev.*, vol. 166, pp. 1568–1577, 1968.
- [84] S. Coleman, J. Wess, and B. Zumino, “Structure of phenomenological lagrangians. I,” *Phys. Rev.*, vol. 177, pp. 2239–2247, 1969.
- [85] C. G. Callan, S. Coleman, J. Wess, and B. Zumino, “Structure of phenomenological lagrangians. II,” *Phys. Rev. Lett.*, vol. 177, pp. 2247–2250, 1969.
- [86] S. Weinberg, “Phenomenological lagrangians,” *Physica A*, vol. 96, pp. 327–340, 1979.
- [87] J. Gasser and H. Leutwyler, “Chiral perturbation theory to one loop,” *Annals Phys.*, vol. 158, pp. 142–210, 1984.
- [88] J. Gasser and H. Leutwyler, “Chiral perturbation theory: expansions in the mass of the strange quark,” *Nucl. Phys. B*, vol. 250, pp. 465–516, 1985.
- [89] E. Jenkins and A. Manohar, “Baryon chiral perturbation theory using a heavy fermion lagrangian,” *Phys. Lett. B*, vol. 255, pp. 558–562, 1991.
- [90] E. Epelbaum, “Nuclear physics from QCD: state of the art and open challenges,” *PoS Confinement 14*, 2012.
- [91] E. Jenkins, “Hyperon non-leptonic decays in chiral perturbation theory,” *Nucl. Phys. B*, vol. 375, pp. 561–581, 1992.
- [92] R. Springer, “Heavy baryon chiral perturbation theory and the weak nonleptonic p-wave decays of the baryon octet,” *Phys. Lett. B*, vol. 461, pp. 167–174, 1999.

- [93] J. F. Donoghue, E. Golovich, and B. R. Holstein, *Dynamics of the Standard Model*. Cambridge Univ. Press, 1992.
- [94] V. G. J. Stoks and T. A. Rijken, “Soft-core baryon-baryon potentials for the complete baryon octet,” *Phys. Rev. C*, vol. 59, pp. 3009–3020, 1999.
- [95] V. G. J. Stoks, T. A. Rijken, and Y. Yamamoto, “Soft-core hyperon-nucleon potentials,” *Phys. Rev. C*, vol. 59, pp. 21–40, 1999.
- [96] A. Nogga, “Faddeev-yakubovsky calculations for  $A = 4$  hypernuclear systems,” *Nucl. Phys. A*, vol. 754, pp. 36c–42c, 2005.
- [97] E. Oset, H. Toki, M. Mizobe, and T. T. Takahashi, “ $\sigma$  exchange in the NN interaction within the chiral unitary approach,” *Prog. Theor. Phys.*, vol. 103, pp. 351–365, 2000.
- [98] N. Kaiser, R. Brockmann, and W. Weise, “Peripheral nucleon-nucleon phase shifts and chiral symmetry,” *Nucl. Phys. A*, vol. 625, pp. 758–788, 1997.
- [99] G. Passarino and M. Veltman, “One-loop corrections for  $e^+e^-$  annihilation into  $\mu^+\mu^-$  in the weinberg model,” *Nucl. Phys. B*, vol. 160, pp. 151–207, 1979.
- [100] T. A. Rijken, M. M. Nagels, and Y. Yamamoto, “Baryon-baryon interactions—nijmegen extended-soft-core models—,” *Prog. Theor. Phys. Suppl.*, vol. 185, pp. 14–71, 2010.
- [101] S. Bufalino, “Experimental status of the weak decay of  $\Lambda$  hypernuclei,” *XI International Conference on Hypernuclear and Strange Particle Physics (HYP2012)*, 2012.
- [102] H. Noumi et al., *Proceedings of the IV International Symposium on Weak and Electromagnetic Interactions in Nuclei*. World Scientific, 1995.
- [103] S. Ajimura et al., “Asymmetry in the nonmesonic weak decay of polarized  ${}^5\Lambda$ He hypernuclei,” *Phys. Rev. Lett.*, vol. 84, pp. 4052–4055, 2000.
- [104] T. Maruta et al., “Proton asymmetry in non-mesonic weak decay of light hypernuclei,” *Nucl. Phys. A*, vol. 754, pp. 168c–172c, 2005.
- [105] H. Noumi et al., “Hypernuclear weak decay of  ${}^{12}\Lambda$ C and  ${}^{12}\Lambda$ B,” *Phys. Rev. C*, vol. 52, pp. 2936–2945, 1995.
- [106] H. Outa et al., “Mesonic and non-mesonic decay widths of  ${}^{12}\Lambda$ C,” *Nucl. Phys. A*, vol. 670, pp. 281c–284c, 2000.
- [107] J. H. Kim et al., “Neutron energy spectra from the nonmesonic weak decay of  ${}^{12}\Lambda$ C and  ${}^{89}\Lambda$ Y hypernuclei,” *Phys. Rev. C*, vol. 68, p. 065201, 2003.
- [108] [http://seal.web.cern.ch/seal/snapshot/work\\_packages/mathlibs/minuit/](http://seal.web.cern.ch/seal/snapshot/work_packages/mathlibs/minuit/).
- [109] E. Epelbaum, U. G. Meißner, W. Glöckle, and C. Elster, “Resonance saturation for four-nucleon operators,” *Phys. Rev. C*, vol. 65, p. 044001, 2002.

- [110] K. Sasaki, M. Izaki, and M. Oka, “ $\sigma$  exchange in the nonmesonic decays of light hypernuclei and violation of the  $\Delta I = 1/2$  rule,” *Phys. Rev. C*, vol. 71, p. 035502, 2005.
- [111] M. M. Block and R. H. Dalitz, “Structure of the weak interaction  $\Lambda + N \rightarrow N + N$ ,” *Phys. Rev. Lett.*, vol. 11, pp. 96–100, 1963.
- [112] J. Golak et al., “Nonmesonic weak decay of the hypertriton,” *Phys. Rev. C*, vol. 55, pp. 2196–2213, 1997.
- [113] A. Parreño, “Weak decays of hypernuclei,” *Lect. Not. Phys.*, vol. 724, pp. 141–189, 2007.
- [114] A. Pérez-Obiol, A. Parreño, and B. Juliá-Díaz, “Constraints on effective field theory parameters for the  $\Lambda N \rightarrow NN$  transition,” *Phys. Rev. C*, vol. 84, p. 024606, 2011.
- [115] M. Agnello et al., “Neutron–proton coincidences from non-mesonic weak decay of p-shell  $\Lambda$ -hypernuclei and determination of the two-nucleon induced process,” *Phys. Lett. B*, vol. 701, pp. 556–561, 2011.
- [116] G. Garbarino, A. Parreño, and A. R. (*in preparation*).
- [117] S. Scherer, “Introduction to chiral perturbation theory,” *Adv. Nucl. Phys.*, vol. 27, pp. 277–538, 2003.
- [118] J. D. Bjorken and S. D. Drell, *Relativistic Quantum Mechanics*. McGraw-Hill, 1964.
- [119] B. H. J. McKellar and B. F. Gibson, “Nonmesonic decay of heavy  $\Lambda$  hypernuclei,” *Phys. Rev. C*, vol. 30, pp. 322–330, 1984.